Title
Oh the Places You'll Go, with Graphene: A Chemists Exploration of Two Dimensions

Author
Wassei, Jonathan Khalil

Publication Date
2013

UNIVERSITY OF CALIFORNIA

Los Angeles

Oh the Places You'll Go, with Graphene: A Chemist's Exploration of Two-Dimensions

A dissertation submitted in partial satisfaction of the
Requirements for the degree of Doctor of Philosophy
in Chemistry and Biochemistry

by

Jonathan Khalil Wassei

2013

ABSTRACT OF THE DISSERTATION

Oh the Places You'll Go, with Graphene: A Chemist's Exploration of Two Dimensions

by

Jonathan Khalil Wassei

Doctor of Philosophy in Chemistry and Biochemistry

University of California, Los Angeles, 2013

Professor Richard B. Kaner, Chair

Graphene, the first two-dimensional crystal ever studied, has made such an impact in a myriad of fields ranging from physical science to engineering that its discovery earned Nobel recognition in 2010. Although it was initially lauded as the answer to the Moore's law limitation of silicon electronics, what really captivated scientists was the fact that it opened countless avenues of exploration. From a synthetic chemists perspective, it became imperative to find a more sensible way to isolate graphene if it were ever to become practical for industrial use. This thesis demonstrates several fascinating routes to synthesize graphene, such as: top down methods involving the solution processing of graphitic materials through redox chemistry and bottom-up approaches mainly using chemical vapor deposition (CVD).

Graphene oxide, a derivative of graphene, has become a promising route to graphene analogues owing to enhanced processability. A portion of this thesis is devoted to exploring solution-processing routes towards chemically converted graphene as well as functionalized nanotubes and fullerenes. Although many methods to synthesize these nanomaterials have been demonstrated, there are relatively few approaches to systematically organize these materials that meet the high throughput requirements for practical device applications. To address this concern, thin elastomeric membranes comprised of poly(dimethylsiloxane) (PDMS) can be utilized as physical stencils for patterning chemically converted graphene (CCG), carbon nanotubes (CNTs), and fullerenes, all of which can be dispersed in hydrazine. Furthermore, this method represents a simple and versatile process to selectively register these carbon nanomaterials into configurations suitable for nano electronic devices. To make films of these materials useful for transparent electrode applications, anionic dopants have been used to reduce the sheet resistance. These enhanced electronic properties are attributed to an increased number of p-type charge carriers. While there have been many reports of its use, there is little reported insight into the chemical interactions of a commonly used dopant, thionyl chloride ($SOCl_2$), with pristine graphene and its chemically converted derivatives.

The growth of graphene via CVD has predominately been accomplished with methane gas. To study the effects of other hydrocarbon precursor gases, graphene was grown by chemical vapor deposition from methane, ethane, and propane on copper foils. The larger molecules were found to more readily produce bilayer and multilayer graphene, due to a higher carbon concentration and different decomposition processes. Single- and bilayer graphene was grown with good selectivity in a simple, single-precursor process by varying the pressure of ethane from 250 to 1000 mTorr. The bilayer graphene is AB-stacked as shown by selected area electron diffraction analysis. Several device architectures were developed to exploit intrinsic properties of the derived graphene. These applications include: Flash memory devices and bio-electrodes for cell stimulation.

The dissertation of Jonathan Khalil Wassei is approved.

Xiangfeng Duan

Paul Weiss

Yang Yang

Richard B. Kaner, Chair

University of California, Los Angeles

2013

This work is dedicated to my parents A. Khalil and Marie Wassei, and to my best friend and brother, Joseph Wassei.

Table of Contents

List of Figures

Acknowledgements

I would like to thank all of the inspirational people that I have met throughout the years and have helped to mold me into the person I am today. First, I would like to thank my research advisor, Professor Richard Kaner (Ric) for his unwavering support and encouragement over the past five years. You make me want to be a better scientist. I am humbled to have also been mentored by so many other great individuals: Prof. Michael Ansell, Dr. Satinderpal Pannu, Prof. Frank Osterloh, Prof. Susan Kauzlarich and Dr. Scott Gilje.

I am thankful for the past and present members of the Kaner group, who have been my substitute family and made graduate life entertaining. You guys really put the “fun” in dysfunctional. I appreciate the help of all my colleagues at UCLA in the Kaner, Yang, Dunn and Regan labs. My CNSI officemates: Dr. Vincent Tung, Dr. William Hou, Dr. Matthew Allen and Dr. Kitty Cha who proved to be excellent peer-mentors and provided useful insight when experimenting with rocket fuel… Dr. Steven Jonas, for our efficacious discussions regarding cleanroom life, lithography and the liberty of stem cells. Dr. Matthew Mecklanberg, thank you for the countless hours you spent obtaining TEM images. My other collaborators, Emil Song and Haider Rasool, thank you for life lesson. Mr. Jaime Torres, it was a pleasure researching along side you for the final years of graduate study. To all my other colleagues at UCLA, your struggles make me feel better about myself.

I’d like to thank Dr. Bruce Weiller and Mr. Jesse Fowler, from the Aerospace Corporation, for educating me about the inner workings high vacuum systems, which has been extremely beneficial for my research.

I would like to give a special thanks to the cast and crew at the Intelligent Polymer Research Institute in the University of Wollongong, NSW, Australia. I am grateful for the hospitality and assistance of Dr. Michael Higgins, Dr. Paul Molino, Dr. Peter Sherrell and Prof. Gordon Wallace who embraced my ideas and helped me to run with them.

Finally, I’d like to thank my family for their invigorating love and continuously supporting of my foolish endeavors throughout the years.

To my high school chemistry teacher, who told me that this field wasn’t for me, I want you to know that I am still looking for your address, so I can give you a copy of my thesis.

VITA

2006	B.S., Chemistry, UC Davis, Davis, California
2005-2006	Research Associate, Department of Chemistry, UC Davis, Davis California
Summer 2005	NSF Fellow, Department of Chemistry, University of Oregon, Eugene, Oregon
2006-2007	Chemist, Department for Meso/Micro/Nano Technology, Lawrence Livermore National Laboratory, Livermore, California
2010-2011	Intern, Micro/Nano Technology Department, Micro/Nano Technology Department, El Segundo, California
Fall 2010	Visiting Scholar, Intelligent Polymer Research Institute, University of Wollongong, Wollongong, NSW, Australia
Summer 2011	Intern, Aerospace Research Labs, Northrop Grumman, Redondo Beach, California
2008- Present	Senior Research Associate, Department of Chemistry and Biochemistry, UCLA, California

PUBLICATIONS

1. Jonathan K. Wassei and Richard B. Kaner. “Oh the places you’ll go, with graphene” *Acc. of Chem. Res.*, **2012** (In Press)

2. Jonathan K. Wassei, Matthew Mecklenburg, Jaime Torres, Jesse D. Fowler, B.C. Regan, Richard B. Kaner and Bruce H. Weiller. “Chemical vapor deposition of graphene on copper from methane, ethane and propane: evidence for bilayer selectivity” *Small,* **2012**, 8, 1415-1422

3. Augustin J. Hong, Emil B. Song, Matthew J. Allen, Jonathan K. Wassei, Jiyoung Kim, Jesse Fowler, Yong Wang, Youngju Park, Faxian Xiu, Jin Zou, Richard B. Kaner, Bruce H. Weiller and Kang L. Wang. “Graphene flash memory.” *ACS Nano,* **2011**, 5, 7812-7817

4. Haider Rasool, Emil B. Song, Matthew Allen, Jonathan K. Wassei, Richard B. Kaner, Kang L. Wang, Bruce H. Weiller, James K. Gimzewski, “Continuity of graphene on polycrystalline copper” *Nano Lett.* **2011**, 11, 251-256

5. Jonathan K. Wassei, Kitty C. Cha, Vincent C. Tung, Yang Yang and Richard B. Kaner. “The effects of thionyl chloride on graphene and graphene-carbon nanotube composites.” *J. Mater. Chem.*, **2011**, 21, 3391-3396

6. Jonathan K. Wassei and Richard B. Kaner. “Graphene, a promising transparent conductor” *Materials Today* **2010**, 13, 52-59

7. Jonathan K. Wassei, Vincent Tung, Steven Jonas, Kitty Cha, Bruce Dunn, Yang Yang, Richard B. Kaner, et al “Stenciling graphene, carbon nanotubes and fullerenes with elastomeric membranes” *Adv. Mater.* **2010**, 22, 897–901

8. Vincent C. Tung, Matthew J. Allen, Jonathan K. Wassei, Richard B. Kaner, Yang Yang et al. **“**Low-temperature solution processing of graphene-carbon nanotube hybrid materials for high-performance transparent conductors.” *Nano Lett.* **2009**, 9, 1949-55.

9. Susan M. Kauzlarich, Cathie Condron, Jonathan K. Wassei, Teruyuki Ikeda, Jeffry Snyder. **“**Structure and high-temperature thermoelectric properties of SrAl2Si2.” *J. Solid State Chem*., **2009**, 182(2), 240-245.

PUBLICATIONS IN PREPARATION

1. Peter Sherrel, Brianna Thompson, Jonathan K. Wassei, Amy Geimy, Michael Higgins, Richard B. Kaner and Gordon Wallace, “Graphene enabled stimulated growth of nerve cells on biopolymers” (2013)

Chapter 1: Graphene and Applications from a Chemist's Point-of-View

1.1 An Introduction to Graphene and Chemically Converted Derivatives

Since the 2004 Nobel Prize winning report that demonstrated the existence of graphene, the first isolated two-dimensional crystal; there has been a paradigm shift in a myriad of science and engineering disciplines.[1] In just nine years, graphene has had a major impact on fields ranging from physics and chemistry to materials science and engineering, leading to a host of interdisciplinary advances in micro- and nanotechnology. Graphene is attractive because it possesses many extraordinary characteristics that are a direct consequence of its unique atomic structure.

Unlike synthetic graphene, pristine graphene is a zero-band gap semiconductor with an extraordinary room temperature carrier mobility of >20,000 cm^2/V sec.[2] Covalent, delocalized π-bonds account for its high electronic and thermal conductivity along with its ability to absorb photons uniformly across the spectrum from infrared to ultraviolet light.[3] At just a single atomic layer in thickness, it has an exceptionally high surface to volume ratio. All of the carbon atoms in graphene are essentially identical so there is no net dipole, making it nonpolar and hydrophobic.[4] The structural robustness stemming from its network of strong covalent bonds provides graphene with the ability to withstand stretching, making it "pound for pound" one of the strongest materials known.[5] Graphene is even biocompatible since it is made entirely of carbon, the most important element of life.

An important distinction should be made between graphene and chemically converted graphene. High crystalline graphene can be obtained through micromechanical cleavage of highly ordered graphite, e.g. Kish single crystals or highly oriented pyrolytic graphite (HOPG).

Other methods to synthesize graphene include Chemical Vapor Deposition using metal catalysts such as copper or reduction of silicon carbide at high temperatures.[6,7] Chemically converted graphene (CCG), on the other hand, is synthesized by a chemical, thermal and/or photolytic reduction of graphene oxide.[8,9] CCG typically has defects along the edges and basal planes, which result in a lower carrier mobility, but enhanced processability, a critical attribute if graphene is to become a useful bulk material. This chapter describes the intrinsic properties of graphene that stem from its chemical structure and essentially free electrons.

1.2 Conductivity and Mobility

As mentioned earlier, pristine graphene is a zero-band gap semiconductor with extraordinary room temperature carrier mobility, but to understand this from a chemist's point-of-view, it is helpful to start with a structural perspective. Each carbon atom in graphene's hexagonal lattice has four valence electrons; the first three are used to form covalent sp^2 bonds, while the fourth resides in a p_z orbital that forms π bonds distributed equally along 3 directions thus leading to a bond order of 1 and 1/3. Hence, a continuous layer of delocalized electrons forms across each plane that enables the rapid movement of injected electrons (Figure 1.1a). Physicists generally explain this remarkable conductivity as a consequence of a zero band gap, which can be mathematically derived by first assuming that graphene has two identical carbon atoms per unit cell (Figures 1.1b-d).[10]

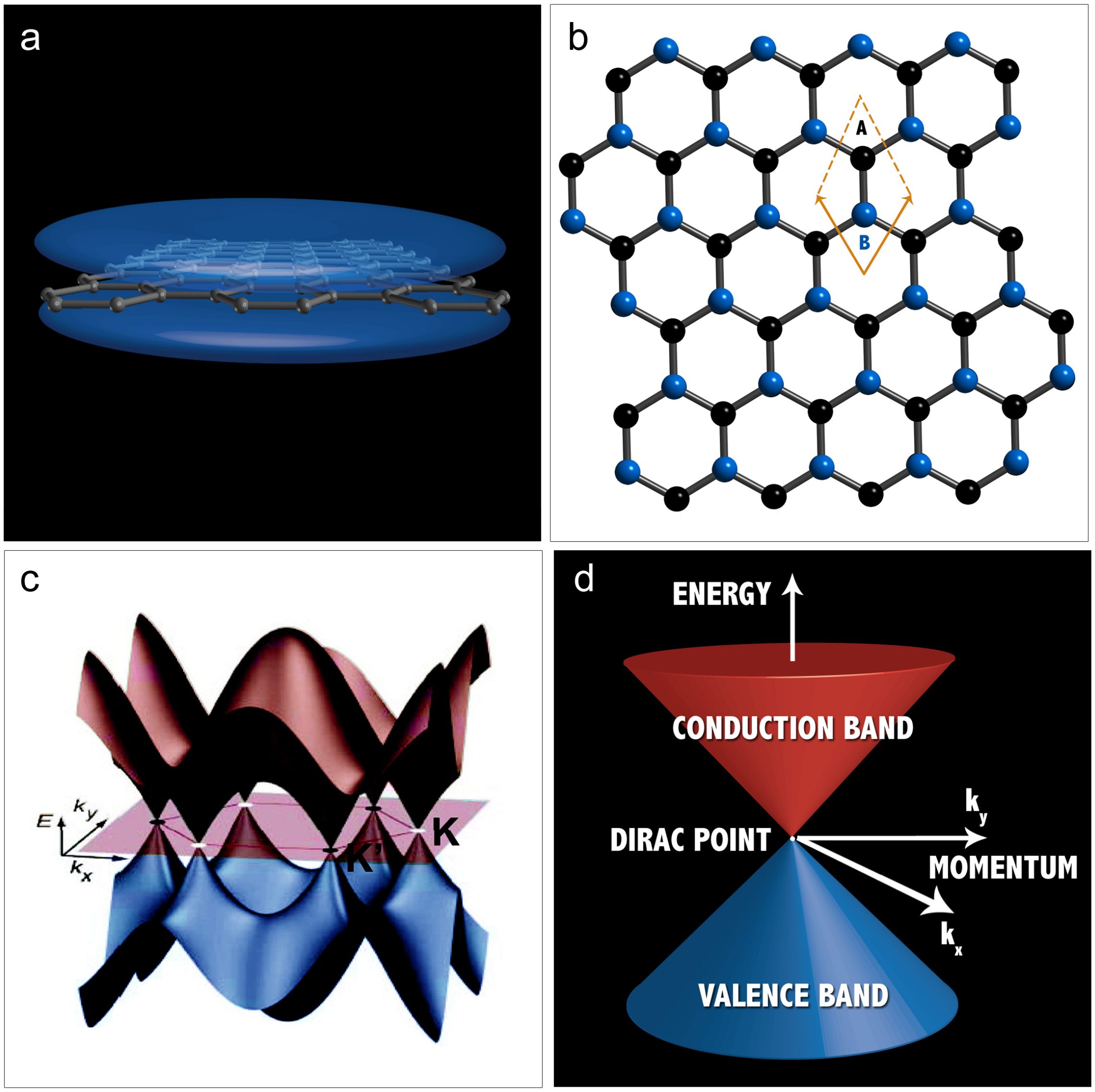

Figure 1.1 Graphene's band structure arises from delocalized pi electrons across a plane of honeycomb carbon (a); a closer look at the identical carbon atoms in a unit cell (b); which gives rise to its zero-band gap at the Dirac point (c,d). 1.1c is reprinted with permission[10] © (2010) American Chemical Society.

In addition to being highly conductive, the thinness of graphene makes it an interesting alternative to other active layer semiconductors in electronic devices. The first demonstration of using graphene's conductivity in a device was of a field-effect transistor.[11] Graphene was reported to exhibit ambipolarity, meaning it can be converted into either a p- or n-type material simply by switching the gate bias. Despite this, graphene lacks one key property, a room temperature band gap, making its integration into modern semiconductor devices and the replacement of silicon for logic-based applications problematic.

If graphene is to become useful as a high-speed transistor, a band gap is needed. There have been several reports demonstrating a wider gap in bilayer and trilayer graphene and several types of graphene derivatives including nanoribbons, strained and chemically doped graphene.[12–15] When an additional layer of graphene is Bernal stacked (i.e. ABAB…), the π-electrons are disturbed and the electronic structure changes[16–18] such that a spacing of up to 250 meV can be opened between the HOMO and LUMO, see Figure 1.2a.[12] This can be pushed further by adding a third layer, stacked ABCABC… (i.e. rhombohedral) (Figure 1.2b), but this approach is hampered by the lack of synthetic methods to produce large amounts of trilayer graphene.[13]

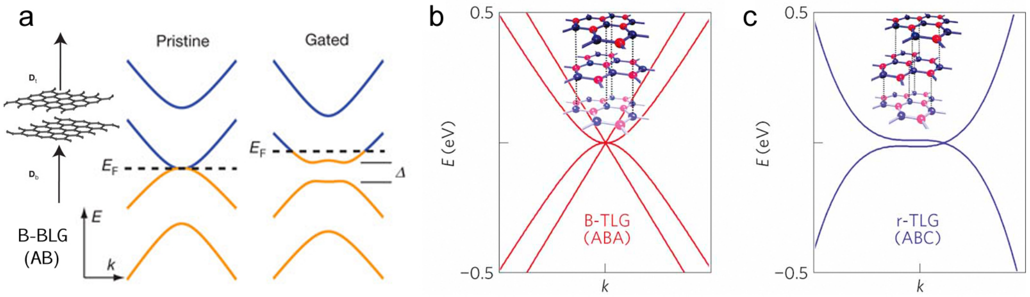

Figure 1.2 Changes in the band structure for bilayer (a) and trilayer (b, c) graphene with different stacking orders. Figures 1.2a and 1.2b,c are reprinted with permission[12,13] © (2009), (2011) Macmillan Publishers Limited.

Graphene is fundamentally a large, aromatic macromolecule that possesses an interesting chemical duality – it reacts with both electron donating and electron withdrawing groups.

Additionally, graphene can form both covalent and ionic bonds. While covalent bonds interrupt the delocalized sp^2 network, ionic bonds simply interact with it. Common organic chemical reaction pathways including hydrogenation, hydration, and electrophillic and free radical addition can take place on its surface to make derivatives such as graphene oxide.[15,19] Interactions like hydrogen plasma exposure or laser irradiation can be used to produce sp^3 graphane or fluorographene.[20,21] A variation in the degree of changes made through covalent bonding yields either a semiconducting or an insulating two-dimensional material. Ionic bonds with graphene are less invasive and usually occur along the basal plane.[14,22–24] Graphene will intermingle with other conjugated systems, via π-π stacking or weak van der Waals interactions, as is also the case for graphite.

Instead of trying to alter its structure for electronic applications, it may be more effective simply to utilize its already interesting intrinsic properties. For example, graphene's high mobility enables it to potentially play a significant role in high-frequency analog electronics, such as radio frequency (r.f.) devices, which are critical for communications equipment (Figure 1.3a).[25,26] The main attraction is that r.f. devices operate over a range of voltages rather than in terms of on/off ratios.

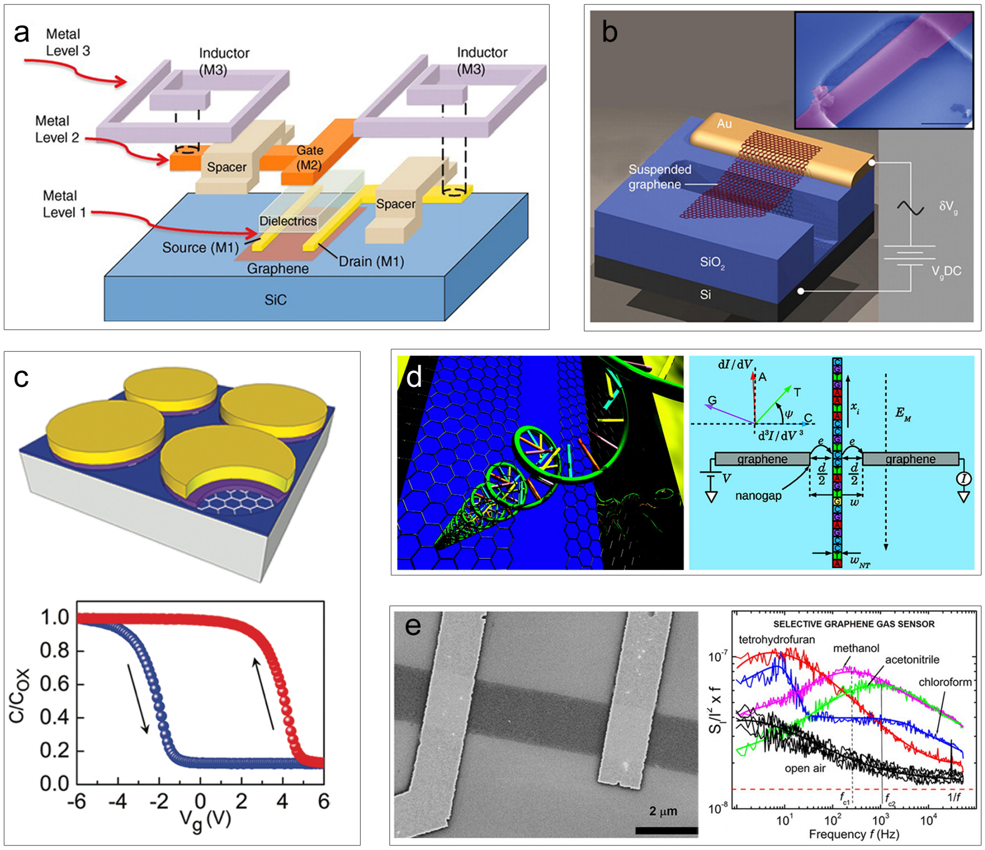

Figure 1.3 Applications utilizing graphene's intrinsic properties demonstrating utility as an integrated circuit for rf devices (a); an electromechanical resonator (b); flash memory (c); DNA translocation (d); and a chemical sensor (e). 1.3a,b reprinted with permission[26,34] © (2011, 2007) Science. 1.3b-d reprinted with permission[33,36,32,] © (2011), (2010) and (2012) American Chemical Society.

Graphene can also play a role in other frequency-related applications. For example, graphene can be used as a frequency multiplier in the THz regime, which can be used to image packages much like X-ray scanners do now in airports or to image cancer tumors for early disease diagnosis.[3,10,26–30] It is this same forward thinking that has resulted in demonstrations of electromechanical resonators (Figure 1.3b), graphene-based flash memory (Figure 1.3c), water-splitting catalysts, rapid sequencing of DNA (Figure 1.3d) and chemical sensors (Figure 1.3e).[14,31–36]

1.3 Thermal Properties

In addition to being electronically conductive, graphene also exhibits a phenomenally high thermal conductivity and this observation is a consequence of its atomic structure. While graphene's sp^2 hybridized system allows for the ballistic transport of electrons, its rigid covalent bonds are responsible for the quick dissipation of lattice vibrations known as phonons, which leads to extremely high thermal conductivities (κ) >3,000 W mK^{-1} at room temperature.[37]

The thermal properties of materials are known to change when the dimensions are reduced to the nanometer scale.[38] Heat conduction in lower dimensions is predicted to have an infinitely large intrinsic κ, because transport is confined to just one lateral dimension. Thermal transport can be limited by anharmonic phonon-phonon or phonon-electron scattering processes known as Umklapp scattering and also by defects. For all intents and purposes, κ in graphene can be readily explained in two ways - it is either ballistic or diffusive. When the mean free path (Λ) of the phonons is larger than the channel length (L), it is ballistic. Conversely, when Λ is diminished by grain boundaries or other scattering centers, $\Lambda < L$, and the thermal transport is diffusive.[39] Isotopically labeled ^{13}C was used to demonstrate that heavier carbon creates scattering centers and alters the thermal transport (Figure 1.4a). Applications in the areas of optoelectronics, thermal management, thermoelectrics and solar energy harvesting are likely to be impacted by graphene's thermal properties (Figures 1.4b,c).[40,41]

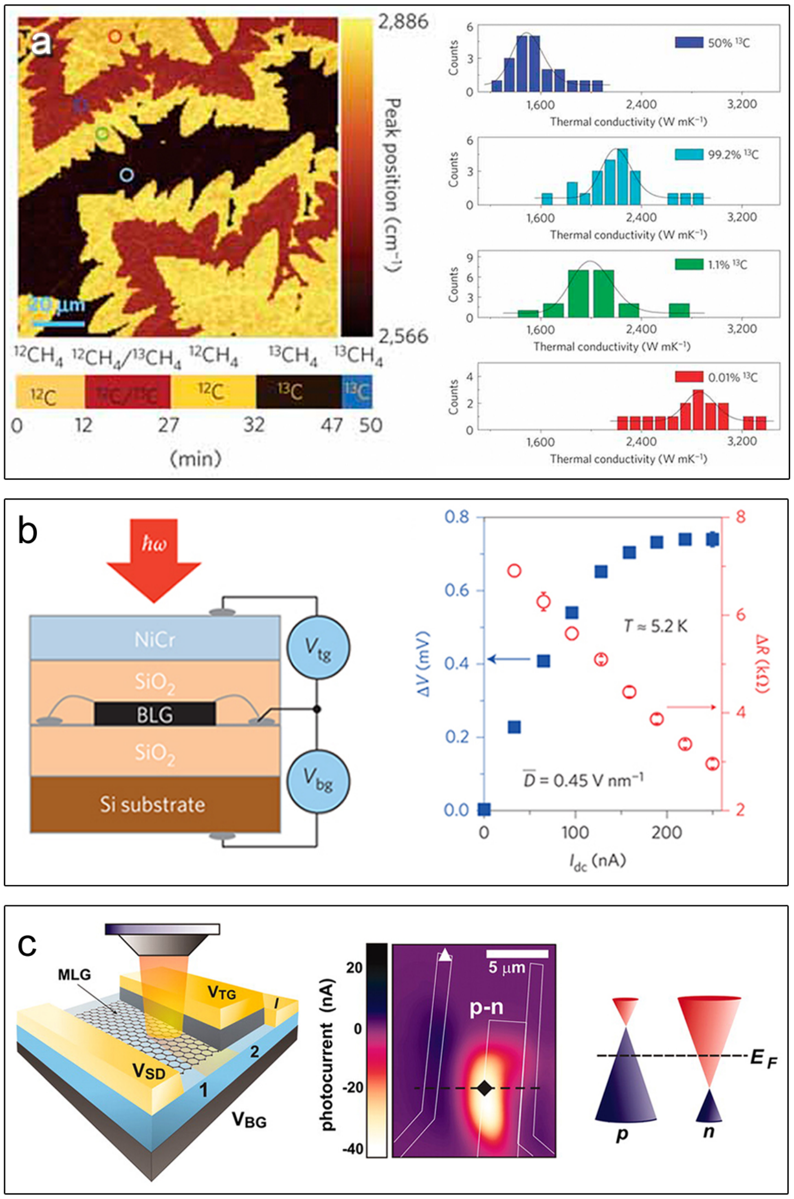

Figure 1.4 Thermal properties and applications of graphene. Raman mapping and thermal conductivity values for combinations of isotopically labeled graphene (a); graphene bolometers detect temperature-induced changes in electrical conductivity caused by the absorption of light (b). An illustration and spatially resolved photocurrent map demonstrates that gating a portion of the graphene creates an artificial p-n junction (c). Figures 1.4a,b reproduced with permission[40,41] © (2012) Macmillan Publishers Limited. American Chemical Society and 1.4c reproduced with permission[42] © (2011) Science.

1.4 Optical Properties

Graphene shows remarkable optical properties. An example is that it can be visualized on silicon dioxide as it forms an interference pattern, even though it is only one atomic layer thick.[42] Figure 1.5a shows CVD grown graphene transferred onto a silicon/silicon dioxide substrate. Graphene's transmittance can be expressed in terms of a fine-structure constant and can be derived using principles for thin-films with a fixed universal optical conductance.[43] The transparency of a single layer of graphene in the visible region has been both calculated and measured to be ~97.7% (Figure 1.5b).

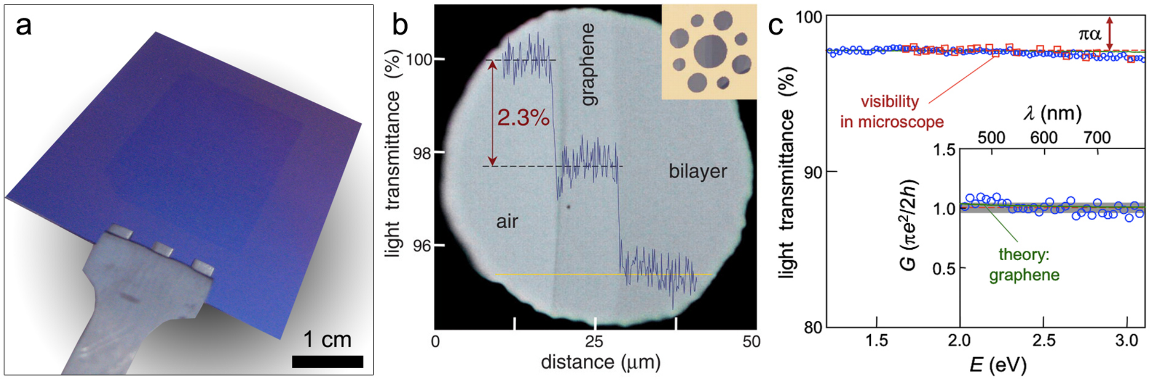

Figure 1.5 At just one atomic layer thick, graphene can be seen on silicon with a 300 nm oxide (a). Optical measurements are used to calculate that graphene absorbs 2.3% of visible light (b) and maintains a relatively uniform absorbance across the visible spectrum (c). Figure 1.5b,c reproduced with permission[44] © (2008) Science.

An alternative approach for describing graphene's optical properties is to consider it as a large macromolecule with highly delocalized electrons. Conjugated systems are used extensively for dyes and pigments because their delocalized electrons absorb photons of specific wavelengths and our eyes interpret the reflected residual wavelengths of light as color. As the degree of conjugation increases, longer wavelengths (i.e. lower energies) of the electromagnetic spectrum are more readily absorbed.

Emitted photons can be reflected from, absorbed by or transmitted within a material. In some cases, photons do not possess an appropriate energy to be absorbed and will scatter. According to Kirchhoff's law, any material that is a strong absorber of a given wavelength is also a strong emitter at that wavelength and vice versa. A strong photon absorbing material generally has a small band gap, thus making it easier for electrons to be promoted to a higher energy level. Graphene is a zero band gap crystal with delocalized electrons that behaves as if they were massless. It is for this reason why graphene not only absorbs visible wavelengths of light, but also electromagnetic energy uniformly across the spectrum, from infrared to ultraviolet.[3,10,43,44] The 97.7% transmittance is a direct consequence of the carbon atoms strongly absorbing visible light, with the remaining photons transmitting through the honeycomb structure.

The high in-plane conductivity, flatness and relative transparency of graphene makes it an obvious choice for use in optoelectronics. The absorption spectrum of single layer graphene is quite flat from 300 – 2500 nm.[28] This property makes it potentially attractive for IR shielding for next generation stealth technology. Photodetection, a measure of absorbed light and conversion into electrical current, is another possible venue.[45] Since graphene can absorb and reemit energy so rapidly, from the ultraviolet to the terahertz range, and has a large mobility, it can be used to make fast and highly sensitive photodetectors (Figure 1.6a), transparent conducting windows (Figure 1.6b), alternating current electroluminescence devices (Figure 1.6c), and light polarizers (Figure 6d).[10,27–29,45–50]

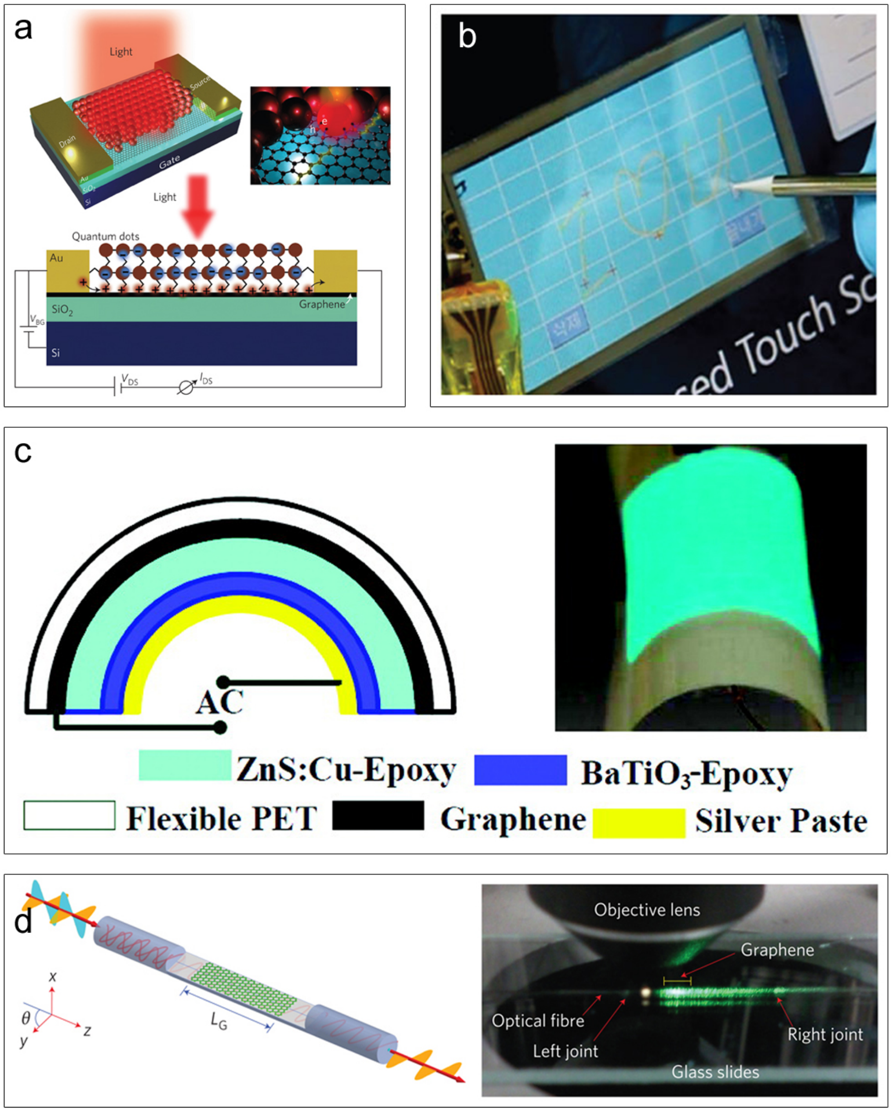

Figure 1.6 Optoelectronic graphene-based devices. A schematic of a graphene-quantum dot hybrid phototransistor (a) shows enhanced photon absorption for sensitive photodetector applications. Graphene can be used as a transparent electrode to make touch screens (b) and alternating current electroluminescence devices (c). A fiber-to-graphene coupler polarizes light (d); Optical image shows polarized green light. Figure 1.6a,b and d reproduced with permission[46,50,48] © (2010) (2012) and (2011) Macmillan Publishers Limited. Figure 1.6c reproduced with permission[51] © (2011) American Chemical Society.

1.5 High Surface Area

The surface area of nanomaterials is generally very high and graphene, with a calculated value of 2630 m^2 g^{-1}, is no exception.[51] In general, high surface area translates into increased reactivity. Since graphene comes in several varieties, these should be considered separately. CCG has the benefit of being solution processed leaving both sides available for reactions. The largest concern for pristine graphene is that up to half of the area is impeded by its interactions with a support structure. Due to a lack of high-throughput methods, there is no practical way so far to obtain large quantities of suspended graphene, so typically only one side is exposed. Stacking multilayers of graphene is problematic because the space between each layer is commonly inaccessible. Despite this, there is a plethora of space on one side of a graphene sheet that can be used as a scaffold for catalysis.

The required characteristics of a scaffold for catalytic application are: chemical and electrochemical stability, high electrical conductivity and a high surface area to uniformly disperse catalyst particles. All of the above requirements are intrinsic to graphene and scaffolding of nanoparticles for purposes such as artificial photosynthesis, photodetection and fuel cells demonstrates this utility.[22,46] For high energy density applications, a suspended or multi-dimensional architecture is required.[52–55]

With conventional energy sources peaking, the demand for renewable energy and energy efficient technology is on the rise. Many researchers have explored the potential of graphene and CCG as materials of choice for high energy density applications (Figures 1.7a-c).[51,54–58] Alternatively, multi-dimensional graphene can be grown onto porous nickel foams using CVD (Figure 1.7d).[52] These new derivatives of graphene have shown remarkably large charge capacitance values while maintaining high conductivity. The exceptional electrochemical performance of graphene-based supercapacitors is due to reversible charge storage within the available surface and crevice spaces, inherent to a 3D structure.[59] Another potentially scalable method to synthesize high surface area graphene for supercapacitors is using a laser scribe.[55,58] Graphene's high surface area may also find use in improving battery electrodes,[59] especially since carbon is an earth abundant material.

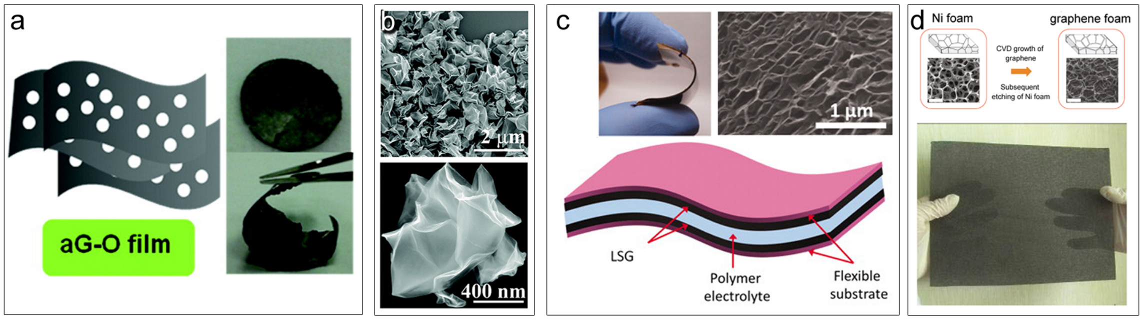

Figure 1.7 Graphene's surface area can be enhanced with 3D architectures, which extends its utility into areas such as energy storage. Examples include: porous, activated graphene oxide films (a), crumpled reduced-GO (b), laser-scribed graphene films (c), and a porous network of graphene grown via CVD onto a Ni foam (d). Figure 1.7a,b reproduced with permission[58,55] © (2012), (2011) American Chemical Society. Figure 1.7c reproduced with permission[56] © (2012) Science. Figure 1.7d reproduced with permission[53] © (2011) Macmillan Publishers Limited.

1.6 Hydrophobicity

The surface forces on materials vary from hydrophobic to hydrophilic. In the case of pristine graphene, it is hydrophobic with a relatively large contact angle near 90º.[4,60] Figure 1.8a shows an optical image of graphene on a glass cover slip. Water beads onto the glass areas that do not contain graphene because graphene has a lower surface energy than hydrophobic glass. Contact angle values for single and multilayered graphene are plotted in Figure 1.8b. In terms of polarity, the carbons along the basal plane have the same electronic configuration and are essentially identical. The net result is a lack of polarity across the crystal surface.[61] This can be utilized to make hydrophobic coatings, useful for a water barrier when graphene's conductivity is not an issue.[62–64] Chemically converted graphene contains additional functional groups such as polar oxygen or hydroxyl species, thereby making it amphiphilic. Graphene oxide sheets, which are by nature hydrophilic, can be electrophoretically deposited into hydrophobic microstructures.[65] This highly hydrophobic, low-density material can be used to produce water resistant coatings for windshields that shed water so effectively that they don't need wipers and ship hulls so slippery that they glide through the water more efficiently.[65]

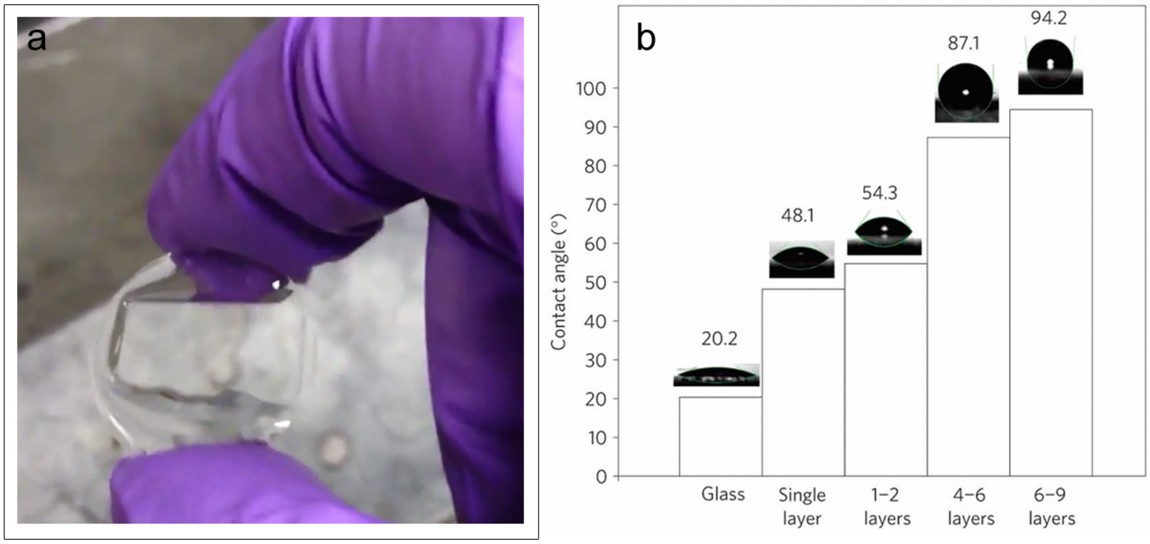

Figure 1.8 A hydrophobic coating made from graphene. Optical image of water isolated along the edges of a glass cover slip where graphene is absent (a). Contact angle measurements of water on a glass slide with increasing numbers of graphene (b). Figure 1.8b reproduced with permission[3] © (2011) Macmillan Publishers Limited.

1.7 Impermeability

Membranes are used to isolate one species from another. We see evidence of this in common food packaging. Graphene can conceivably play an important role in this area because of its ability to not only repel water, but even small atoms such as helium.[62,66] In the honeycomb structure of graphene, the hexagons possess a diameter of 0.28 nm. A simple size exclusion principle dictates that atoms with larger diameters cannot pass through it. Helium, however, has a Van der Waals radius of 0.14 nm, but still cannot pass through. While little explanation has been provided, it has been pointed out that if helium were a point particle, classical effusion principles would dictate that each atom would pass through at a rate of ~1 atom per second (STP).[67] The researchers, however, measured a much slower rate, comparable to the diffusion rate of helium through a glass substrate and claim that graphene is impermeable to even helium atoms. (see Figures 1.9a,b).

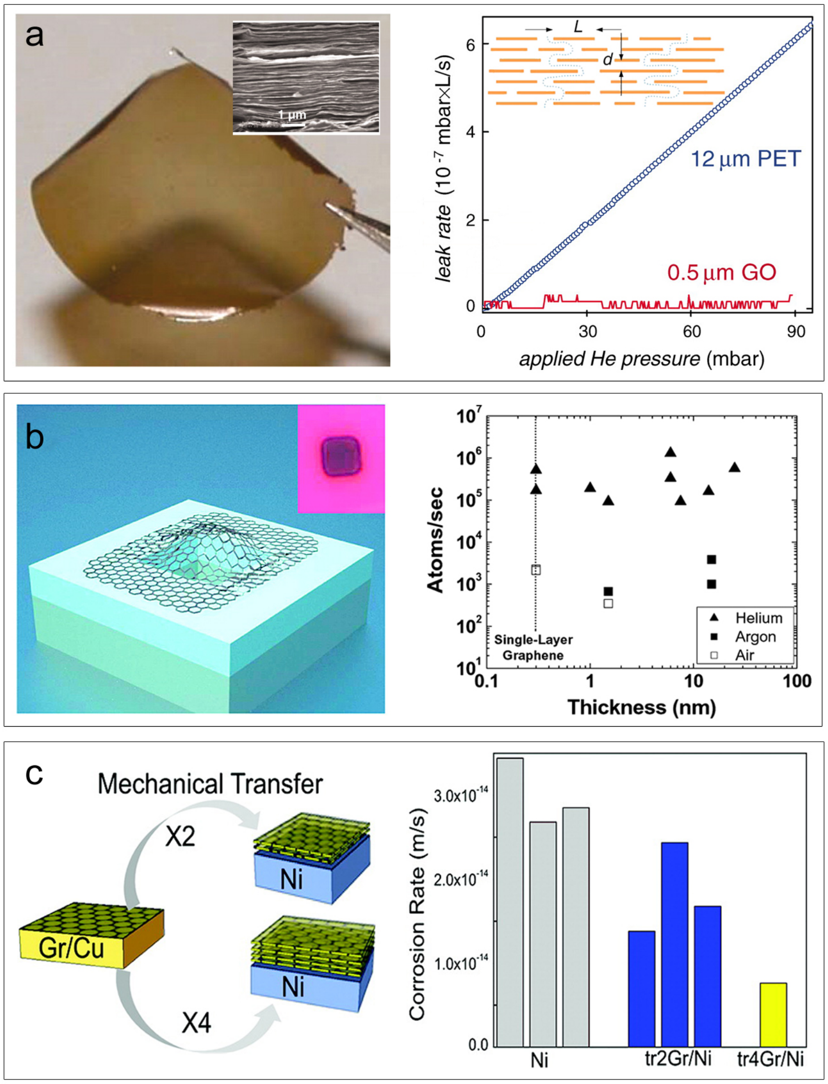

Figure 1.9 Graphene membranes made from reduced graphene oxide (a) and pristine graphene (b) can be used for blocking permeation of gases such as helium and for anti-corrosion coatings (c). Figure 1.9a reproduced with permission[63] © (2012) Science. Figure 1.9b,c reproduced with permission[65,64] © (2008), (2012) American Chemical Society.

The resistance to gas permeation has the potential to improve other areas of technology. For instance, inorganic and organic solar cells commonly use metal oxides such as indium tin oxide (ITO) as a transparent conductor because of its high transparency and low resistivity.

Besides being mechanically brittle, ITO lacks the ability to protect free ions from diffusing between stacked layers. Graphene could be an ideal candidate for protecting against such leakage.

Metal corrosion is another problem that costs US industries more that $200 billion annually.[63] A pristine and uniform graphene layer possesses the capability to act as an anticorrosion or antifouling coating. Figure 1.9c shows that graphene coatings reduce the rate of corrosion on nickel. As graphene has been shown to be biocompatible,[60] this may even prove to be useful for implantable devices.

1.8 Structural Robustness

The strength of a material is determined by how much stress can be applied without fracture and is quantified as a measure of force acting on a specific area. Stress terms can be defined as compression, tensile, shear and torsion. To measure the tensile strength (elasticity) of graphene, a force must be applied perpendicular to the basal plane of carbon. Figure 1.10a shows that graphene has an exceptionally high Young's modulus of 1,000 GPa, a shear modulus of 280 GPa, and an ultimate strength of up to 130 GPa – which is several orders of magnitude higher than that of either steel or diamond.[5,68,69] In addition to strength, graphene is quite flexible. These remarkable properties are a testament to the strength of carbon's short covalent bonds in a hexagonal layered structure.

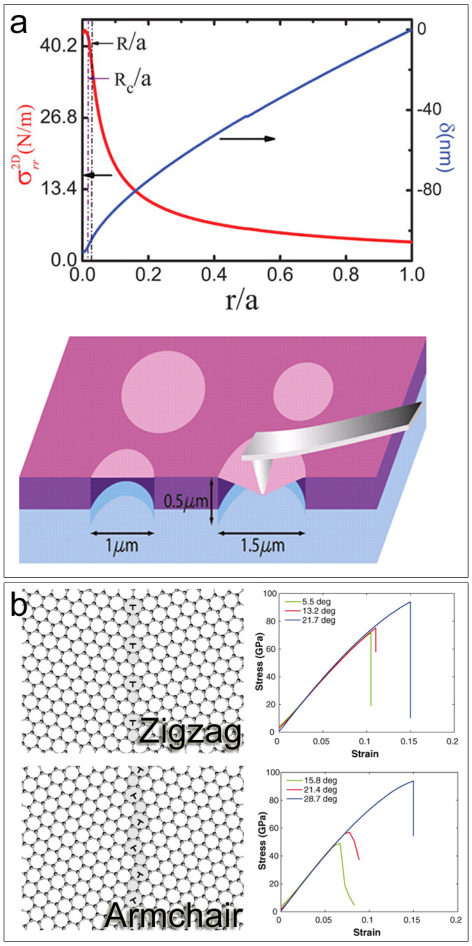

Figure 1.10 The strength of graphene is dependant on the atomic structure. A schematic representation of nano-indentation on a suspended graphene membrane is shown below the resulting stress and deflection curves versus normalized radial distance at maximum loading (a). The structures of grain boundaries in zigzag and armchair-oriented graphene sheets with varying mismatch angles and the calculated stress-strain curves for graphene pulled perpendicular to the grain boundaries (b). Figure 1.10a,b reproduced with permission[4,71] © (2008), (2012) Science.

There is a correlation between tensile strength and grain size showing that graphene sheets with highly misaligned grain boundaries are even stronger than slightly misaligned ones. In this regard, graphene can be strengthened by an increase in structural defects. A computational study suggests that 5- and 7-membered ring (Stone-Wells) grain boundary defects could account for the intrinsic strength of CVD graphene (Figure 1.10b).[70] Graphene has been assembled into fibers, papers, composites, transparent and conductive films and 3-D networks.[71–74] Composite materials could benefit from the integration of a robust, lightweight reinforcement mesh such as graphene.

1.9 Biocompatibility

Graphene is of interest to biology, medicine and bioengineering because it can be considered to be a biologically compatible material. A biocompatible material consists of two elements, biosafety (absence of negative responses) and biofunctionality (ability to perform a designed task).[60,75,76] Since graphene meets these two requirements, it has been studied as a scaffold for drug delivery and as a substrate for cell growth.[77] However, careful consideration as to where graphene is placed, its concentration and how it is used are of paramount importance.

Reports discussing the effects of exposure of graphene oxide and graphene to certain cell lines and bacteria have often met with mixed results because of differences in lateral dimensions and chemical composition.[77] The lateral dimensions of graphene affect how successful cellular interactions, such as endocytosis, will be and if small enough graphene platelets can be phagocytosed (engulfed) by macrophages (see Figure 1.11a).[61] Drug delivery therapeutics, specifically for treating neurological diseases, requires small enough sheets of graphene to cross the blood-brain barrier (BBB), so it is advantageous to use CCG or even GO in some instances.[78] Studies investigating the effects of GO and CCG films with *Escherichia colia* and *Staphylococcus aureus* bacteria show that chemically converted graphene is more toxic to these bacteria than graphene oxide.[79] This effect has been attributed to a more efficient charge transfer between the bacteria and the more sharpened edges of the CCG. Graphene's chemical sensing ability and conductivity allow it to interface with neurons and other cells that communicate via action potentials. Large area graphene has been shown to act as a scaffold for cell growth within the body (see Figure 1.11b).[75] Research in this area is relatively new and warrants further study.

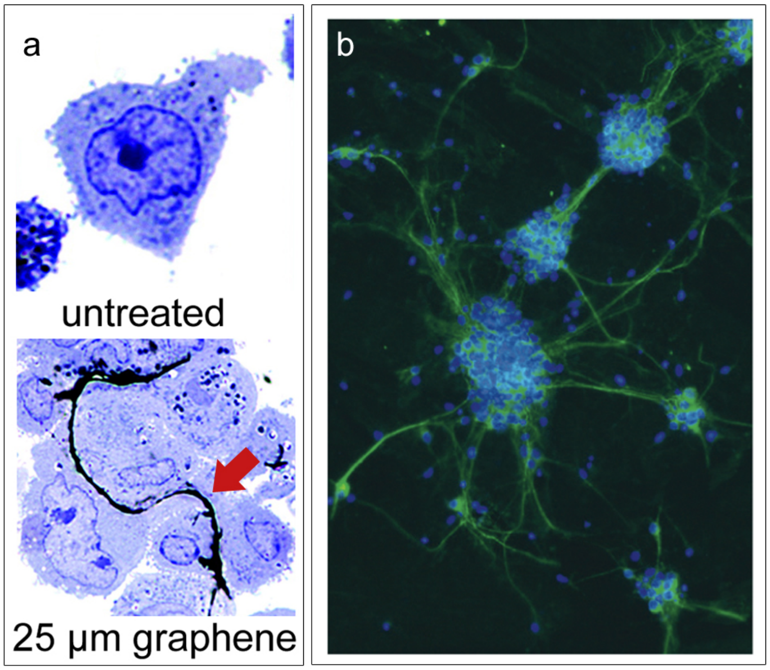

Figure 1.11 Potential biological applications for graphene include anticancer drug delivery, and as a scaffold for cell growth. Size-dependent internalizations of graphene (black) by human macrophages (blue) for clean and graphene exposed cells with lateral dimensions up to 25 µm, red arrow (a). Cortical neurons grown on graphene (nuclei are stained blue) demonstrate cell proliferation (b). Figure 1.11a reproduced with permission[61] © (2012) American Chemical Society. Figure 1.11b reproduced with permission[76] © (2012) Macmillan Publishers Limited.

1.10 Future outlook and organization of dissertation

The intrinsic properties of graphene are structurally dependent and can be explained in terms of chemical bonds and delocalized electrons. Synthetic routes to graphene and processing techniques are advancing and will continue to be an active area of research likely leading to new phenomena and uses. Many scientists have explored applications of graphene in their favorite areas of research ranging from charge storage to drug delivery, but only time will tell what ultimate applications will emerge. One thing is for certain; graphene is a truly versatile material that will continue to impact cross-disciplinary fields for many years to come.

Having said this, one of the more compelling challenges within the graphene community is to determine a practical and scalable method to synthesize it for wide spread use. This thesis accounts for several significant advances to the fields of graphene namely in synthesis/isolation, characterization and device applications. The chapters herein highlight both Top-down and Bottom-up routes to graphene, which includes intercalation/exfoliation, chemical reduction with hydrazine and other organic reagents and Chemical Vapor Deposition on copper catalyst surfaces.[16,23,73,80] While synthetic routes are of great importance, there will also be emphasis on how these different approaches have afforded unique opportunities to explore graphene's properties through novel applications such as: transparent electrodes for organic photovoltaic cells, flash memory storage structures and biocompatible electrodes for nerve cell growth.[23,32,48,73]

References

1. Novoselov, K. S., Geim. A.K., Morozov, S.V., Jiang, D. Zhang. Y., Firzov., A.A.. Electric field effect in atomically thin carbon films. *Science* **306**, 666 (2004).

2. Neto, A. H. C., Guinea, F., Peres, N. M. R., Novoselov, K. S. & Geim, A. K. The electronic properties of graphene. *Revies of Modern Physics* **81**, 109–162 (2009).

3. Palacios, T. Taking charge. *Nature* **483**, 540–5451 (2012).

4. Rafiee, J. Wetting transparency of graphene. *Nature Materials* **11**, 217–222 (2012).

5. Lee, C., Wei, X., Kysar, J. W. & Hone, J. Measurement of the Elastic Properties and Intrinsic Strength of Monolayer Graphene. *Science* **321**, 385–388 (2008).

6. Li, X. Cai, W., Kim, S., Tutuc, E., Ruoff, R.. Large-area synthesis of high-quality and uniform graphene films on copper foils. *Science* **324**, 1312–1314 (2009).

7. Hass, J., De Heer, W. A. & Conrad, E. H. The growth and morphology of epitaxial multilayer graphene. *Journal of Physics-Condensed Matter* **20**, (2008).

8. Li, D., Müller, M. B., Gilje, S., Kaner, R. B. & Wallace, G. G. Processable aqueous dispersions of graphene nanosheets. *Nature Nanotechnology* **3**, 101–105 (2008).

9. Allen, M. J., Tung, V. C. & Kaner, R. B. Honeycomb Carbon: A Review of Graphene. *Chemical Reviews* **110**, 132–145 (2010).

10. Avouris, P. Graphene: Electronic and photonic properties and devices. *Nano Letters* **10**, 4285–4294 (2010).

11. Zhang, Y., Tan, Y.-W., Stormer, H. L. & Kim, P. Experimental observation of the quantum Hall effect and Berry's phase in graphene. *Nature* **438**, 201–204 (2005).

12. Zhang, Y., Tang, T-T, Girit, C., Crommie, M.F., Wang, F.. Direct observation of a widely tunable bandgap in bilayer graphene. *Nature* **459**, 820–823 (2066).

13. Bao, W. Velasco, J., Koshino, M., Lau, C.N.. Stacking-dependent band gap and quantum transport in trilayer graphene. *Nature Physics* **7**, 948–952 (2011).

14. Wehling, T. O. Novoselov, K.S., Geim, A.K., Lichtenstein, A.. Molecular doping of graphene. *Nano Letters* **8**, 173–177 (2008).

15. Balog, R. Jorgensesn, B., Baraldi, A. Pedersesn, T.. Bandgap opening in graphene induced by patterned hydrogen adsorption. *Nature Materials* **9**, 315–319 (2010).

16. Wassei, J. K., Mecklenburg. M., Torres, J., Fowler, J., Regan, B.C., Kaner, R.B., Weiller, B.H.. Chemical Vapor Deposition of Graphene on Copper from Methane, Ethane and Propane: Evidence for Bilayer Selectivity. *Small* **8**, 1415–1422 (2012).

17. Yan, K., Peng, H., Zhou, Y., Li, H. & Liu, Z. Formation of Bilayer Bernal Graphene: Layer-by-Layer Epitaxy via Chemical Vapor Deposition. *Nano Letters* (2011).

18. Lee, S., Lee, K. & Zhong, Z. Wafer Scale Homogeneous Bilayer Graphene Films by Chemical Vapor Deposition. *Nano Letters* **10**, 4702–4707 (2010).

19. Jr, W. H. & Offeman, R. Preparation of graphitic oxide. *Journal of the American Chemical Society* **208**, 1937 (1958).

20. Sofo, J., Chaudhari, A. & Barber, G. Graphane: A two-dimensional hydrocarbon. *Physical Review B* **75**, 153401 (2007).

21. Lee, W., Suk, J., Chou, H., Lee, J. & Hao…, Y. Selective-Area Fluorination of Graphene with Fluoropolymer and Laser Irradiation. *Nano Letters* (2012).

22. Wan, X., Huang, Y. & Chen, Y. Focusing on energy and optoelectronic applications: a journey for graphene and graphene oxide at large scale. *Accounts Chemical Research* **45**, 598–607 (2012).

23. Wassei, J. K., Cha, K. C., Tung, V. C., Yang, Y. & Kaner, R. B. The effects of thionyl chloride on the properties of graphene and graphene–carbon nanotube composites. *Journal of Materials Chemistry* **21**, 3391 (2011).

24. Schedin, F. Geim, A.K., Morozov, S.V., Novoselov, K.S.. Detection of individual gas molecules adsorbed on graphene. *Nat Mater* **6**, 652–655 (2007).

25. Bourzac, K. Electronics: Back to analogue. *Nature* (2012).

26. Lin, Y.-M., Valdes-Garcia, A., Farmer, D.B., Avouris, P., Jenkins, K.A.. Wafer-Scale Graphene Integrated Circuit. *Science* **332**, 1294–1297 (2011).

27. Kim, K., Choi, J.-Y., Kim, T., Cho, S.-H. & Chung, H.-J. A role for graphene in silicon-based semiconductor devices. *Nature* **479**, 338–344 (2011).

28. Bao, Q. & Loh, K. P. Graphene photonics, plasmonics, and broadband optoelectronic devices. *ACS Nano* **6**, 3677–3694 (2012).

29. Yan, H., Li, X., Wu, Y., Avouris, P., Xia, F.. Tunable infrared plasmonic devices using graphene/insulator stacks. *Nature Nanotechnology* **7**, 330–334 (2012).

30. Savage, N. Come into the light. *Nature* (2012).

31. Rumyantsev, S., Liu, G., Shur, M. & Potyrailo…, R. Selective Gas Sensing with a Single Graphene Pristine Transistor. *Nano Letters* (2012).

32. Hong, A. J., Song, E.B., Yu, H.S., Allen, M.J., Fowler, J., Wassei, J.K., Wang, Y., Zou, J., Kaner, R.B., Weiller, B.H., Wang, K.L.. Graphene flash memory. *ACS Nano* (2011).

33. Bunch, J. S. *et al.* Electromechanical Resonators from Graphene Sheets. *Science* **315**, 490–493 (2007).

34. Fowler, J. D. *et al.* Practical Chemical Sensors from Chemically Derived Graphene. *ACS Nano* **3**, 301–306 (2009).

35. Postma, H. W. C. Rapid Sequencing of Individual DNA Molecules in Graphene Nanogaps. *Nano Letters* **10**, 420–425 (2010).

36. Lightcap, I. V, Kosel, T. H. & Kamat, P. V Anchoring Semiconductor and Metal Nanoparticles on a Two-Dimensional Catalyst Mat. Storing and Shuttling Electrons with Reduced Graphene Oxide. *Nano Letters* **10**, 577–583 (2010).

37. Balandin, A. A. Thermal properties of graphene and nanostructured carbon materials. *Nature Materials* **10**, 569–581 (2011).

38. Gilje, S. *et al.* Photothermal Deoxygenation of Graphene Oxide for Patterning and Distributed Ignition Applications. *Advanced Materials* **22**, 419–423 (2010).

39. Chen, S. *et al.* Thermal conductivity of isotopically modified graphene. *Nature Materials* **11**, 1–5 (2012).

40. Yan, J. *et al.* Dual-gated bilayer graphene hot-electron bolometer. *Nature Nanotechnology* 1–7 (2012).

41. Gabor, N. M. *et al.* Hot Carrier-Assisted Intrinsic Photoresponse in Graphene. *Science* **334**, 648–652 (2011).

42. Song, E. B. *et al.* Visibility and Raman spectroscopy of mono and bilayer graphene on crystalline silicon. *Applied Physics Letters* **96**, 81911 (2010).

43. Nair, R. R. *et al.* Fine structure constant defines visual transparency of graphene. *Science* **320**, 1308 (2008).

44. Yan, H. *et al.* Infrared spectroscopy of wafer-scale graphene. *ACS Nano* (2011).

45. Konstantatos, G. *et al.* Hybrid graphene-quantum dot phototransistors with ultrahigh gain. *Nature Nanotechnology* (2012).

46. Mueller, T., Xia, F. & Avouris, P. Graphene photodetectors for high-speed optical communications. *Nature Photon* **4**, 297–301 (2010).

47. Bao, Q. *et al.* Broadband graphene polarizer. *Nature Photonics* **5**, 411–415 (2011).

48. Wassei, J. K. & Kaner, R. B. Graphene, a promising transparent conductor. *Materials Today* **13**, 52–59 (2010).

49. Bae, S. *et al.* Roll-to-roll production of 30-inch graphene films for transparent electrodes. *Nature Nanotechnology* **5**, 574–578 (2010).

50. Wang, Z. *et al.* Flexible Graphene-Based Electroluminescent Devices. *ACS Nano* (2011).

51. Stoller, M. D., Park, S., Zhu, Y., An, J. & Ruoff, R. S. Graphene-Based Ultracapacitors. *Nano Letters* **8**, 3498–3502 (2008).

52. Chen, Z. Three-dimensional flexible and conductive interconnected graphene networks grown by chemical vapour deposition. *Nat Materials* **10**, 424–428 (2011).

53. Choi, B., Yang, M., Hong, W. & Choi…, J. 3D Macroporous Graphene Frameworks for Supercapacitors with High Energy and Power Densities. *ACS Nano* **6**, 420–428 (2012).

54. Luo, J. *et al.* Compression and Aggregation-Resistant Particles of Crumpled Soft Sheets. *ACS Nano* (2011).

55. El-Kady, M. F., Strong, V., Dubin, S. & Kaner, R. B. Laser Scribing of High-Performance and Flexible Graphene-Based Electrochemical Capacitors. *Science* **335**, 1326–1330 (2012).

56. Zhu, Y. *et al.* Carbon-Based Supercapacitors Produced by Activation of Graphene. *Science* **332**, 1537–1541 (2011).

57. Zhang, L. L. *et al.* Highly conductive and porous activated reduced graphene oxide films for high-power supercapacitors. *Nano Letters* (2012).

58. Gao, W. *et al.* Direct laser writing of micro-supercapacitors on hydrated graphite oxide films. *Nature Nanotechnology* **6**, 496–500 (2011).

59. Merlet, C., Rotenberg, B., Madden, P. & Taberna…, P. On the molecular origin of supercapacitance in nanoporous carbon electrodes. *Nat Materials* (2012).

60. Sanchez, V. C., Jachak, A., Hurt, R. H. & Kane, A. B. Biological Interactions of Graphene-Family Nanomaterials–An Interdisciplinary Review. *Chemical Research in Toxicology* (2012).

61. Leenaerts, O., Partoens, B. & Peeters, F. Water on graphene: Hydrophobicity and dipole moment using density functional theory. *Physical Review B* **79**, 235440 (2009).

62. Nair, R. R., Wu, H. A., Jayaram, P. N., Grigorieva, I. V & Geim, A. K. Unimpeded Permeation of Water Through Helium-Leak-Tight Graphene-Based Membranes. *Science* **335**, 442–444 (2012).

63. Prasai, D., Tuberquia, J. C., Harl, R. R., Jennings, G. K. & Bolotin, K. I. Graphene: Corrosion-Inhibiting Coating. *ACS Nano* (2012).

64. Bunch, J. S. *et al.* Impermeable Atomic Membranes from Graphene Sheets. *Nano Letters* **8**, 2458–2462 (2008).

65. Hasan, S. A. *et al.* Transferable graphene oxide films with tunable microstructures. *ACS Nano* **4**, 7367–7372 (2010).

66. Compton, O. C., Kim, S., Pierre, C., Torkelson, J. M. & Nguyen, S. T. Crumpled graphene nanosheets as highly effective barrier property enhancers. *Advanced Materials* **22**, 4759–63 (2010).

67. Nair, R. R. *et al.* Graphene as a transparent conductive support for studying biological molecules by transmission electron microscopy. *Applied Physics Letters* **97**, 153102 (2010).

68. Tan, P. H. The shear mode of multilayer graphene. *Nature Materials* **11**, 294–300 (2012).

69. Liu, X., Metcalf, T. H., Robinson, J. T., Houston, B. H. & Scarpa, F. Shear modulus of monolayer graphene prepared by chemical vapor deposition. *Nano Letters* **12**, (2012).

70. Grantab, R., Shenoy, V. B. & Ruoff, R. S. Anomalous Strength Characteristics of Tilt Grain Boundaries in Graphene. *Science* **330**, 946–948 (2010).

71. Shin, M. K. *et al.* Synergistic toughening of composite fibres by self-alignment of reduced graphene oxide and carbon nanotubes. *Nature Communications* **3**, 650–658 (2012).

72. Li, D. & Kaner, R. B. Materials Science: Graphene-Based Materials. *Science* **320**, 1170–1171 (2008).

73. Tung, V. C. *et al.* Low-Temperature Solution Processing of Graphene−Carbon Nanotube Hybrid Materials for High-Performance Transparent Conductors. *Nano Letters* **9**, 1949–1955 (2009).

74. Tang, H., Ehlert, G. J., Lin, Y. & Sodano, H. Highly Efficient Synthesis of Graphene Nanocomposites. *Nano Letters* **12**, 84–90 (2012).

75. Schmidt, C. Bioelectronics: The bionic material. *Nature* **483**, S37 (2012).

76. Yang, K. *et al.* Graphene in Mice: Ultrahigh In Vivo Tumor Uptake and Efficient Photothermal Therapy. *Nano Letters* **10**, 3318–3323 (2010).

77. Zhang, Y. *et al.* Cytotoxicity effects of graphene and single-wall carbon nanotubes in neural phaeochromocytoma-derived PC12 cells. *ACS Nano* **4**, 3181–3186 (2010).

78. Li, M., Yang, X., Ren, J., Qu, K. & Qu, X. Using Graphene Oxide High Near-Infrared Absorbance for Photothermal Treatment of Alzheimer’s Disease. *Advanced Materials* **24**, 1722–1728 (2012).

79. Hu, W. *et al.* Graphene-based antibacterial paper. *ACS Nano* **4**, 4317–4323 (2010).

80. Wassei, J. K. *et al.* Stenciling Graphene, Carbon Nanotubes, and Fullerenes Using Elastomeric Lift-Off Membranes. *Advanced Materials* **22**, 897–901 (2010).

Chapter 2: Top-down Synthesis of Graphene and Applications

2.1 Impetus for Solution Processing and Stenciling of Small Graphitic Structures

Generating alternative and successful approaches to isolating single layer graphene has proven to be a large undertaking. Across the globe, several interdisciplinary groups have embarked on this quest, which resulted in a plethora of results; some remarkable and some prosaic. As this field has matured over these past eight years only a few of those processes have emerged as desirable pathways. This chapter discusses one such approach; solution processing of chemically converted graphene. Many topics will be introduced and discussed throughout this chapter: *processing,* methods to enhance the material output and its overall properties; *deposition*, a myriad of ways to deposit and isolate single – few layers of graphene for electronic devices and thin film conductors; and finally, *applications*, which is simply an exploration of the intrinsic properties of the material through device architectures. Before these concepts are discussed, it should be mentioned that other low dimensional allotropes of carbon, such as fullerenes and nanotubes, could also be solution-processed alongside chemically converted graphene (CCG).

2.2 Synthesis and Processing of Graphitic Structures

CCG, a useful analog of graphene, is a practical alternative, when high electrical performance is not a critical necessity. This chapter discusses the ability to solution process chemically converted graphene in anhydrous hydrazine, due to the residual functional groups interacting with hydrazine; at least this was the hypothesis. To test this, other allotropes with and without residual functional groups were examined to re-examined and extended to include carbon nanotubes and fullerenes. It was found that un-functionalized carbon nanotubes do not interact with hydrazine and settle to the bottom of a vial of hydrazine. To form a stable dispersion of CNTs and fullerenes in hydrazine, we suggested that the formation of hydrazinium compounds comprised of negatively charged CNTs and [6,6]-phenyl-C_{61}-butyric acid methyl ester (PCBM) surrounded by $N_2H_5^+$ counterions was needed, as discussed in more detail later. Such hydrazinium compounds are known to readily disperse in hydrazine.

Similar to a previous study, graphene oxide (GO) was used as a precursor to CCG.[1] The graphite oxide materials used for these experiments were prepared via a modified Hummer's method[2] and produced copious amounts of GO, which can be and was stored as aqueous (2% w/v) dispersions and used as needed. Prior to reduction, the GO paste was dried under vacuum using 0.22 μm alumina Anodisc filter membranes, purchased from Whatman. A thick, black paper-like material is produced after 24 h of drying under ambient conditions. P3 single-walled carbon nanotubes, purchased from Carbon Solutions Inc., were purified by refluxing for 1 h in ethanol followed by a mild oxidation in a 1 molar nitric acid solution to integrate hydroxyl moieties onto the surface of the nanotubes. Similar to GO films, these water dispersible nanotubes were suspended into water, filtered and dried under vacuum for 24 h. Dry powders of PCBM were purchased from Nano-C, Inc. and used as received.

The materials were pre-weighed, transferred into a nitrogen glove box, dissolved into clear anhydrous hydrazine and left to stir for at least 24 h. Effervescence of nitrogen gas occurred upon contact with hydrazine. CCG and CNTs dispersed in hydrazine formed black colloids, while the PCBM dissolves in hydrazine to yield a dark yellow, translucent solution. Chemically converted graphene, carbon nanotubes and PCBM hydrazinium dispersions were prepared in concentrations of 1 mg/ml, 10 mg/ml and 15 mg/ml, respectively, and subsequently purified to remove larger aggregates.

Hydrazinium graphene and carbon nanotube suspensions were purified using a combination of centrifugation, dilution and ultra-sonication, while dispersions of PCBM are simply diluted to different loading conditions to vary the final thicknesses. To isolate single and few layer sheets of CCG and single from bundled carbon nanotubes, the respective dispersions were centrifuged, using a Heraeus Labofuge 400, between 1200 and 1500 rpm for 45-60 minutes. This process helped to separate the materials based on their masses. For a typical 1 mL centrifuge vial, the top 100 μL is collected in an air-free environment and dispersed into 900 μL of fresh anhydrous hydrazine. The dregs, at the bottom of the vials, were not used for any further investigation beyond the initial analysis. In some instances, sonication was then used to help disperse the materials into the hydrazine. Sonication was carried out using a VWR model 250D sonicator set at level 9 for 10 min. Interestingly, it was found that prolonged exposure to sonication assisted in further breaking up of the graphitic materials into smaller fragments.

When a 532 nm green laser is projected through purified mixtures of carbon nanotubes (0.1 mg/ml), PCBM (0.5 mg/ml) and chemically converted graphene (0.1 mg/ml), respectively, light scatters differently based on the Tyndall effect. A beam of light traveling along a straight path will be scattered if it comes into contact with discontinuities such as colloidal particles in a suspension, as seen in Figure 2.1. A higher loading concentration of PCBM was used to enhance the yellow color of the solution, which may account for a modicum of light scattering that can be seen through the solution. Additionally, the glass vial diffracts some light around the edges. The difference in light scattering intensity correlates with differences in particle size and dimensionality. Since a single-walled carbon nanotube can be thought of as a rolled-up graphene sheet, it is logical that they will absorb up to twice as much visible light. Likely for this reason, CNT dispersions appear darker and scatter light more heavily than CCG colloids.

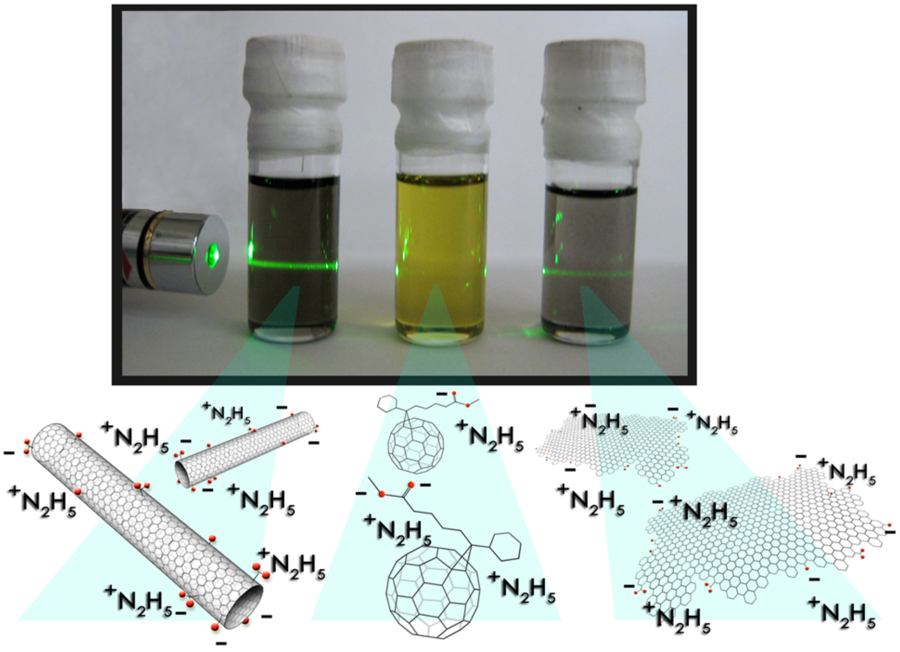

Figure 2.1 The "Tyndall effect " is observed upon shining a 532 nm green laser through a 0.1 mg/ml mixture of carbon nanotubes (left), 0.5 mg/ml phenyl-C_{60}-butyric acid methyl ester (middle) and 0.1 mg/ml chemically converted graphene (right) dispersed in hydrazine. Figure 2.1 is reprinted with permission[4] © 2010 WILEY-VCH Verlag GmbH & Co. KGaA, Weinheim

PCBM disperses in hydrazine to form a transparent yellow solution, shown in Figure 2.1, at a rather high loading (17 mg/ml). The compatibility of PCBM in hydrazine can be attributed to the functionality present on the fullerene, which also enables it to be dissolved in common organic solvents.[3] Interestingly, while PCBM forms a solution in hydrazine, CNTs and CCG tend to form colloidal dispersions in hydrazine. The reason for this is likely due to differences in size. The dimensions of a fullerene are within the nanometer regime, while the other two allotropes contain at least one dimension on the micron scale.

As described in another paper,[1] CCG can be deposited onto a variety of substrates via spin-coating. Since hydrazine is inherently hydrophilic, the SiO_2 or glass substrates are generally pretreated with a 30 W powered oxygen plasma source, for 5 minutes, to activate the surface functional groups and enhance the hydrophillicity. These substrates were brought into an air-free glove box and used as surfaces to deposit graphitic materials via drop-casting and spin-coating. After deposition, thermal annealing carried out at a relatively low temperature (150˚C), can be used to drive off residual hydrazine.[1] The shortcoming of this method is that deposition is random and at best, produces films of CCG that can be used as semi-transparent electrodes.

2.3 Selective Deposition of Graphene Using Stencil Masks

One solution to the impasse of random distribution was to prepare stencils that would be stable in the presence of hydrazine.[4] The idea stemmed from previous t-shirt designing exploits as wells as studies involving the patterning of carbon nanotubes and fullerenes into a matrix.[3,5–9] For example, carbon nanotubes have been patterned through soft transfer printing,[5] spray-coating,[6] ink-jet printing,[7] and dielectrophoresis,[8] but low resolution and length limitations of the nanotube can be problematic. Arrays of fullerenes have also been constructed, for example, via physical vapor transport (PVT) onto self-assembled monolayers of octadecyltrichlorosilane.[3,9] Fullerenes arranged by PVT have been utilized in organic field effect transistors and in the photoactive layer of bulk heterojunction solar cells. While relatively large fullerene features on the order of 8 x 8 μm can be obtained on silicon with PVT, the typical processing temperatures required for this technique (425 - 500˚C) preclude the use of flexible plastics as substrates for device fabrication.

Hydrazine is a strong base that interacts strongly with many materials. With this in mind, thin elastomeric membranes comprised of polydimethylsiloxane (PDMS), which is stable in hydrazine, can be used as a physical mask for patterning chemically converted graphene (CCG), carbon nanotubes (CNT) and fullerenes dispersed in hydrazine. Furthermore, this method represents a simple and versatile process to selectively register these carbon nanomaterials into configurations suitable for nano electronic devices.

PDMS is an elastomeric material that has become ubiquitous in applications ranging from microfluidics, biomedical packaging, and the soft lithographic patterning of a variety of materials including metals.[10] PDMS is well suited as a mask material based on the ease with which it can be fashioned into many desired structures, as well as its resistance to many chemical and physical processes. PDMS is also a flexible material that makes intimate contact by conforming to the contours of the surface. In this case, it was designed to make a leak proof mask from which the solution-processed material can be deposited into.

2.3.1 Fabrication of Elastomeric Membranes and Stenciling of Carbon Nanomaterials

Templates for preparing PDMS membranes with defined cavities were fabricated with conventional photolithography. Figure 2.2 outlines the process used to mold an elastomeric membrane from the photo-lithographically prepared master and to stencil arrays of graphene, carbon nanotubes and/or fullerenes from charge-stabilized solutions in hydrazine.

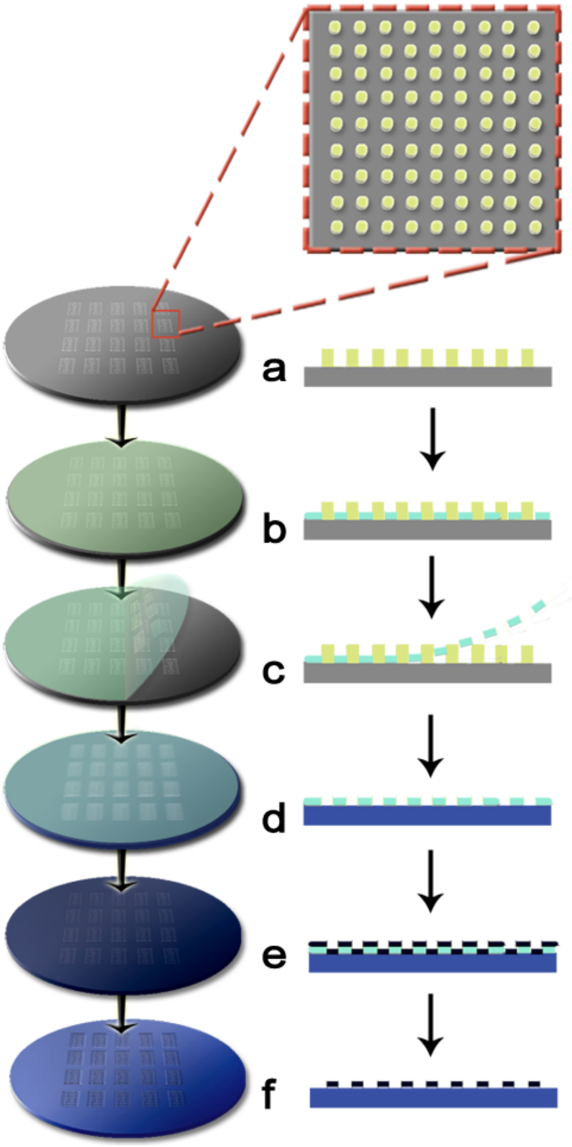

Figure 2.2 A schematic diagram illustrating how to stencil carbon-based nano-materials onto any substrate using an elastomeric lift-off membrane: Wafer view (left) and side view (right). a) A master silicon wafer with raised photoresist features is fabricated; b) a thin PDMS layer is then spin-coated onto the master wafer, which is c) subsequently removed and d) placed onto a new silicon wafer with a 300 nm thermal oxide coating. e) Carbon-based nano-materials are then spin-coated over the entire membrane. f) The coated membrane is finally lifted-off leaving behind an array of carbon-based nano-materials. Figure 2.2 is reprinted with permission[4] © 2010 WILEY-VCH Verlag GmbH & Co. KGaA, Weinheim

To inhibit SU-8 and PDMS lamination, the features are exposed to tridecafluoro-1,1,2,2-tetrahydrooctyl-1-trichlorosilane under vacuum for 1 h rendering the features hydrophobic. A Veeco Dektak profiler was used to measure the step heights of the SU-8 features to be 135-140 μm in height and the width ranges between 75 – 200 μm. The features are made by spin-coating SU-8 2100 onto a silicon wafer at 2000 rpm. Post annealing, the films are exposed to UV irradiation using a Karl Suss contact aligner and the non-exposed regions are developed away in SU-8 developer. The final designs are rinsed with isopropyl alcohol and hard baked.

Stencils were prepared by spin-coating Sylgard 184 - polydimethylsiloxane (PDMS) over the master wafer at speeds of 2500 - 3000 rpm, which yielded membranes with thicknesses of 10 – 50 μm. Low molecular weight polymers were removed from the membranes by soaking for 2 h in dichloromethane and drying in a vacuum oven at 65˚C overnight. The treated membranes were finally rinsed with IPA and dried in a desiccator overnight.

Images of a typical PDMS membrane are provided in Figure 2.3 to illustrate the uniformity of the features. Once cured, PDMS membranes are cut from the mold using a clean razor and placed onto a substrate with fine tip tweezers, Figure 2.3a. These membranes are freestanding and not limited by the shapes described here. Furthermore, the master wafer is reusable several times over and fresh PDMS membranes can be readily fabricated, sidestepping the arduous task of pre-fabricating alignment markers prior to every deposition.

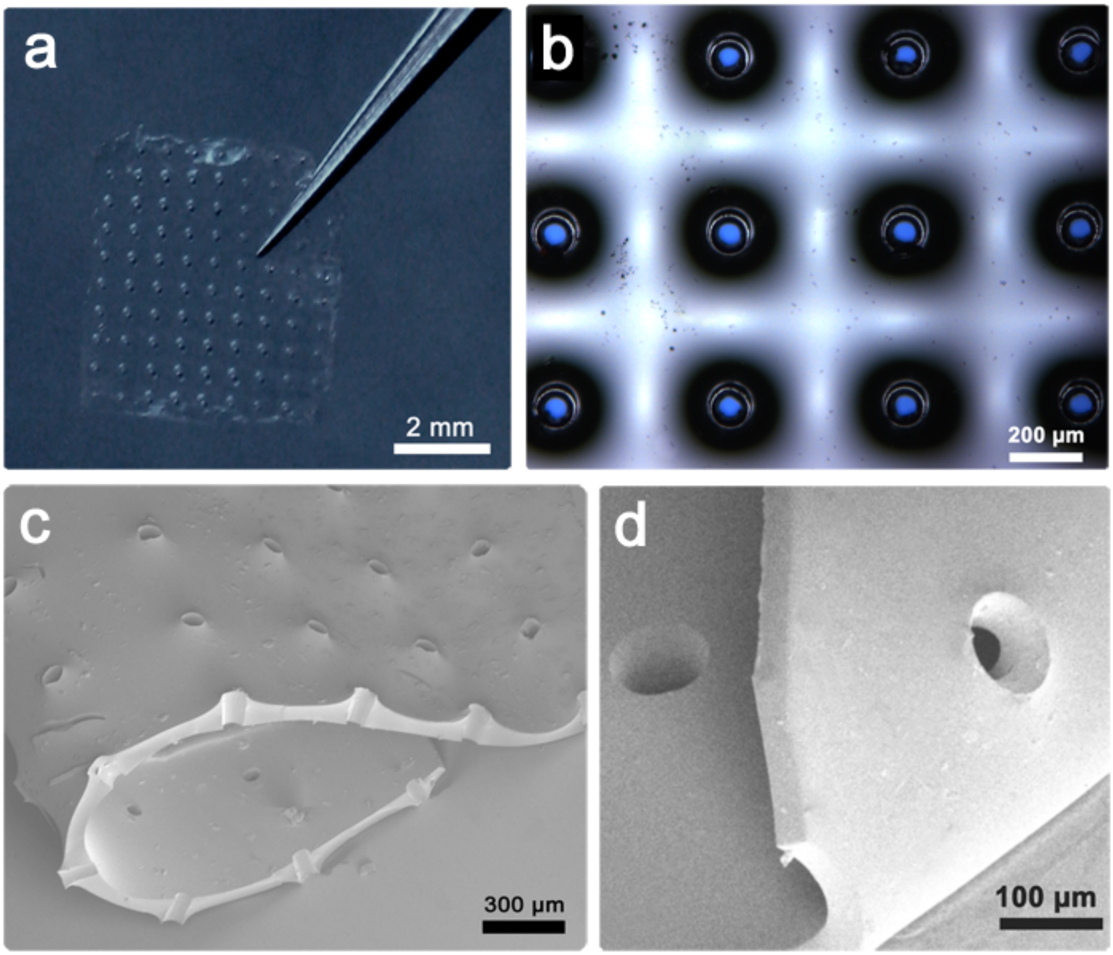

Figure 2.3 a) A freestanding elastomeric membrane held by tweezers. Pores made from a silicon mold are clearly visible. b) An optical microscope image of the membrane pores shows the blue silicon dioxide substrate beneath it. c) An SEM image shows a cross-sectional view of a folded membrane, d) and a magnified view of the membrane pores. Figure 2.3 is reprinted with permission[4] © 2010 WILEY-VCH Verlag GmbH & Co. KGaA, Weinheim

The thin PDMS sheet conforms to the substrate surface as seen in Figure 2.3b, which shows the membrane resting on top of a silicon oxide surface (blue) with no visible air pockets. In instances where the membrane is very thin, a few drops of isopropyl alcohol are used to temporarily lubricate the surface to prevent the membrane from self-adhering.

The wettability of the substrate surface plays a vital role in determining the uniformity of material coverage. For instance, a completely hydrophobic surface will limit the material to beaded regions along the corner of the substrate and virtually no deposition through the stencil. To reduce the surface tension we briefly expose our membrane-covered substrates to an oxygen plasma. After this treatment, the surface becomes temporarily hydrophilic, enabling the deposition of CNTs, CCG, or PCBM into the membrane cavities via spin-coating.

After deposition, the PDMS membrane is removed and defined arrays of chemically converted graphene, carbon nanotubes and fullerenes are revealed. The substrates are then thermally annealed to drive off any residual hydrazine. In **Figure 2.4**, arrays patterned from the hydrazinium solutions can be seen.

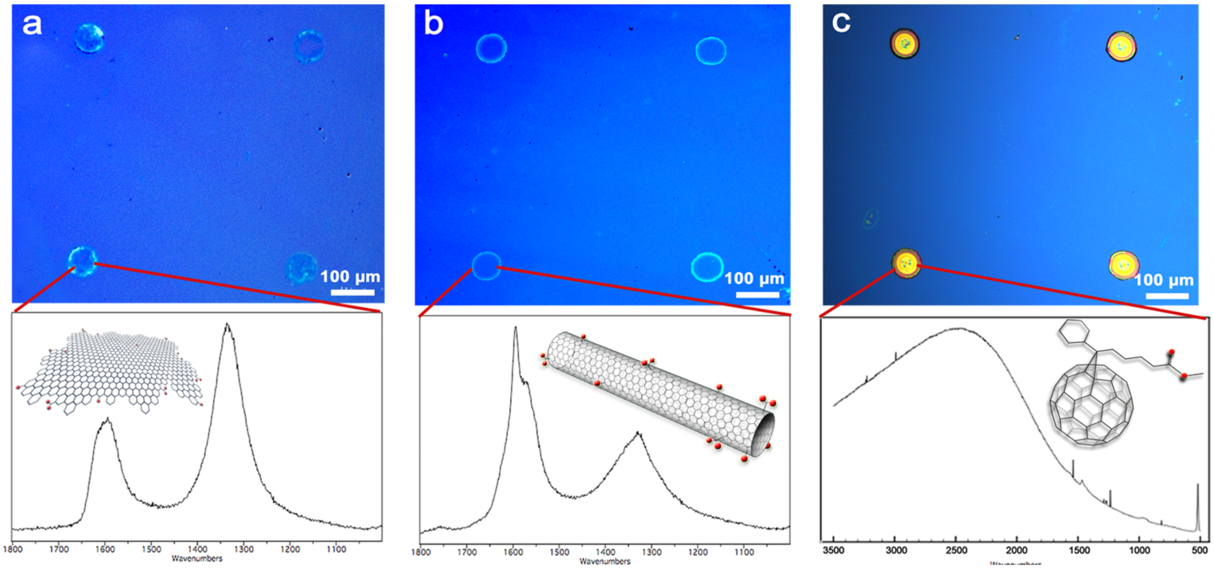

Figure 2.4 Optical microscope images of silicon oxide substrates show patterned arrays of carbon materials with representative Raman spectra: a) Chemically converted graphene, b) single-walled carbon nanotubes and c) phenyl-C_{60}-butyric acid methyl ester (PCBM). Figure 2.4 is reprinted with permission[4] © 2010 WILEY-VCH Verlag GmbH & Co. KGaA, Weinheim

2.4 Analysis of Stenciled Graphene, Carbon Nanotubes and Fullerenes

Raman spectroscopy was used to further demonstrate the presence of each graphitic material within the pre-determined locations, as seen in Figure 2.4. The Raman spectra of chemically converted graphene shows a G band around 1600 cm^{-1}, while the spectra of carbon nanotubes have two peaks at the G band resulting from the semiconducting (larger) and the metallic (smaller) conformations.[11] For PCBM, we resolved several peaks hidden beneath the strong fluorescing band as well as the characteristic 1450 cm^{-1} peak.[12]

Scanning electron microscope (SEM) and atomic force microscope (AFM) images taken within the individual arrays provide a detailed overview of the surface coverage and nano-topology of the materials. Figure 2.5a shows the AFM step height of CCG to be ~0.6 nm, indicative of a single layer as explained by Tung et al.[1] We can control the amount of material deposited by changing the concentration of the dispersions as needed. In Figure 2.5a, we used a concentration of 0.1 mg/ml to deposit a single sheet of graphene. In Figures 2.5b and 2.5c the SEM and AFM images show bundles of single-walled carbon nanotubes and large round aggregates of coalesced PCBM, respectively. Similarly, a few bundles of CNTs can be isolated through dilution of the graphitic dispersion.

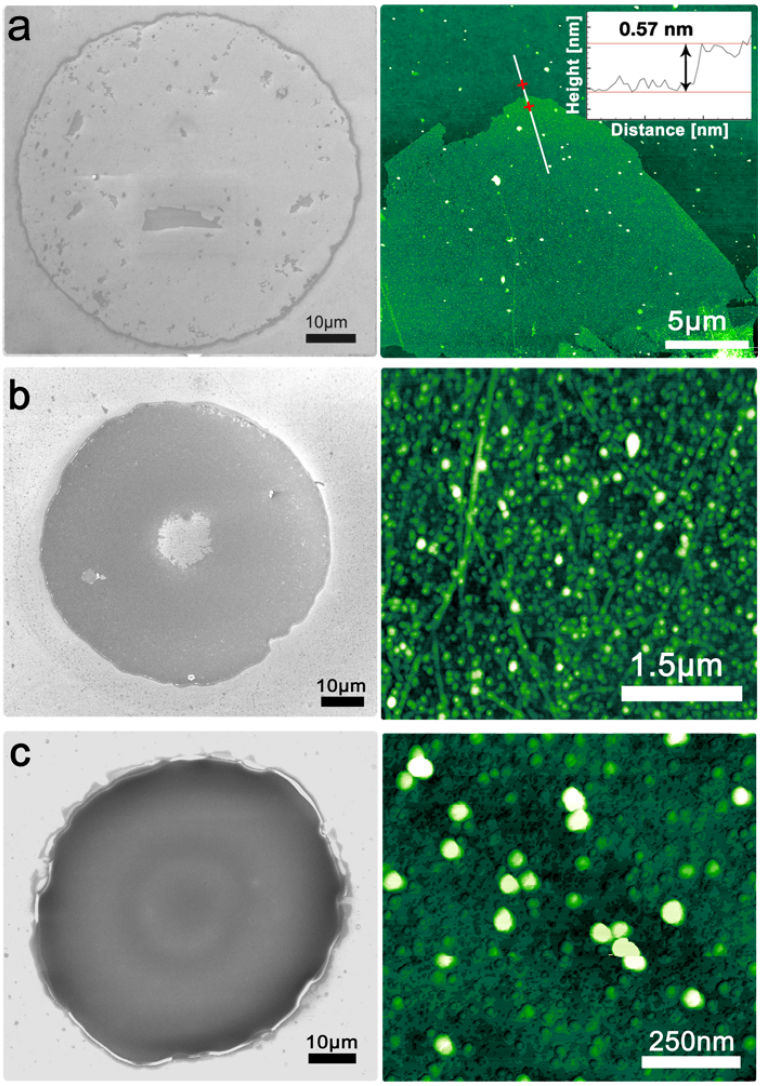

Figure 2.5 a) SEM (left) and AFM (right, false color) images with corresponding line profiles (inset) confirming a step height of less than 1 nm, indicative of chemically converted graphene. b) An SEM (left) and an AFM (right) of a dense network of CNT bundles. c) An SEM (left) and an AFM (right) showing the topology of PCBM aggregates. Figure 2.5 is reprinted with permission[4] © 2010 WILEY-VCH Verlag GmbH & Co. KGaA, Weinheim

This clean transfer process can be used in the low temperature and high throughput fabrication of field effect transistors (FETs) and organic light emitting diodes (OLEDs). For electronic applications, patterned arrays of these carbon nanomaterials could reduce, if not eliminate, parasitic current paths (cross-talk) between neighboring devices.[13]

2.5 Chemical Treatment and Ionic Doping for Enhanced Transparent Electrode Applications

In recent years, there have been several reports discussing graphene's possible uses as a transparent conductor in touch screens, solid-state lighting and solar cells.[14–18] As most graphene produced by CVD and chemical reduction processes have yet to record conductivities high enough for electrode applications, doping of these materials has been studied.[19] Doping processes of CVD graphene with nitric acid, nitro-methane and $AuCl_3$ show characteristics of p-doping,[19–21] while polyvinyl alcohol is reported to n-dope mechanically exfoliated graphene.[22] Doping can reduce the resistance of graphene films to a few hundreds of ohms, bringing it to the range of indium tin oxide. Modification of carbon nanotubes has been carried out using a number of species in the vapor and liquid phases. Thionyl chloride ($SOCl_2$) is a commonly used solvent and inorganic acid known for dehydrating and chlorinating oxygen containing hydrocarbons. Similar effects have been observed in nanotubes exposed to strong inorganic acids such as nitric and sulfuric acids, but these effects are believed to be due to oxidation and removal of surfactant groups.[23] Thionyl chloride is capable of comprehensively modifying the basal planes and open ends of graphitic materials, creating platforms for attachment of a variety of functionalities.[11,24] Previous work has shown that the conductivity of single-walled carbon nanotubes increases upon treatment with $SOCl_2$.[11,15–17] The modification process involves simple immersion either in liquid or vapor phase $SOCl_2$, so the mechanism behind their increased conductivity warrants further analysis. Similarly, the structural similarity with carbon nanotubes makes it logical that graphene and composites of graphene and carbon nanotubes (G-CNT) would be affected by this chemical treatment in an analogous manner. While there have been reports on dopant- or solvent-induced changes in the electronic properties of graphitic materials, there has been a lack of conclusive evidence to explain the improvement in conductivity in chemically converted graphene and graphene-CNT nano-composites treated with $SOCl_2$. In this study, we explore the effects of thionyl chloride on the physical and chemical properties of pristine graphene and examine the changes in the structure and morphology of G-CNT nano-composites that lead to improvements in their transparent conducting properties.[25]

2.5.1 Preparation and Doping of CCG and G-CNT Transparent Conductive Films

The combination of CNTs and CCG into a single mixture results in an overall enhancement in the conductivity, all while sacrificing little in transparency. Interestingly, the sheet resistance values of the combined materials were lower than that of the materials separately. Chemically converted graphene and graphene-carbon nanotube nano-composite films were prepared using previously reported procedures.[14] GO was obtained via oxidation of graphite using Hummers' method, followed by filtration to remove water. The GO paper was then dispersed and reduced in anhydrous hydrazine without surfactants. This dispersion was purified after being mixed for one week to insure complete reaction. The CCG dispersion was then centrifuged at 1500 rpm for 60 minutes and the top 40 μl of the supernatant was collected and diluted with 60 μl of fresh hydrazine to reliably disperse the single sheets.[1,14] Similarly, SWCNTs were weighed out and dispersed into anhydrous hydrazine for one week. The resulting dispersion was centrifuged at 2000 rpm for 60 minutes and the top 40 μl was collected and diluted with fresh anhydrous hydrazine. These two dispersions were then mixed in a ratio of 1 part CCG to 5 parts CNTs, to make G-CNT. A post-treatment process combining ultra-sonication and centrifugation can be used to vary the composition of the dispersions before deposition. Films were then deposited from surfactant-free dispersions in hydrazine onto a myriad of substrates by spin-coating. A mild annealing process, at 110^{0}C, was applied to ensure adequate removal of the solvent. Additional studies on graphene were performed on sheets of mechanically exfoliated graphene, or pristine graphene, which were transferred onto silicon substrates with a thermally grown 300 nm silicon oxide.

Vapor treatments were performed in glass Petri dishes. Substrates with dried CCG, G-CNT composites and pristine graphene were placed into these vapour treatment chambers and ~1 mL of liquid $SOCl_2$ was dispensed into the dishes and around the samples, with care taken to avoid direct contact. We find that extended immersion into thionyl chloride results in complete delamination from the substrate. The dishes were covered and allowed to saturate with vapor at 135°C for at least 15 minutes, or until the vapor had dissipated.

2.6 Analyzing the Effects of Exposure to Thionyl Chloride

2.6.1 Raman Spectroscopy

Raman spectroscopy is a versatile and non-destructive characterization technique for obtaining information on the quality of many poly-aromatic hydrocarbons. The assignment of the D and G peaks, and their overtones, is now a straightforward process that has been discussed at great length.[11,24,26] The Raman spectra of all carbon materials are dominated by sp^2 vibrations, since visible excitations resonate with π states, while sp^3 sites can only be activated upon UV excitation.[11,26] The G peak, which resides at ~1560 cm^{-1}, is a result of bond stretching from all pairs of sp^2 atoms in both rings and chains.

The G-band in graphitic materials typically exhibits a substantial up-shift for electron-acceptor dopants (e.g. bromine, iodine and nitric acid), while displaying a down-shift for electron-donor (e.g. potassium) dopants.[27] Upon exposure to thionyl chloride vapor, electrons originally residing on the graphitic framework are pulled toward the more electronegative atoms, leading to charge redistribution.

Raman spectra were obtained for chemically converted graphene, mechanically exfoliated graphene (pG) and CCG-CNT composites, before and after 15 minutes of thionyl chloride exposure (Figure 2.6). The full width at half maximum (fwhm) for the 2D mode of our pristine graphene was measured to be 33 cm^{-1}, indicating that a single layer was being used for this experiment. Blue shifts in CCG (Figure 2.6 a) from 1595.9 to 1601.1 cm^{-1} (~5.2 cm^{-1}), pristine graphene (Figure 2.6b) from 1587.7 to 1592.5 cm^{-1} (~4.8 cm^{-1}) and G-CNT (Figure 2.6 c) from 1592.1 to 1600.2 cm^{-1} (~8.1 cm^{-1}) were observed, which signifies electron transfer from the graphitic materials to the dopants. The shape of the G band can also be used to understand the changes in the in-plane force constant and determine if a graphene flake has been intercalated.[28] As shown in Figure 2.6 (a-c), no splitting of the G peak is observed, indicting that this anion interaction does not form an intercalation compound. This is important in understanding the role of the anionic dopant in the graphene system. The physical adsorption of anions is a similar effect to that of other halogen dopants such as bromine or iodine, whereas nitric acid and diazonium are believed to intercalate into the graphitic layers.[19] The shape of the G peak in the G-CNT system, see Figure 2.6c, is an exception to the splitting since its shape is a result of combining mostly semiconducting carbon nanotubes with CCG.

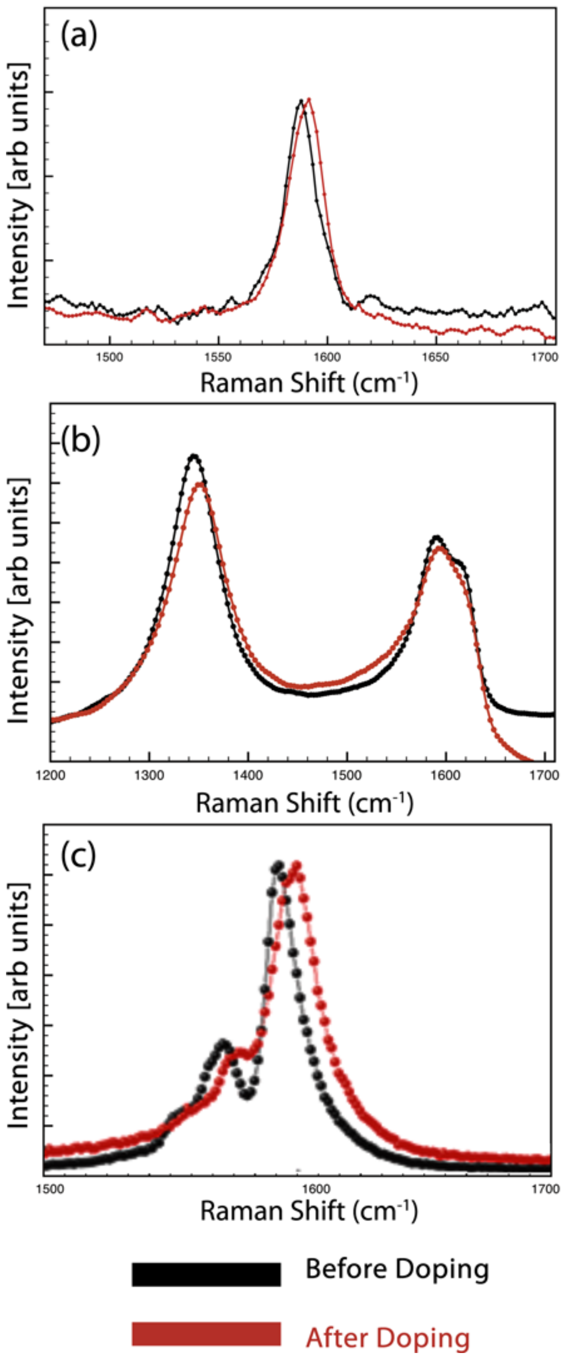

Figure 2.6 An up-shift in the Raman spectrum for the G peak is observed after fifteen minutes of thionyl chloride exposure. (a) A pristine graphene flake red shifts by 5.2 cm^{-1}; (b) a chemically converted graphene flake shifts by 4.8 cm^{-1}; and (c) a CCG-CNT hybrid film red shifts by 8.1 cm^{-1}. Figure 2.6 is reprinted with permission[25] © 2011, Royal Society of Chemistry

2.6.2 Chemical Bonding of Thionyl Chloride to the Graphitic Structures

To gain insight into the effect of thionyl chloride on graphene, XPS and EDX were used to elucidate bonding information on graphene, CCG and G-CNT thin films. The nature of the chemical modification to the graphitic structures was determined by XPS analysis. Spectra were collected for pristine graphene, CCG and G-CNT that were deposited onto silicon substrates with a 20 nm gold layer added on top to avoid charging effects. It has been shown that pristine SWCNT form many C-S bonds and some C-Cl bonds when exposed to liquid $SOCl_2$ at elevated temperatures,[11] so similar doping interactions with pristine graphene were expected. Full core level spectra for all three samples were collected and evidence for C 1s and Cl 2p peaks were found, but an S 2p peak, which was observed in previous experiments with CNTs, was not found. These results suggest that either the curvature and absence of carboxylic acid groups on the CNT allows for molecular interaction of the $SOCl_2$ with the carbon and resulting C-S bonds, or the $SOCl_2$ fully decomposes in the vapor phase. In all instances, the XPS shows the same C 1s (for sp^2 C) and Cl 2p (C-Cl) binding energies. Figure 2.7 (a, b) presents the results for CCG flakes before and after treatment. Our results indicate that the C-Cl interactions form from the doping process, which leads to the overall enhancement in electronic transport.

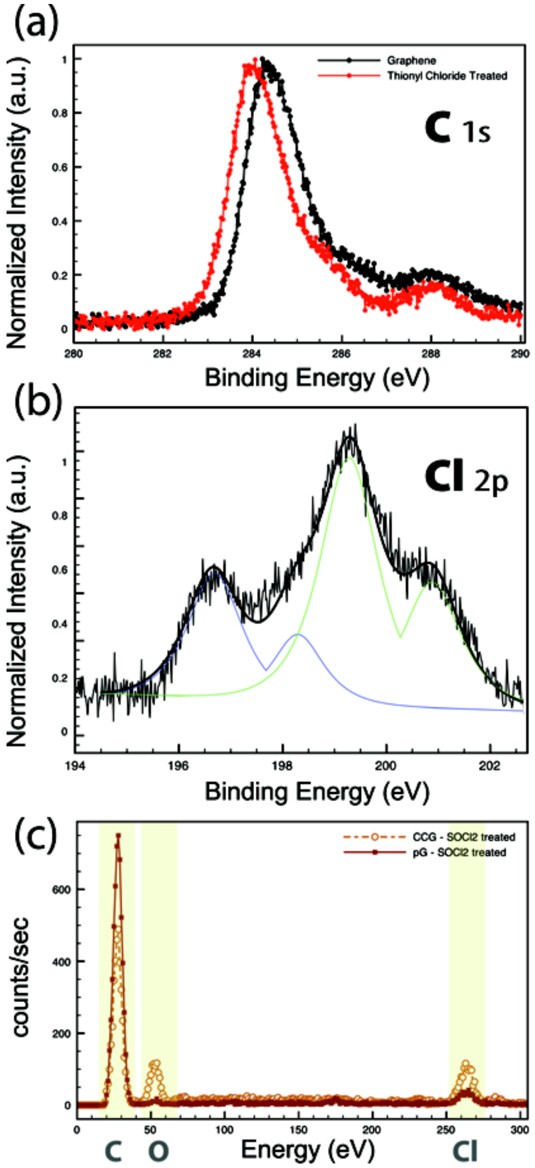

Figure 2.7 X-ray photoemission spectra of thionyl chloride treated graphene materials were taken to probe their chemical bonding: (a) C 1s and (b) Cl 2p of graphene. The chemical composition of the materials was probed, after treatment, using energy dispersive X-ray (EDX) spectroscopy for (c) both mechanically exfoliated pristine graphene (pG) and chemically converted graphene (CCG) to verify the presence of chlorine. Figure 2.7 is reprinted with permission[25] © 2011, Royal Society of Chemistry

The C 1s peak at 284.4 eV for sp^2 carbon shifts by 0.5 eV to a lower binding energy (283.9 eV) after the vapor treatment, indicating that the sp^2 pi system has been affected. The Cl 2p core level spectrum shows two nonequivalent chlorine sites from the 3/2 and 1/2 levels, which are separated by 1.4 eV due to spin-orbit coupling. The more intense peak at ~200.2 eV is a result of Cl participating in C-Cl covalent bonding, while the less intense peak at ~198.8 eV is a result of Cl^- ionic bonds with the carbon on the surface. This is significant as it shows that the graphitic surfaces in the pG, CCG and G-CNT are modified by interactions with the Cl in the thionyl chloride, instead of the S in unfunctionalized CNTs.

To confirm the chemical composition of the modified graphitic species, EDX spectra were collected on both pristine and chemically converted graphene species. Figure 2.7 c verifies that only chlorine, carbon and oxygen (in the case of CCG) on the graphene and G-CNT post-$SOCl_2$ treatment are present. Further analysis with micro-IR spectroscopy reveals the presence of C-Cl bonds in both pristine and chemically converted graphene after vapor exposure to thionyl chloride, as seen in Figure 2.8.

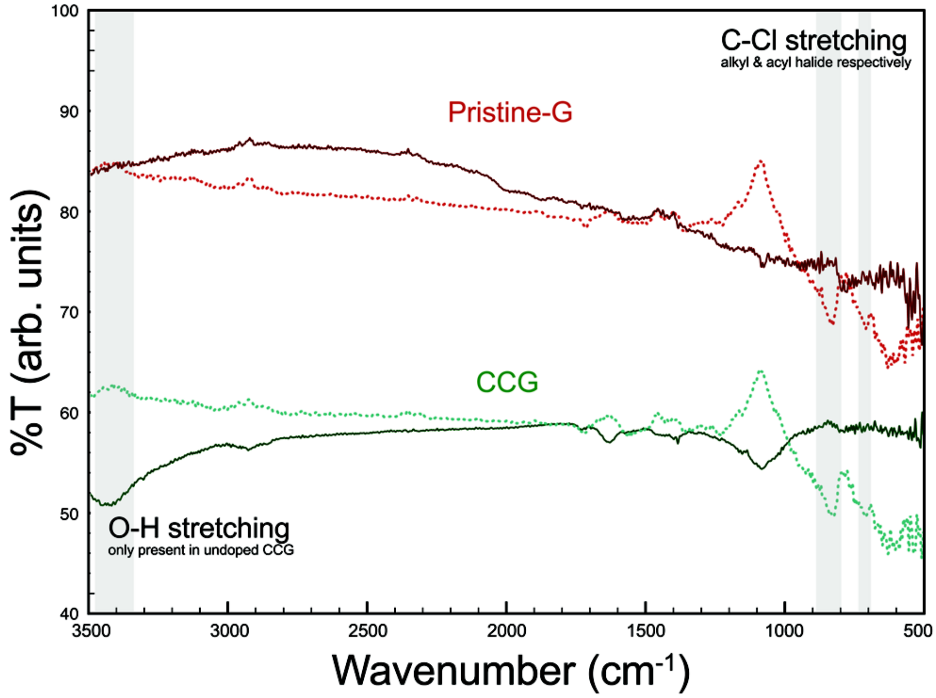

Figure 2.8 IR data for mechanically exfoliated graphene and chemically converted data pre- and post-thionyl chloride treatment, which verifies the presence of C-Cl stretching modes and O-H stretching modes from the oxygen moieties remaining on CCG.

2.6.3 Morphological Changes to G-CNT Composites

The changes in chemical structure can be correlated to the morphology of the composites using scanning electron microscopy (SEM). Thicker multilayer composites were analyzed, and the micrographs show that the treatment promotes not only aggregation and cross-linking among nanotube bundles, but also between the nanotubes and the graphene sheets. These results show that chlorine, not sulfur-bound thionyl chloride must be responsible for this morphological change. SEM images (Figure 2.9) suggest that the chemical modification with $SOCl_2$ facilitates stronger interactions between the carbon nanotubes and graphene (Figure 2.9 a,b). The images of graphene layers alone (Figure 2.9 c, d) show that the thionyl chloride treatment also promotes aggregation between layers and the incorporation of carbon nanotubes clearly provides an additional pathway for 3-dimensional interactions.

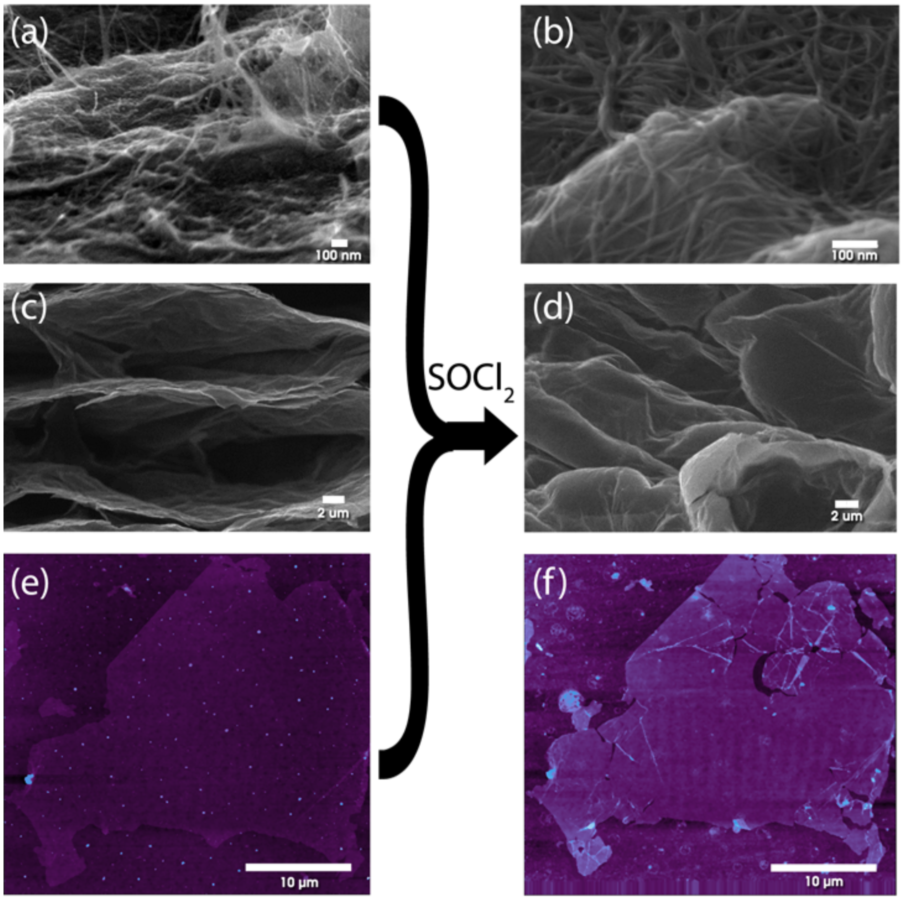

Figure 2.9 Representative scanning electron micrographs (SEM) of graphene-CNTs nanocomposites and CCG and an atomic force micrograph (AFM) of a single CCG sheet. The SEMs of the nanocomposite (a) before, and (b) after $SOCl_2$ treatment indicate that the carbon nanotubes bundle up on top of the graphene layers. (c) SEMs show an increased overlap between graphene layers after (d) doping with $SOCl_2$. AFM images of CCG (e) before and (f) after treatment suggest that exposure to thionyl chloride can be detrimental to the overall fidelity of a graphene flake. This anionic dopant does not induce intercalation and folding, but rather causes rips and wrinkles. Figure 2.9 is reprinted with permission[25] © 2011, Royal Society of Chemistry

The bundling, coupled with the lack of G peak splitting from the Raman spectra suggests that chlorine anions, from thionyl chloride, also act as adsorbents rather than intercalants. AFM images further suggest that instead of folding along preferred crystallographic planes, the graphene flakes slightly wrinkle, and in the case of CCG, they also rip (Figure 2.9 e, f). No significant change in step height was measured on surveying the surface of the CCG with an atomic force microscope tip, implying that either these anions are not strong enough to induce folding or the concentration of the adsorbed vapor was insufficient to induce the type of folding previously seen with bisulfate anions.[28]

2.6.4 Proposed Mechanism of Chloride Anion Doping

Scheme 1 illustrates a proposed reaction mechanism where thionyl chloride interacts in a nucleophilic fashion with a carboxylic acid. In the presence of thionyl chloride, carbonyl oxygen groups can form a chlorosulfite ester intermediate, which readily reacts with nucleophiles, as it is a good leaving group. Upon formation of the acyl chloride, the displaced chlorosulfite ion is unstable and decomposes into SO_2 and Cl^-. Analogous reactions with CCG and carbon nanotubes, where the edges and basal planes are functionalized with hydroxyl and carboxylic functionalities, explain how thionyl chloride modification takes place. In the case of pG, the edges are the preferred reaction sites and would likely chlorinate at terminating carbons.[29]

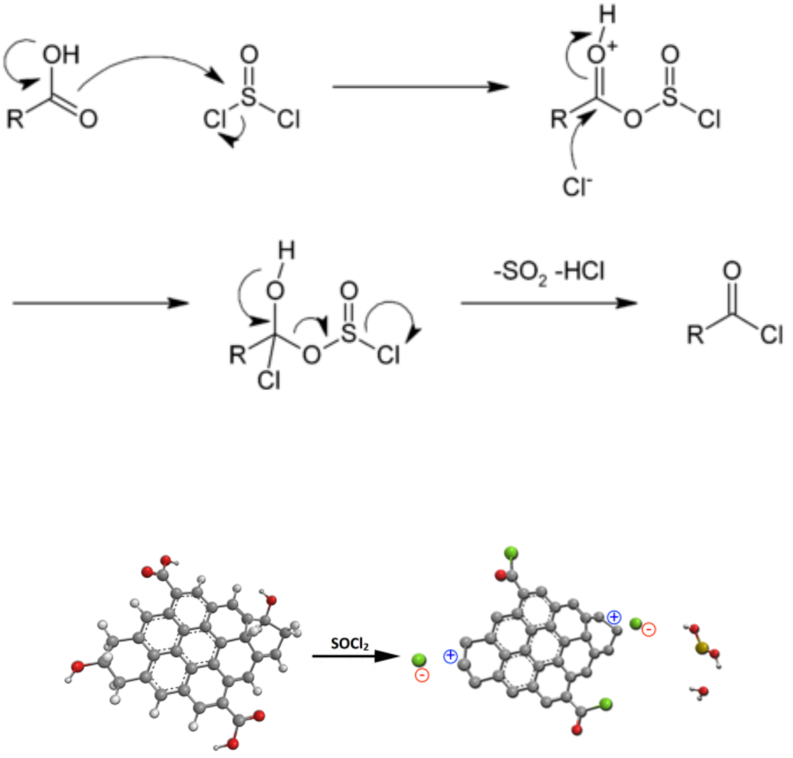

Scheme 2.1 (a) Proposed reaction mechanism in which thionyl chloride undergoes a nucleophilic interaction with a carboxylic acid releasing a chloride, which in turn can functionalize groups present on chemically converted graphenes and oxidized carbon nanotubes. R represents poly-aromatic hydrocarbon species; (b) visualization of how chloride ions (green circles) are bonded to the carbons at the edge of a graphitic base. Scheme 2.1 is reprinted with permission[25] © 2011, Royal Society of Chemistry

The effects of $SOCl_2$ on CNTs have been investigated, and it was found that the doping mechanism occurs predominantly via bonding of sulfur to the graphitic backbone, with very little C-Cl interactions.[19] This doping mechanism was therefore expected for pristine graphene, but that is not the case. We find that this proposed scheme applies only to CCG and functionalized CNTs films. In the case of peeled graphene, chlorine anions formed in the vapor phase readily adsorb onto the surface and react with the delocalized pi system halogenating preferentially along the edges, as they are the most energetically favorable locations.[29] Since chlorination of pristine graphene is possible with thionyl chloride, it is likely that other chlorinating agents will react in a similar fashion.

2.6.5 Optical Transmission and Electrical Conductivity

Maintaining optical transmittance with high conductivity is vital for transparent conductor applications. Nitric acid doping of CNTs and CVD graphene show no significant drop in transmittance, while reducing the resistance by about 60%.[20] However, doping with bromine and iodine imparts a significant drop in transmittance after treatment. Doping with those halogens resulted in ~20% loss in transparency with comparable reductions in resistance. Optical transmittance measurements of G-CNT films across the UV-visible spectrum show that doping with $SOCl_2$ does not affect the transparency of G-CNT films, but it does enhance the electrical properties (Figure 2.10 and Table 2.1). The inset images of a G-CNT substrate before (left) and after doping (right) are shown to visually verify that essentially no change in transparency or film quality has occurred.

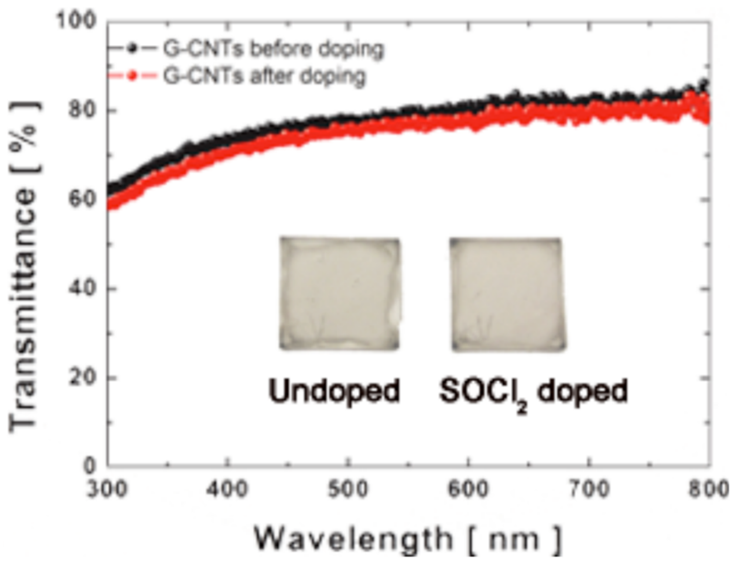

Figure 2.10 Optical transmittance of thionyl chloride treated G-CNT films. Inset: photographic images of a G-CNT substrate before (left) and after doping (right) show essentially no change in transparency. Figure 2.10 is reprinted with permission[25] © 2011, Royal Society of Chemistry

Table 2.1 Optical and electronic properties of G-CNT composite films before and after thionyl chloride treatment. Table 2.1 is reprinted with permission[25] © 2011, Royal Society of Chemistry

G-CNT Sample	Optical Transmittance	Sheet Resistance	Peak Raman Intensity
Untreated	82 %	425 Ω/□	1592 cm^{-1}
$SOCl_2$ doped	82 %	103 Ω/□	1600 cm^{-1}

To further characterize the electronic properties of the different graphenes, flakes of CCG and pG were placed onto aligned substrates and gold electrodes were patterned using e-beam lithography. The resistance data were collected before and after exposure to $SOCl_2$ (2.11 a,b). As metals are susceptible to corrosion when exposed directly to thionyl chloride, *in vacuo* gate modulation measurements were not collected to observe the shift in the Dirac point from its origin. Nevertheless, we found appreciable resistance drops, and attribute them to the adsorbed chlorines along the basal plane of both graphene sheets, which ionically contribute holes to the conjugated sp^2 network. Additionally, the enhanced properties are believed to arise from C-Cl bonds resulting from newly formed charge-transfer complexes. Figure 2.11c shows a computer-generated illustration of a graphene sheet being decorated with chlorine along the edges and basal plane, which increase the number of holes in the conjugated sp^2 network.

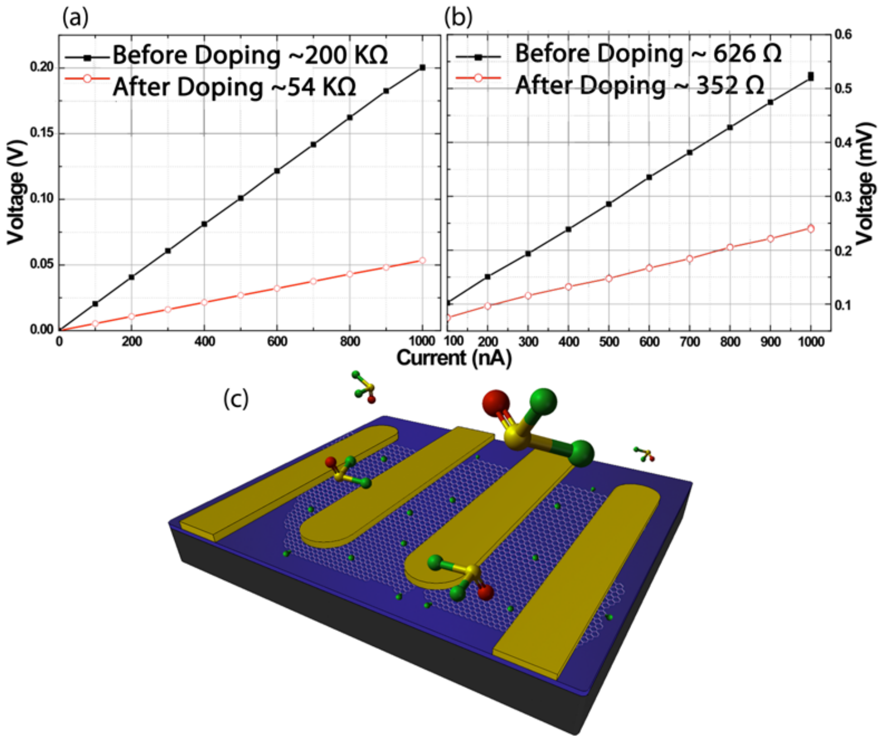

Figure 2.11 Four-point probe measurements taken across single CCG and pG flakes of similar dimensions show a significant decrease in resistance after doping. (a) A single CCG flake shows an ~73% decrease in resistance, while (b) mechanically exfoliated graphene shows an ~44% decrease in sheet resistance. (c) A computer generated illustration of a graphene sheet being decorated with chlorine along the edges and basal plane, which increases the number of positive charge carriers in the conjugated sp^2 network. Figure 2.11 is reprinted with permission[25] © 2011, Royal Society of Chemistry

While the bonding in pristine graphene is exclusively sp^2 carbon, chemically converted graphene contains residual oxygen moieties, which can be readily functionalized for other applications. It was therefore assumed that pristine graphene would be less responsive to chlorination and more susceptible to sulfonation, as seen for other graphitic systems. However, based on the XPS, EDX and Raman spectra, we conclude that vapor-phase thionyl chloride decomposes more readily and the resulting chlorine anions can effectively chlorinate oxygen-containing graphene through a dehydration mechanism and the edges of peeled graphene through halogenation reactions. Additionally, chlorine anions adsorb onto the basal plane of graphene, which also enhance the p-type behavior of the graphitic systems. Electrons residing on graphene are drawn towards the chlorine, which creates hole charge carriers in the graphitic systems and leads to a substantial decrease in resistance. Another reason for the increase in conductivity stems from morphological changes in the graphene thin films, which brings the sheets into closer proximity to each other. In addition to enhancing the electrical properties, we observe that the transparency of the G-CNT films is preserved. SEM and AFM images indicate that this vapor treatment can lead to wrinkles and induce aggregation of sheets and carbon nanotubes when they are in close proximity to each other. These results provide insights into the mechanism of functionalization of graphene and carbon nanotubes with vapor-phase ions and demonstrate a simple method to improve conductivity without sacrificing transparency of graphitic films.

2.7 Conclusions and Future Outlook

Solution processing CCG in hydrazine represents a straightforward and scalable method to make a graphene derivative useful for transparent electrode applications. The work presented in this chapter further demonstrates a method to solution process fullerenes and carbon nanotubes, and hybrid mixtures of them. The materials can be solution processed individually or together and stenciled into desired locations using PDMS elastomeric membranes. This method is certainly not limited to the materials described here and could be extended for patterning other solvent dispersed derivatives of fullerenes, carbon nanotubes and graphene layers. Chemical exposure, specifically thionyl chloride, provides pathways for improving the overall electronic properties of graphitic structures. With future work, the strategies outlined here are capable of delivering entirely carbon-based flexible electronic platforms that represent the building blocks for new and exciting nano-electronic and energy storage materials.

References

1. Tung, V. C., Allen, M. J., Yang, Y. & Kaner, R. B. High-throughput solution processing of large-scale graphene. *Nature Nanotechnology* **4**, 25–29 (2009).

2. Jr, W. H. & Offeman, R. Preparation of graphitic oxide. *Journal of the American Chemical …* **208**, 1937 (1958).

3. Chen, L.-M., Hong, Z., Li, G. & Yang, Y. Recent Progress in Polymer Solar Cells: Manipulation of Polymer: Fullerene Morphology and the Formation of Efficient Inverted Polymer Solar Cells. *Adv. Mater.* **21**, 1434–1449 (2009).

4. Wassei, J. K. *et al.* Stenciling Graphene, Carbon Nanotubes, and Fullerenes Using Elastomeric Lift-Off Membranes. *Advanced Materials* **22**, 897–901 (2010).

5. Zhou, Y., Hu, L. & Grüner, G. A method of printing carbon nanotube thin films. *Appl. Phys. Lett.* **88**, 123109 (2006).

6. Artukovic, E., Kaempgen, M., Hecht, D. S., Roth, S. & Grüner, G. Transparent and flexible carbon nanotube transistors. *Nano Lett.* **5**, 757–760 (2005).

7. Kordás, K. *et al.* Inkjet printing of electrically conductive patterns of carbon nanotubes. *Small* **2**, 1021–1025 (2006).

8. Vijayaraghavan, A. *et al.* Ultra-large-scale directed assembly of single-walled carbon nanotube devices. *Nano Lett* **7**, 1556–1560 (2007).

9. Briseno, A. L. *et al.* Patterning organic single-crystal transistor arrays. *Nature* **444**, 913–917 (2006).

10. Jackman, R., Duffy, D., Cherniavskaya, O. & Whitesides, G. Using elastomeric membranes as dry resists and for dry lift-off. *Langmuir* **15**, 2973–2984 (1999).

11. Dettlaff-Weglikowska, U. *et al.* Effect of SOCl2 treatment on electrical and mechanical properties of single-wall carbon nanotube networks. *J. Am. Chem. Soc.* **127**, 5125–5131 (2005).

12. Campoy-Quiles, M. *et al.* Morphology evolution via self-organization and lateral and vertical diffusion in polymer: fullerene solar cell blends. *Nat Mater* **7**, 158–164 (2008).

13. Dickey, K. C. *et al.* Large-area patterning of a solution-processable organic semiconductor to reduce parasitic leakage and off currents in thin-film transistors. *Appl. Phys. Lett.* **90**, 244103 (2007).

14. Tung, V. C. *et al.* Low-Temperature Solution Processing of Graphene−Carbon Nanotube Hybrid Materials for High-Performance Transparent Conductors. *Nano Letters* **9**, 1949–1955 (2009).

15. Lee, K. *et al.* Single Wall Carbon Nanotubes for p-Type Ohmic Contacts to GaN Light-Emitting Diodes. *Nano Letters* **4**, 911–914 (2004).

16. Wu, Z. *et al.* Transparent, conductive carbon nanotube films. *Science* **305**, 1273–1276 (2004).

17. Pasquier, A. Du, Unalan, H. E., Kanwal, A., Miller, S. & Chhowalla, M. Conducting and transparent single-wall carbon nanotube electrodes for polymer-fullerene solar cells. *Applied Physics Letters* **87**, 203511 (2005).

18. Wassei, J. K. & Kaner, R. B. Graphene, a promising transparent conductor. *Materials Today* **13**, 52–59 (2010).

19. Kasry, A., Kuroda, M., Martyna, G., Tulevski, G. & Bol, A. Chemical doping of large-area stacked graphene films for use as transparent, conducting electrodes. *Acs Nano* **4**, 3839–3844 (2010).

20. Bae, S. *et al.* Roll-to-roll production of 30-inch graphene films for transparent electrodes. *Nature Nanotechnology* **5**, 574–578 (2010).

21. Kim, K. K. *et al.* Enhancing the conductivity of transparent graphene films via doping. *Nanotechnology* **21**, 285205 (2010).

22. Blake, P. *et al.* Graphene-based liquid crystal device. *Nano Lett.* **8**, 1704–1708 (2008).

23. Geng, H. Z. *et al.* Effect of Acid Treament on Carbon Nanotube-Based Flexible Transparent Conducting Films. *J. Am. Chem. Soc.* **129**, 7758–7759 (2007).

24. Hamon, B. M. A., Chen, J., Hu, H. & Chen, Y. Dissolution of Single-Walled Carbon Nanotubes. *Advanced Materials* **0055**, 834–840 (1999).

25. Wassei, J. K., Cha, K. C., Tung, V. C., Yang, Y. & Kaner, R. B. The effects of thionyl chloride on the properties of graphene and graphene–carbon nanotube composites. *Journal of Materials Chemistry* **21**, 3391 (2011).

26. Eda, G., Fanchini, G. & Chhowalla, M. Large-area ultrathin films of reduced graphene oxide as a transparent and flexible electronic material. *Nature nanotechnology* **3**, 270–274 (2008).

27. Rao, A. M., Eklund, P. C., Bandow, S. & Thess, A. Evidence for charge transfer in doped carbon nanotube bundles from Raman scattering. *Nature* **191**, 257–259 (1997).

28. Allen, M. *et al.* Chemically induced folding of single and bilayer graphene. *Chemical Communications* 6285–6287 (2009).

29. Wang, X. *et al.* N-doping of graphene through electrothermal reactions with ammonia. *Science* **324**, 768–771 (2009).

Chapter 3: Bottom Up Synthesis of Graphene

3.1 Switching Synthetic Methods: An Alternative Strategy for Isolating Large Area and Highly Crystalline Graphene

As mentioned in the previous chapter, there were numerous accounts detailing the synthesis of graphene using solution-based methods. The chemical reduction of graphene oxide sheets into CCG can indeed produce large and scalable quantities, which are useful for thin film applications and more recently energy storage.[1–3] The drawback from this approach is that the electrical properties do not rival those of exfoliated natural graphite. This is largely due to a combination of two factors. First, the basal plane of the graphite lattice is irreparably damaged during the oxidation process – imagine crumpling a sheet of paper and then trying to smooth it out afterwards.[4,5] Second, the reduction to reduced graphene oxide, or CCG, produces point defects and vacancies in the lattice.[6,7] Indeed, several groups have successfully demonstrated impacting applications to utilize this material, mainly where high surface area is required.[3,5] The take home message is that solution processing routes to graphene produce derivatives, analogous to what PCBM is to buckminsterfullerene.[8]

In 2010 research teams took a step back to survey the progress.[9] After sifting through the developments, one method in particular emerged as a viable route to make a more pristine graphene-like material, Chemical Vapor Deposition (CVD). Graphene has been grown on a variety of metals, for example Ru, Ir, Ni and Cu.[10–13] Interestingly, the synthesis of monolayer graphite or graphene on metal surfaces has been investigated since the 1970's.[14] They attribute this deposition to the solubility of carbon into these metals as a key component in the synthesis, and the stability/bonding of the monolayer graphite on the surface can be ascribed to electron transfer from the substrate into the π band of graphene.[15] Early in its development, the CVD process typically yielded a monolayer with polycrystalline domains, each being relatively small. After a few years of intense optimization, it was found that CVD of graphene can produce large domains, up to the millimeter scale, having the same properties as the exfoliated counterpart.[16] The synthesis of graphene via CVD is still somewhat of a Pandora's box, because there are so many variables, but theories suggest that copper (111) is the best surface to grow graphene[17,18] (likely related to the orientation of the available d-orbitals on copper) and that suppressing the loss of copper, due to pressure variations and high temperature migration, allow the formation of large domains.[16]

There is still much work to be done in this area, if graphene is ever to make the impact researchers initially promised. First, graphene synthesis needs to be performed at low temperatures if it can be integrated into standard chip processing (ICP). Next, a more reliable and less destructive method to transfer graphene must be found, such that the catalyst-loss is significantly reduced. Finally, a method to selectively augment regions with other elements should be realized, such that the band structure can be reliably controlled. It is likely that these three landmarks will be achieved in the near future, but there are still many ways to exploit the materials created along the way.

3.2 Building a Chemical Vapor Deposition Reactor

Chemical Vapor Deposition is a generic name for a group of processes that involve the deposition of a solid material from a gaseous phase and is similar to physical vapor deposition (PVD), albeit the PVD process uses solid precursors that are then vaporized and deposited. This thin film process takes place at the molecular level building from the "Bottom-up", driven by thermodynamics and kinetics of the precursor chemistry, the dynamics of heat and mass transport and the physics of surface adsorption and crystal growth. This process yields coatings that are of high purity and never more than a few microns in thickness. In the gas that produces graphene, it is ideal to control the deposition of atomic layers. There are also several variations to the CVD process, such as: atmospheric pressure, low pressure, metal-organic, plasma-assisted, laser and photochemical Chemical Vapor Deposition; chemical vapor infiltration and chemical beam epitaxy. For the CVD synthetic process, much of the learning curve is a result of acquiring an intimate knowledge of vacuum system, surface science, fluid and thermodynamics. Background reading, for those mentioned topics, can be found in the following textbooks:

1. Jousten, Karl. Handbook of Vacuum Technology. Wiley-VCH, 2008. Hardcover
2. Somorjai, Gabor and Li, Yimin. Introduction to Surface Chemistry and Catalysis. Wiley, 2nd Edition, 2010. Hardcover
3. Masel, Richard. Principles of Adsorption and Reaction on Solid Surfaces. Wiley-Interscience, 1996. Hardcover

A typical CVD system includes: a gas delivery system, reactor chamber, substrate bay, energy source (resistive heating coils, radiant heating halogen lamps, radio frequency induction heaters and laser), vacuum system, exhaust system, exhaust treatment system and process control equipment. Once a system is in place, precursor gasses are delivered into the reaction chamber and there they pass over or come into contact with a heated substrate or chamber. The act of reaching the substrate is called passing the “boundary layer”, consisting of gaseous “fluids” composed of carrier gas at a given pressure. The precursors will inevitably react and/or decompose and then form a solid phase, which is absorbed into or adsorbed onto the substrate. Controlling the thermodynamics of the system plays a critical role in this process and can influence reactions that can take place. The components of the CVD system built in the Kaner laboratory, at UCLA is described below in Figure 3.1. The schematic is made up of several components to control: the flow rate of the gasses, system pressure and temperature of the reactor. The rounded square enclosure in Figure 3.1 represents the area that should be mounted on a wall and stable bench top.

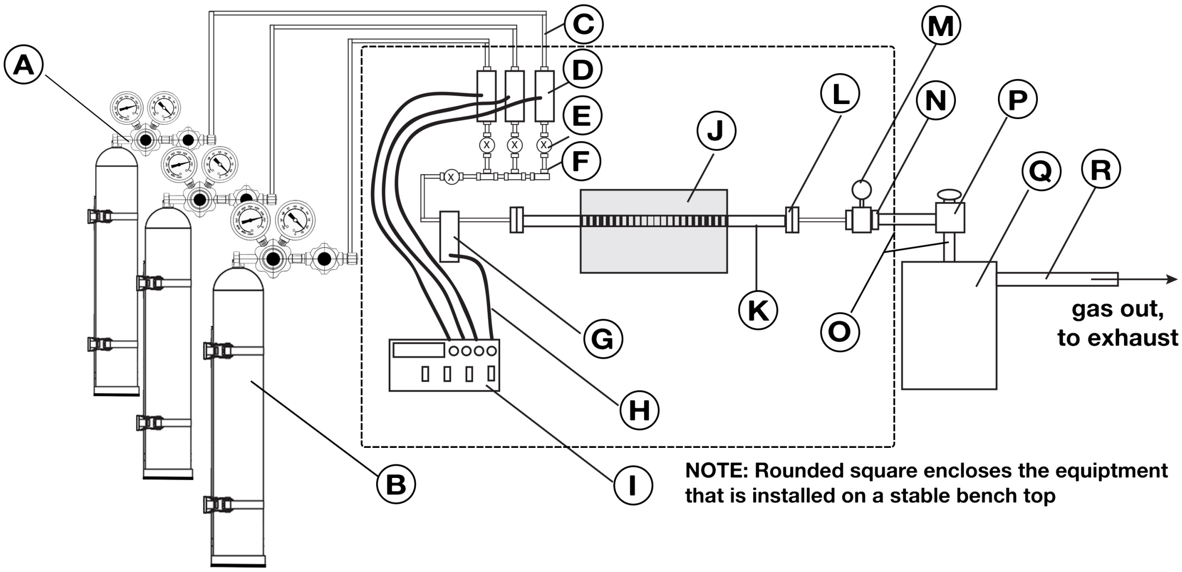

Figure 3.1 Schematic of a Chemical Vapor Deposition reactor that can be used to grow graphene.

To control the flow rate of a system, regulators and mass flow controllers are required. The gas sources for graphene synthesis are generally high purity methane, hydrogen and argon, which are injected into the system from pressurized tanks (B) and specialized regulators (A). The gases flow through stainless steel tubes (C) connected with VCR® (preferred for ultra-high vacuum) or Swagelok® fittings (F). The tubes with gasses are then directed towards and into mass flow controllers (D), which regulate the flow rate of the gasses when connected to the power source (I). The power sources, generally serve dual purposes to also shut off and on the gases at (D); however, the gasses can be turned on and off manually using needle valves (E). Once the gasses are flowing, the pressure throttle is used to monitor and regulate the pressure of gas via a moving butterfly valve. Once a desired gas pressure set point and flow rate are established, they flow through quartz tubes (K), connected with metal/glass fittings (L) and into the heated reactor zone (J) and reacts with, in this case metal catalysts, to graphitize carbon precursors into graphene. The gasses exit the reactor and the pressure can be monitored again using a robust Pirani gauge (M), which monitors the gasses pressures in terms of thermal conductivity. The Pirani gauge is fitted onto the system using HPS ISO-KF® fittings. The gasses can be scrubbed at this point using a cold trap or catalyst scrubber attachment, placed between (N) and (P). The gasses can be trapped in the reactor at any given point by closing off the needle valve at (E) and the Bellows® valve (P). The gasses exit the system through the vacuum pump (Q) and to exhaust at (R).

3.3 Chemical Vapor Deposition of Graphene from a Range of Hydrocarbon Precursors

3.3.1 Impetus for Using Copper Catalysts to Grow Monolayer Graphite

Since the first practical demonstration in 2009, Chemical Vapor Deposition (CVD) of graphene on nickel and copper substrates has become a widely utilized method for synthesizing large-area graphene.[12,19] While mostly monolayer graphene can be grown, small variations in the growth conditions have large effects on the properties of the final graphene produced.[20] Conditions such as the substrate metal, the system pressure, and the chemical precursor each factor into the quality of CVD-grown graphene. Nickel was the first metal catalyst shown to produce graphene, but it is very difficult to avoid multilayer growth. Li et al. demonstrated the growth and isolation of single-layer graphene on copper and showed that the process is self-limiting at low pressure due to the lower solubility of carbon in copper.[20] In contrast, growth on copper at atmospheric pressure can result in multilayer growth.[21,22] While methane is the most studied carbon source for CVD of graphene, graphene of comparable quality can be made using liquid and solid carbon feedstock's as well as olefin gases.[23–27]

Several factors are important in controlling the number of layers of CVD-grown graphene. Although, bilayer graphene has recently been grown from methane by varying the cooling time,[23] the reductive gas flow,[28] the growth time[29] and epitaxially[30] via an additional growth process in the presence of a fresh copper foil, there is little explanation fully describing the mechanism of bilayer graphene growth.[23,28–30] Since extended growth times are required for secondary growth, it seems likely that the concentration of the precursor gas plays a critical role in controlling the number of layers.

To study the effect of carbon concentration from alkane gases on graphene growth, we investigate ethane and propane hydrocarbon precursors, which contain two and three times more carbon than methane, respectively. The growth pressures were varied (250 – 1000 mTorr), while other conditions such as flow rate, temperature and time were fixed. In the present work, mono- and bilayer graphene are controllably grown on high purity copper foils using ethane, while propane produces single to few layer and turbostratic graphene.

Using fixed flow-rates, temperature, growth and cooling times, we systematically varied the pressure of the hydrocarbon precursors to examine the effect of carbon concentration. We find that larger aliphatic hydrocarbon gases at relatively low-pressure (<1 Torr) can produce single, bilayer and multilayer graphene, whereas methane only forms single layer graphene. We characterize and compare the graphene with optical microscopy, scanning electron microscopy and transmission electron microscopy (TEM), Raman spectroscopy and UV-Vis spectroscopy. The data provide insight into the growth mechanism of single and bilayer graphene on copper. To our knowledge, this is also the first report discussing CVD of graphene on copper using ethane and propane feedstock gases.

3.3.2 Characterizations and Analysis

Graphene films were separated from the copper catalyst supports through a transfer process, explained in Section 3.3.5, and placed onto various substrates for analysis. Figure 3.2 shows optical micrographs (OM) of graphene samples that were grown with methane, ethane and propane and were transferred onto silicon substrates with a 300 nm oxide layer. For all growths with methane, the graphene films are visually the same. Interestingly, the larger hydrocarbon precursors produce films that appear to have a variation of color contrast under the optical microscope. This color variation is a result of additional layers interfering with the reflected light.[31] The data, in Figure 3.2, suggest a trend that higher concentrations of carbon from ethane and propane, result in thicker films of varying quality. Another interesting result is the films grown with propane (Figure 3.2 g, h and i) yield multilayer graphene. In fact, these layers can be stripped away mechanically and even under a gentle flow of air. The bright pink area shown in Figure 3.2 indicates the true thickness of the film, while the dark gold regions are where the graphene layers have been stripped away.

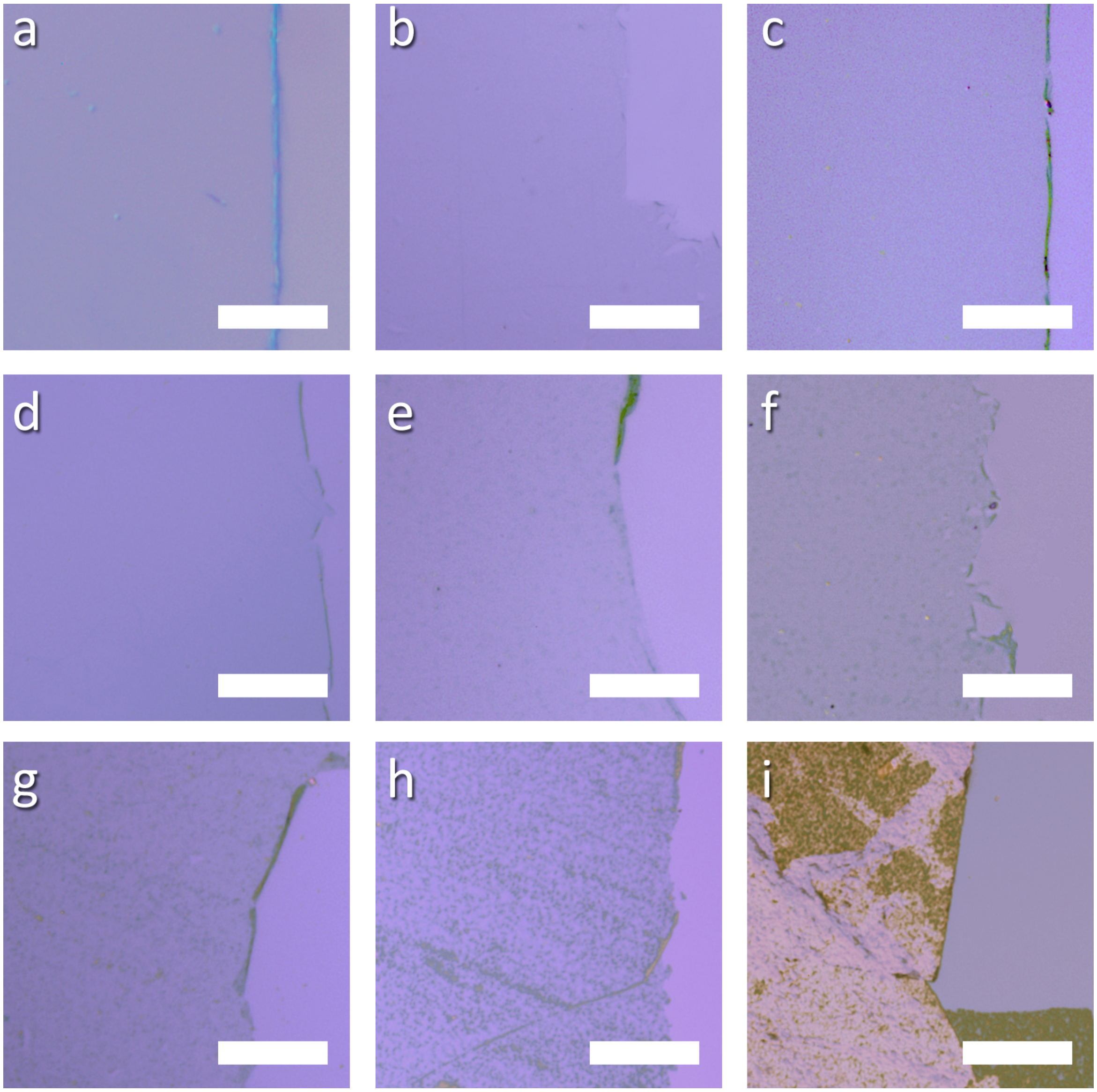

Figure 3.2 Optical micrographs of graphene grown with methane (a-c), ethane (d-f) and propane (g-i) at 250, 500 and 1000 mTorr growth pressures, respectively. The graphene was transferred onto a silicon substrate with a 300 nm oxide layer. Scale bar represents 20 µm. Figure 3.2 reprinted with permission, copyright © 2012 WILEY-VCH Verlag GmbH & Co. KGaA, Weinheim

The graphene grown from ethane gas shows a significant change when the pressure is increased; bilayer graphene becomes the dominant form. High-resolution SEM images of ethane-synthesized graphene (Figure 3.3) reveal darker, more conductive bilayer regions covering the first layer. Since the only variable changed was the growth pressure, we attribute the additional growth to a higher concentration of carbon during the reaction. The SEM images of ethane-grown graphene were used, in conjunction with ImageJ freeware, to calculate the type and percent coverage of graphene based on relative color intensities. The analysis infers that up to 75% bilayer graphene can be grown with ethane at 1000 mTorr pressure, and is graphed in Figure 3.3f. Within these growth conditions, methane yields single layer graphene, therefore SEM analysis was not performed. SEM images of graphene grown with propane can be seen in Figure 3.4 and show that single layer growth is much more difficult to obtain. Instead, growths of multilayer graphene and turbostratic graphene, as explained later, are observed within these parameters.

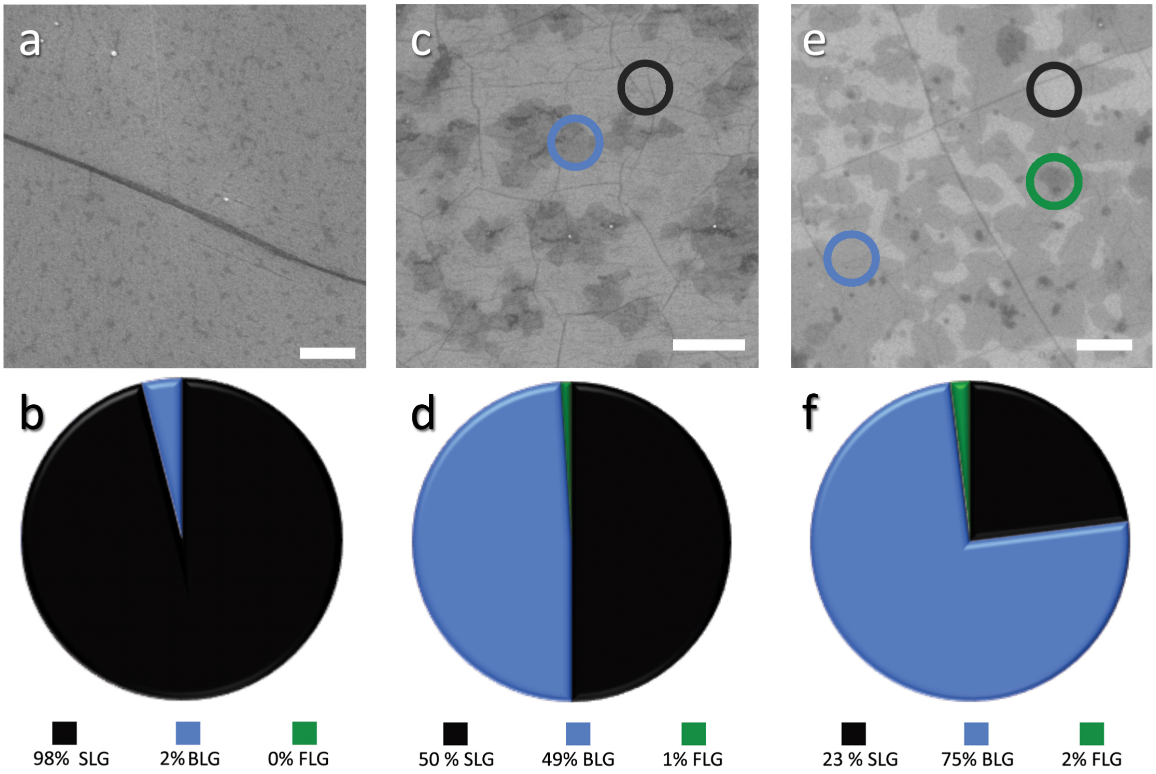

Figure 3.3 Scanning electron micrographs of graphene grown with ethane at increasing pressures (250, 500 and 1000 mTorr, respectively) show the appearance and growth of a second layer. These films were transferred onto silicon wafers with a 300 nm thick silicon dioxide layer. Coverage statistics (b, d, f) were tabulated and graphed to illustrate the growth trends of graphene layers at different pressures. At 250 mTorr (a) a single layer (black circle) is controllably grown, but at 500 mTorr (c) ~49% bilayer coverage (blue circle) is observed with 1% few layer graphene (green circle) and at 1000 mTorr (e) ~75% bilayer coverage is observed with small regions containing ~2% few layer graphene. Scale bars represent 1 μm. Figure 3.3 reprinted with permission, copyright © 2012 WILEY-VCH Verlag GmbH & Co. KGaA, Weinheim

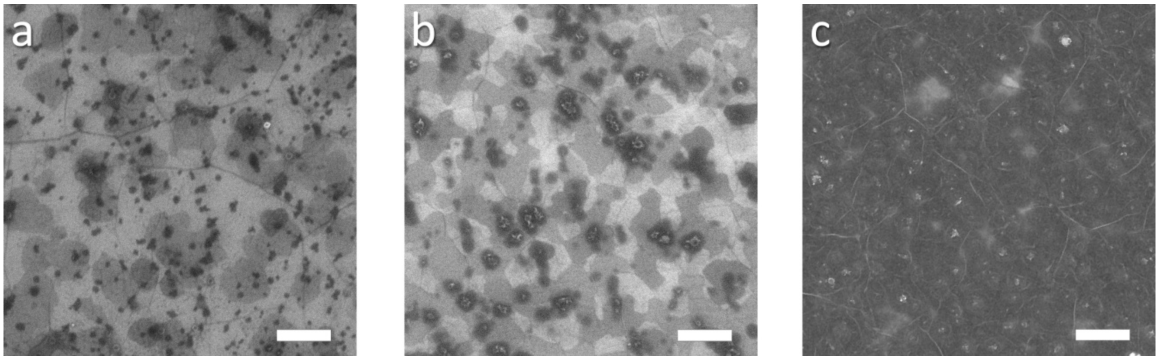

Figure 3.4 Scanning electron micrographs (SEM) of graphene grown with propane at increasing pressures (250, 500 and 1000 mTorr, respectively) show the growth trend of graphene with a larger hydrocarbon gas. These films where transferred onto silicon wafers with a 300 nm thick silicon dioxide layer. At 250 mTorr growth conditions (a) there is evidence for bilayer graphene, seen as dark regions. At 500 mTorr (b) the bilayer region coverage increases and the larger dark spots, indicative of few layer graphene, become more prevalent. Finally, at 1000 mTorr growths (c), the number of layers dramatically increases. Scale bar represents 1 μm. Figure 3.4 reprinted with permission, copyright © 2012 WILEY-VCH Verlag GmbH & Co. KGaA, Weinheim

Raman spectroscopy was used to assist in quantitatively determining the number of layers of graphene and to gauge the crystallinity by noting changes in the spectral fingerprint.[32] Again, the graphene was transferred onto silicon with a 300 nm oxide layer. Full Raman characterization for all gases can be found in Figure 3.5. Graphene growths with methane (at all pressures) show the characteristic Raman signals for single layer graphene and have expected G:2D peak intensities of roughly 0.25 - 0.30. The graphene grown from ethane, as described in more detail later, shows single and bilayer Raman signatures that vary as the pressure is increased. The Raman spectra resulting from propane show the presence of a D (~1345 cm^{-1}) and a D' (~1615 cm^{-1}) peak budding from the G peak. Furthermore, the intensity of the D peak linearly increases with the growth pressure of propane. The increasing disorder is suggestive of turbostratic graphene,[31] (rotationally disordered multilayer graphene) and also graphene with sp^3 defects.[21] We attribute the lower crystallinity of the films to oversaturation from carbon species and from different cracking pathways of the precursors, as described later.

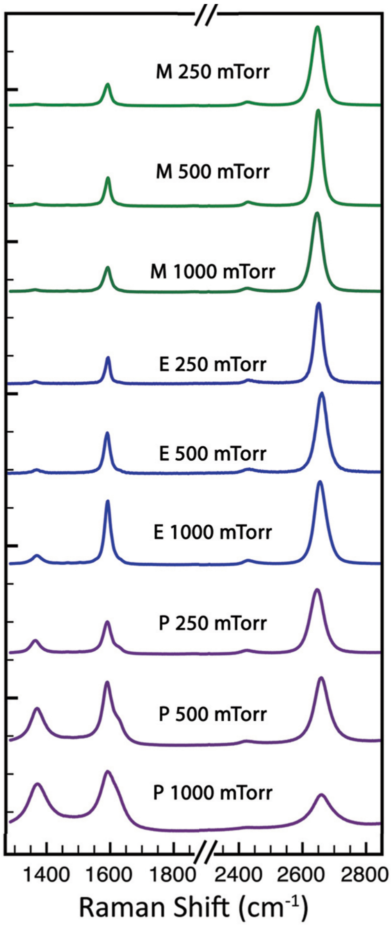

Figure 3.5 Raman spectra of graphene films grown at different pressures and with different hydrocarbon precursors. (a) Spectra were measured with a low power laser, at wavelength of 514 nm and laid out in sequence to show an overall trend in graphene crystallinity as a function of pressure (M–methane, E–ethane and P-propane). Figure 3.5 reprinted with permission, copyright © 2012 WILEY-VCH Verlag GmbH & Co. KGaA, Weinheim

The growth of bilayer graphene from ethane was studied with Raman spectroscopy as a function of pressure. Figure 3.6 show that ethane-grown graphene exhibits a significant change in the 2D band as the pressure is increased from 250 to 1000 mTorr. The spectra were normalized so that the G peaks are of equal intensity. At pressures of 500 and 1000 mTorr, the 2D peaks change in shape, width, position and intensity, indicative of additional layers. The full width at half maximum (FWHM) of the 2D peaks (Figures 3.6b,c) are up-shifted, broader, asymmetric and contain 4 Lorentzian bands; a result of interactions between the graphene planes.[33–35] The 2D peaks, of graphene grown with ethane at pressures of 250-1000 mTorr, were further analyzed through Raman contour mapping of a 400 μm^2 region (Figure 3.6d). The bar below each map displays values in wavenumbers (cm^{-1}). The FWHM values of the ethane-grown graphene increases as a function of pressure from ~33 cm^{-1} at 250 mTorr, to ~50 cm^{-1} for 1000 mTorr (see also Figure 3.12), and are in good agreement with values obtained by other groups.[23,29]

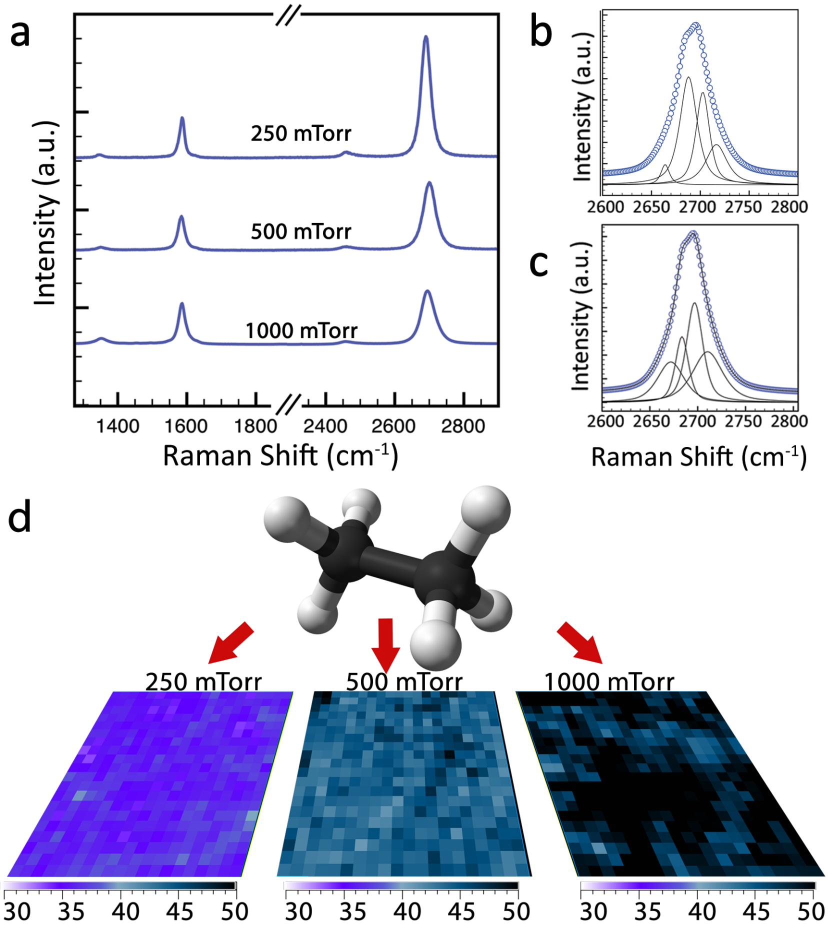

Figure 3.6 Raman spectra and maps of graphene films grown at different pressures using ethane. (a) Raman spectra placed in sequence show changes in the G and 2D ratio- as a function of pressure. Lorentzian fits of the full-width at half maximum from the 2D peaks for graphene grown with ethane at (b) 500 mTorr and (c) 1000 mTorr show that the 2D band is split into 4 components: $2D_{1B}$, $2D_{1A}$, $2D_{2A}$, $2D_{2B}$, indicative of bilayer interaction. (d) Raman mapping over a 20 x 20 μm^2 scan area for the FWHM of the 2D peak shows single to bilayer graphene areas at different pressure growths with ethane gas. The values of the color gradient bars below are in wavenumbers (cm^{-1}). Figure 3.6 reprinted with permission, copyright © 2012 WILEY-VCH Verlag GmbH & Co. KGaA, Weinheim

Transmission electron microscopy is a powerful tool to ascertain crystallographic information and also to determine the number of graphene layers. Unlike high-resolution TEM images, which have been typically used to show the graphene edges, selective area electron diffraction (SAED) patterns have the benefit of allowing one to not only differentiate single from bilayer graphene, but also the type of stacking (AA vs. AB). Briefly, single and bilayer graphene can be quantitatively identified by peak intensities; the former has a two atom and the latter a four-atom basis set. The structure factor calculated using these basis values allows us to determine whether the peak intensities are from single layer or bilayer graphene. Additional distinction between single and bilayer graphene can be obtained by measuring the diffraction peak amplitude as a function of reciprocal space distance. After correcting for the Rutherford cross-section and the Debye Waller effects, the structure factor of the basis for single layer graphene has a 4-1 value (between the first and second order diffraction peaks) and a 16-1 value for AB bilayer graphene. Simply, the diffraction intensity line profiles, collected from SAED patterns, will distinguish single from bilayer graphene based on the relative intensities of the inner and outer peaks.

TEM samples were prepared by transferring the resulting graphene on top of a specially prepared silicon nitride support with a thin amorphous silicon dioxide window (~20 nm thick), which accounts for the diffuse rings seen in the diffraction patterns. The diameter of the illuminated area in each SAED pattern is ~250 nm. Diffraction patterns shown in Figure 3.7 a-e correspond to graphene grown at 1000 mTorr with methane, 250 – 1000 mTorr with ethane and 250 mTorr with propane, respectively.

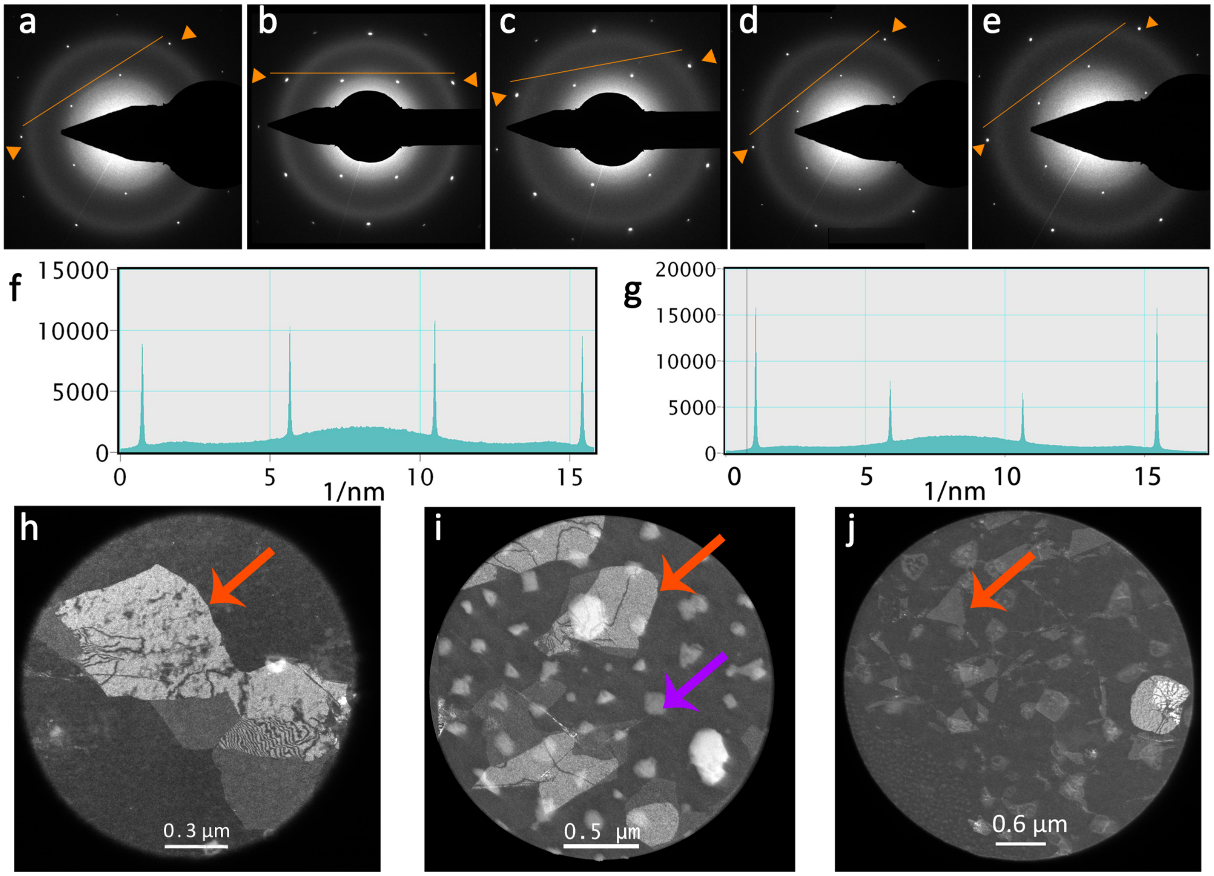

Figure 3.7 TEM selective area electron diffraction (SAED) patterns of single and bilayer graphene, diffraction intensity line profiles and low-resolution TEM (LRTEM) images. Normal incident diffraction pattern of (a) single layer graphene from methane grown at 1000 mTorr, (b) single layer graphene from ethane grown at 250 mTorr, (c and d) bilayer graphene from ethane at 500 mTorr and 1000 mTorr and (e) bilayer layer graphene from propane grown at 250 mTorr. Representative line profiles for (f) single layer and (g) bilayer graphene show the differences in diffraction intensities. LRTEM images of graphene grown with ethane at (h) 500 mTorr, (i) 1000 mTorr and with propane at (j) 250 mTorr, from many angles, show the actual size of each crystalline domain (red arrows) to be around 500 nm across, although SEM shows the actual coverage is much larger. The purple arrow indicates silicon residue from the etch process. Figure 3.7 reprinted with permission, copyright © 2012 WILEY-VCH Verlag GmbH & Co. KGaA, Weinheim

SAED analysis shows that films grown with higher pressures of ethane are AB stacked. The changes in relative peak intensities can be seen in the characteristic line profiles shown in Figure 3.7f (single layer graphene) and 5g (bilayer graphene). The peak intensities (outermost to innermost) of ~1:1 correspond to single layer graphene, while ~2:1 represents bilayer graphene. Methane in all cases produces single layer graphene and the 1000 mTorr case was chosen to show the high crystallinity and single layer diffraction for growths at the highest pressure. Graphene grown with ethane at 250 mTorr produces single layer graphene and the diffraction intensities reflect this, while higher pressures exhibit a ratio of 2:1, suggesting AB stacking in the areas of bilayer coverage. Films grown at 250 mTorr with propane produce diffraction patterns for bilayer graphene. Films produced at 500 and 1000 mTorr were too thick and were not analyzed with TEM due to transparency issues. For more information on the transmittance of each product, see the UV-Vis data in Figure 3.8.

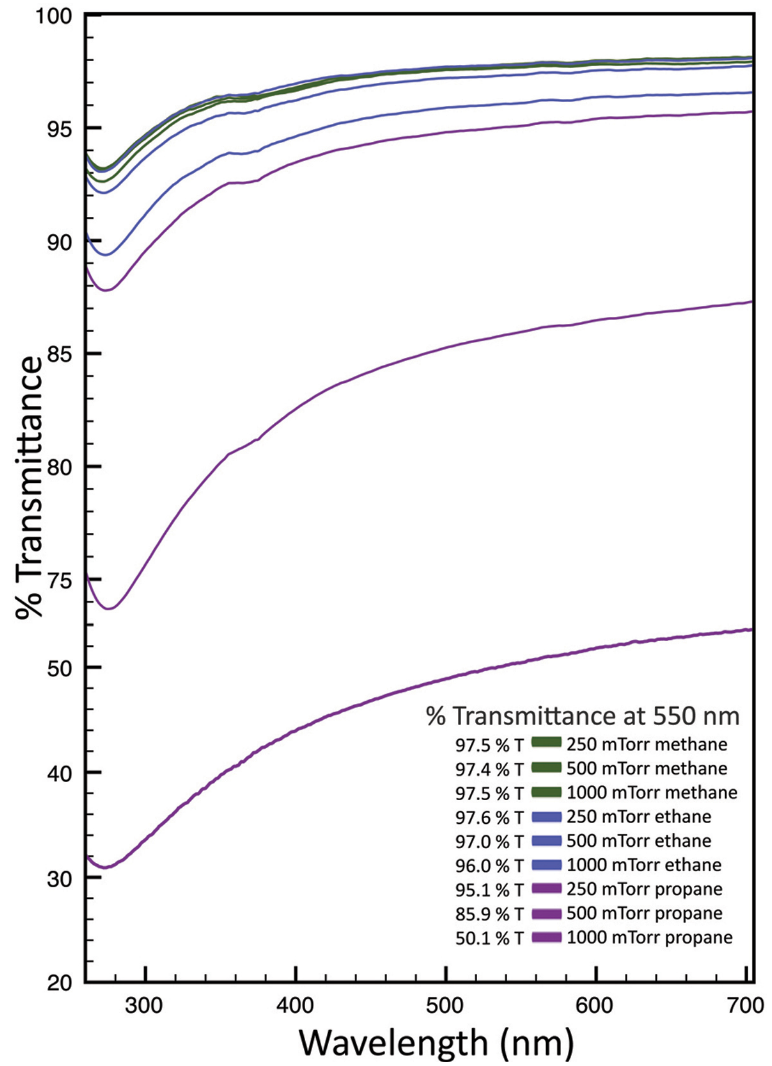

Figure 3.8 UV-Vis spectra from graphene transferred onto fused quartz discs. Methane at all pressures produces films with a transmittance (at 550 nm) of ~97%, indicative of single layer graphene. At varying pressures, ethane and propane will produce films with ranging transmittances, suggesting an increase in film thickness. Figure 3.8 reprinted with permission, copyright © 2012 WILEY-VCH Verlag GmbH & Co. KGaA, Weinheim

To characterize the domain size of the bilayer regions, we collected low-resolution TEM images. Huang et al., showed that CVD graphene is comprised of a patchwork of polycrystalline domains.[36] Images collected at various diffraction angles show the bilayer graphene grown with ethane at (5h) 500 mTorr, (5i) 1000 mTorr and with propane at (5j) 250 mTorr are composed of crystalline facet around 500 nm across, although SEM images show that the actual coverage is much larger.

3.3.3 Single Layer Graphene Growth with Methane on Copper: Scanning Tunneling Microscopy Analysis

Knowledge of material growth mechanisms on solid supports allows scientists to grow materials with highly desired properties. In heteroepitaxy, lattice matching between deposited materials and single crystal substrates dramatically affects the properties of grown materials. Small atomic lattice mismatches between substrates and the growth materials will create a significant amount of strain in single crystal films,[37] which can result in highly desired electronic properties or harmful defects.[38] In addition, when growing ionic films on metallic single crystals, the initial facet identity and mobility of the underlying substrate greatly influence the resulting surface structures. In these systems, a strong interfacial binding between surface charges on vicinal metal surfaces and ionic overlayers[39,40] drives massive surface restructuring and selective growth on specific metal facets.[41,42] These exemplary studies illustrate the significant role of substrate – overlayer interactions.

In collaboration with Professor Jim Gimzewski, we obtained Scanning Tunneling Microscope (STM) topographs of as-grown graphene produced by the thermal decomposition of methane on high purity polycrystalline copper disks. The STM allows us to observe the morphology of samples over several hundred square nanometers and to obtain atomic resolution of graphene's carbon lattice at specific surface features of interest in a single experiment. The pristine graphene lattice is shown to exist over the copper substrate despite underlying features that are generally thought to create defects in a growing overlayer. Defect-free graphene is observed over edges and vertices of the copper substrate where line and point defects are expected by conventional wisdom. Furthermore, the perfect lattice is observed over crystalline facets of a different symmetry than graphene and over highly stepped surfaces, both of which should inhibit efficient sheet extension.

3.3.3.a Sample Preparation and Imaging for the STM Study

Graphene was grown by Chemical Vapor Deposition (CVD) of carbon from a mixture of high purity methane (CH_4) and hydrogen (H_2) gases at 1000 °C in a tube furnace. Copper disks were loaded into a quartz tube and heated to 1000 °C over a period of ~40 minutes under a constant flow of H_2 gas. Samples were held at 1000 °C for 10 minutes before addition of methane. A flow rate of 100 sccm was used for CH_4 at a partial pressure of 6 Torr and a flow rate of 25 sccm was used for H_2 at a partial pressure of 1.5 Torr. After 20 minutes CH_4 flow was stopped. The sample was then cooled at a rate of ~20 °C/min under a 1.5 Torr atmosphere of H_2 gas. Copper disks were purchased from Alfa Aesar with the following characteristics; diameter = 9.0 mm, thickness = 0.8 mm, and percent purity = 99.9995%.

Samples were imaged under ambient conditions using a home-built scanning probe microscope housed in a custom-built enclosure. All images were acquired in constant current mode with tunneling set-points between 0.2 nA and 30 nA. Typical sample biases were acquired between -30 mV and -300 mV, referenced to the tip voltage. A Nanonis Universal SPM Controller was used for all data acquisition.

3.3.3.b Analysis

The polycrystallinity of the copper disc after graphene growth was established through Raman and XRD (Figure 3.9 a,b). Three low index facets of copper, (100), (110), and (111), are clearly oriented in the vertical direction, i.e. accessible to the imaging plane of the microscope. The only high index facet clearly observed in the diffraction pattern is the (311) plane. While the substrate polycrystallinity is expected, it is remarkable that monolayer graphene can grow over a substrate with multiple facets of different identities and whose surface atomic configurations vary dramatically. The (111) and (100) facets of the face centered cubic (FCC) copper metal have a “flat” hexagonal and cubic atomic arrangement at the surface of the bare metal with each atom having 6 and 4 in plane nearest neighbors, respectively. Conversely, the (110) and (311) facets have complex corrugated atomic arrangements at the surface with significant anisotropy. These fundamental geometric differences of the facets are expected to have distinct surface energy potentials, affecting the carbon atom extension differently.

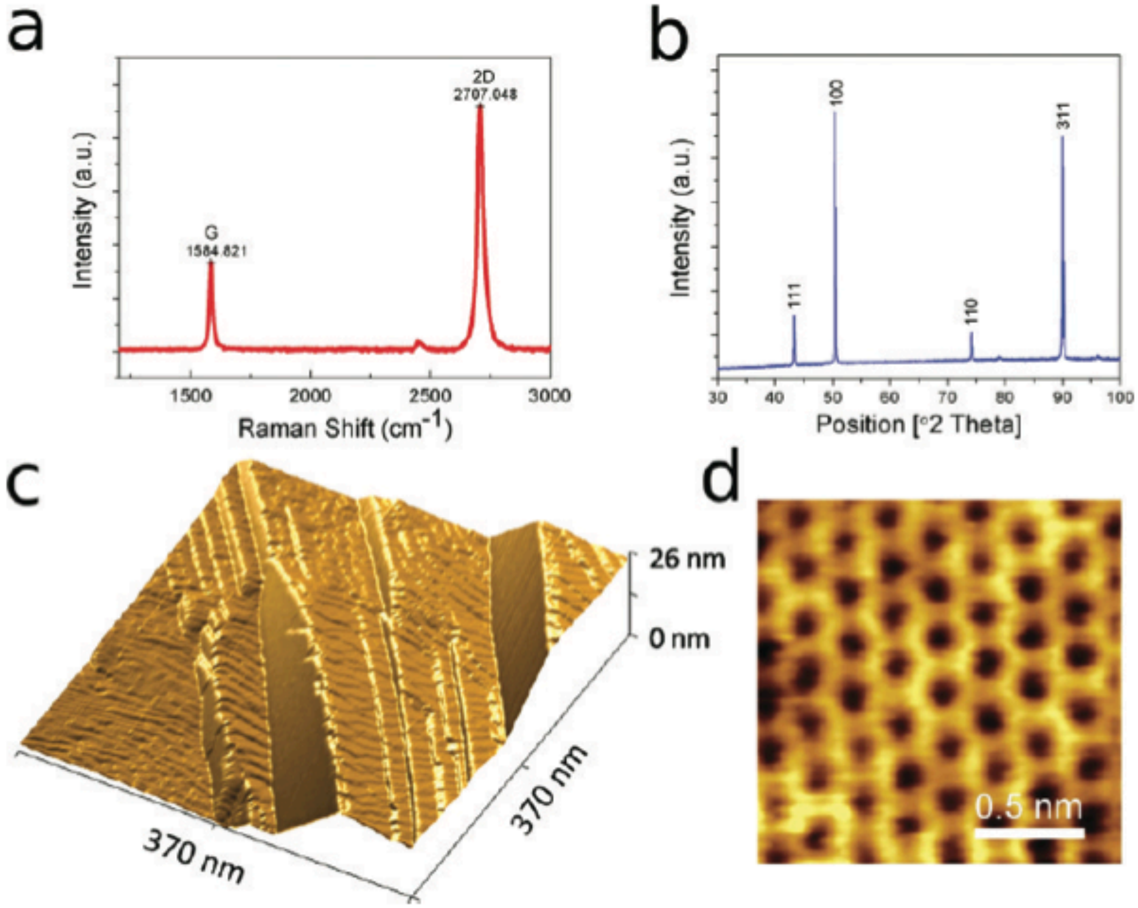

Figure 3.9 Characterization of as-grown graphene on polycrystalline copper. (a) Typical Raman spectrum of graphene on a polycrystalline copper substrate (after subtraction of copper luminescent back- ground). (b) Powder X-ray diffraction pattern of a copper disk after growth. (c) Typical large area STM topograph of as-grown graphene on a copper substrate: $I_{\text{tunneling}} = I_t =$ 0.9 nA, Vsample) V_{sample} =-75 mV. (c) Atomic resolution STM image of the pristine carbon honeycomb lattice: I_t = 5.0 nA, V_s = -75 mV. Figure 3.9 reprinted with permission, Copyright © 2011, American Chemical Society

Large area scans of graphene covered copper substrates taken at different locations show varied surface topography, but with common fundamental features (35.9 c). Some areas have large atomically flat regions that span hundreds of nanometers. Other areas have a highly corrugated surface, which is the result of small atomically flat planes oriented in different directions and with surface areas of a few tens of nanometers. Continuity of graphene was established through atomic resolution imaging (Figure 3.9d) at features of interest. An STM topograph of a corrugated area is shown in Figure 3.10a. The surface structure is characterized by different sets of parallel flat planes intersecting to form edges or vertices. An edge is defined as the intersection of two distinct planes and a vertex as the intersection of three or more planes. Atomic resolution images taken in certain flat areas (Figure 3.10b) show a perfect graphene lattice with a superimposed aperiodic modulation. The height variations proceed for a few nanometers with localized depressions of a half nanometer in width and up to 30 pm in depth. These modulations are attributed to defects within the copper substrate since freely suspended graphene shows larger intrinsic modulation amplitudes of 1 nm and longer coherence lengths of approximately 10 nm.[43] The copper may create these variations in the STM topograph where atomic vacancies exist near or at the interface between the metal and graphene overlayer (3). This is expected since copper mobility is extremely high at the growth temperature of 1000 °C and vacancies can become pinned between the graphene sheet and the copper during cooling.

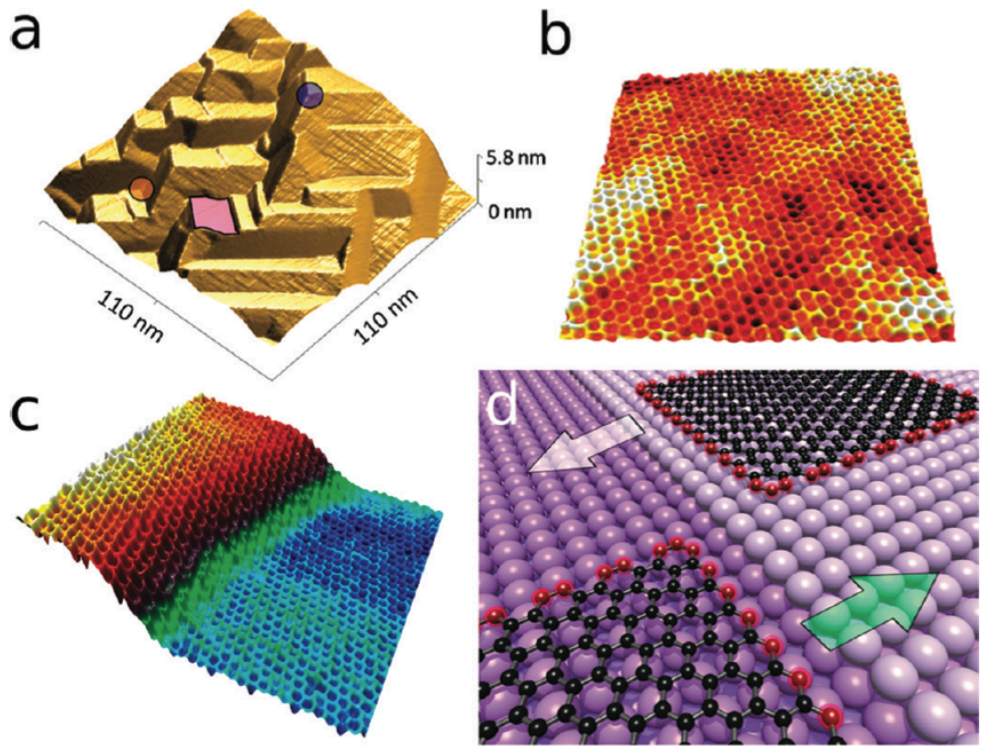

Figure 3.10 (a) STM topograph of a highly corrugated region of the sample. The magenta rectangle highlights an atomically flat plane, the blue circle highlights where three positive edges meet to form a positive vertex, and the orange circle highlights where three negative edges meet to form a negative vertex. (b) Atomic resolution STM topograph of a graphene sheet above an amorphous copper plane. (c) Atomic resolution STM topograph illustrating continuous growth over a copper monatomic step. (d) Schematic illustration of graphene growth “down” (white arrow) and “up” (green arrow) a monatomic Cu (100) step. Carbon atoms are represented by black spheres, foremost carbon atoms of the graphene sheet expected to interact with the monatomic step are highlighted with red spheres, light purple spheres represent copper atoms of the upper terrace, and darker purple spheres represent copper atoms of the lower terrace. Imaging parameters are as follows: (a) I_t = 0.5 nA, V_s = -500 mV, (b) I_t = 0.9 nA, V_s = 65 mV, and (c) I_t = 30 nA, V_s = -75 mV. Figure 3.10 reprinted with permission, Copyright © 2011, American Chemical Society

Within the flat regions, single and double atomic copper steps draped with a continuous layer of pristine graphene are observed. Figure 3.10c shows an atomic resolution STM topograph of a graphene sheet crossing over a monatomic copper step. While the continuity of graphene over monatomic steps of single crystal metal surfaces such as Ru (0001) and Ir (111) is known,[10,11] the mechanism of growth at these features remains an active area of theoretical and experimental research.[44,45] The growth mechanism associated with the extension of a carbon front (the foremost atoms of a sheet) "up" or "down" a monatomic metal step is thought to be fundamentally different (Figure 3.10d). Recent findings suggest that the carbon front terminates at metal step edges through bonding of the dangling carbon sigma bonds to metal step atoms, inhibiting upward growth.[10] However, a different study suggests that the carbon front may displace metal atoms beneath the sheet and onto nearby terraces in order to accomplish upward growth through an etching of the catalytic surface.[45] In the downward direction, growth seems uninhibited and may occur through a carbon dimer extension to a lower terrace.[44] Each of these formulations treats the graphene sheet as extending over or affecting a stagnant catalytic surface. In our experiments graphene continuity over step edges is always observed with no signs of termination at copper steps and may proceed via a more dynamic growth mechanism.

This study has established the continuity of the perfect graphene atomic structure over a multitude of surface features on the copper substrate, which are expected to inhibit efficient growth. Edges and vertices of the copper surface reveal perfect graphene growth where line or point defects are expected to occur through substrate induced sheet termination. With the possibility to grow graphene over regularly stepped surfaces, it may be possible to make use of periodic charge modulation as well as atomic lattice registry for post modification studies. Our results reveal that graphene growth on copper is a unique system where the underlying substrate morphology and atomic arrangement does not affect the atomic arrangement of the grown material. Finally, our results suggest that the growth of continuous macroscopic pristine graphene on copper is not limited by the substrate.

3.3.4 Proposed Growth Mechanism of Secondary Layers

The growth mechanism for secondary graphene layers is of great interest. Under these experimental parameters, we do not find secondary growth with methane, and literature reports indicate that it is considerably more difficult to grow bilayer graphene with methane. For example, multilayer graphene growth from methane has been observed in CVD under atmospheric pressure by using extended growth times or slow cooling rates.[23,28,29] Since longer growth times at relatively high temperatures are required for additional growth on a low carbon solubility catalyst, it seems likely that higher concentrations of carbon provide the means necessary for secondary growth. Additionally, bilayer graphene has been epitaxially grown on graphene coated copper foils by placing a fresh copper catalyst upstream, which produced "carbon fragments" that migrated to the target graphene.[29] The authors proposed the catalytic formation of alkyl radicals or other reactive species that react with graphene to grow a second layer. This is consistent with surface science experiments that showed a methyl radical source can be used to grow graphene on HOPG,[46] and is a possible mechanism for growth of additional graphene layers on copper.

Growing graphene with methane, ethane and propane provides experimental insight into the growth process. In addition to higher carbon content, ethane and propane also have significantly weaker C-H and C-C bond energies than methane. The C-H bond energies for methane are 105 kcal per mole versus 100 kcal per mole for ethane or propane (1° carbon) and the C-C bond energies for ethane and propane are only 90 and 88 kcal per mole, respectively.[47] Clearly ethane and propane, will dissociate more rapidly and result in a more facile formation of alkyl radicals, which are likely precursors to graphene.[48–50] In addition, studies involving the adsorption of alkanes on single crystal copper show the facile conversion of larger alkanes to alkenes by beta hydride elimination.[51,52] This is another possible mechanism by which ethane and propane are converted to alkene precursors on the surface of copper and form the initial layer.

Therefore the observation of additional graphene layers with ethane and propane likely results from alkyl radicals or alkenes that react with edges and defects in the previous layer, which favor reaction with incoming reactive carbon species.[29,46] A schematic of this process can be seen in Figure 3.11. Here it is illustrated that carbon radicals will quickly graphitize onto the copper surface, while dangling carbons on the first graphene layer will bond with incoming alkyl fragments and seed additional layers of graphene. In the most extreme cases, vertical growth will occur fairly rapidly, as seen in the case of propane growth at 1000 mTorr. A result of such a rapid crystallization is lower quality graphene; see the Raman spectra in Figure 3.5.

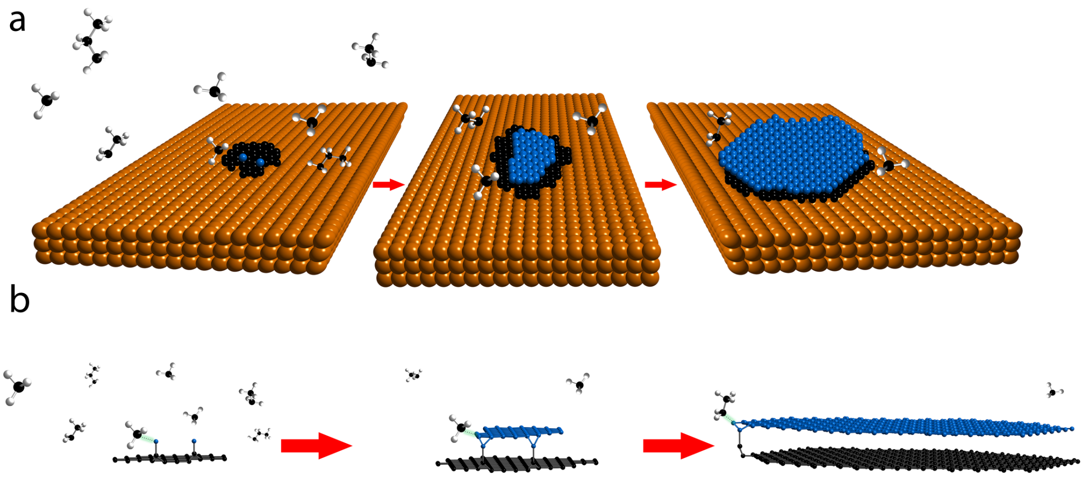

Figure 3.11 A schematic of bilayer graphene growth with ethane and/or propane feedstock gas. (a) Top view is shown with a space-filling model and (b) side view is shown with a ball-and-stick model. Copper atoms are shown as orange spheres, carbon in black (first layer) and in blue (second layer) and hydrogen in gray. When the copper catalyst is oversaturated with ethane molecules, secondary growth is observed. Since ethane has a lower decomposition pathway, higher concentrations of carbon radical will participate in secondary growth near the edge, where dangling bonds and defects are more prevalent. Figure 3.11 reprinted with permission, copyright © 2012 WILEY-VCH Verlag GmbH & Co. KGaA, Weinheim

Another strong factor in the growth of additional layers with these precursors is the number of carbon atoms available. Yao et al. show that few-layer graphene can be suppressed by reducing the flow of carbonaceous gases, such as methane and ethylene, while diluting them with hydrogen.[53] Propane delivers more carbon to the surface and accelerates surface reactions to produce secondary graphene such that only a combination of single - multilayer graphene is observed. A plot of the FWHM values for the Raman 2D peak vs. carbon content, Figure 3.12, illustrates that carbon concentration plays a vital role in the graphitization process and the resulting quality of the graphene. In this light, it may be possible to grow uniform single layer graphene with larger hydrocarbon gases, provided the feedstock gas is appropriately diluted with a reductive gas like hydrogen, and the growth time is modified.

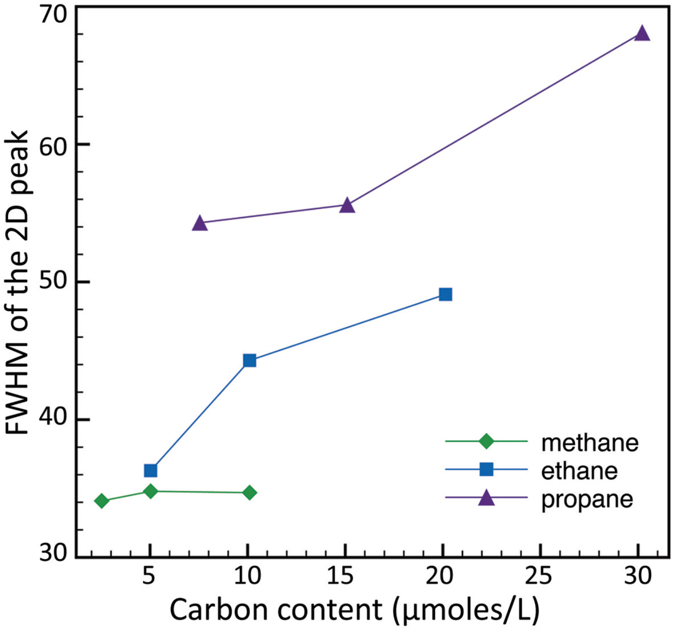

Figure 3.12 Plotting the resulting full width at half maximum (FWHM) of the Raman 2D peak versus the number of moles per liter of carbon show an overall trend suggesting that the number of graphene layers is likely proportional to the concentration of carbon in the system. Figure 3.12 reprinted with permission, copyright © 2012 WILEY-VCH Verlag GmbH & Co. KGaA, Weinheim

3.3.5 Selective Growth of Single or Bilayer Graphene: Experimental Details

Graphene is grown inside a 60 mm quartz tube and clam-shell furnace at 1000 ºC. Flow rates of 25 sccm for hydrogen and 100 sccm of methane, ethane and propane (Matheson research purity gases are used at pressures of 250, 500 and 1000 mTorr). 25 µm thick copper (99.999%

pure) foils (Alfa-Aesar) are loaded into the tube and annealed under the flow of hydrogen for 10 minutes at 1000 ºC to remove the oxide and to increase the copper grain sizes. Reactive hydrocarbon species are introduced and flow in conjunction with hydrogen for 20 minutes. Finally, the furnace is rapidly cooled.

PMMA (495 PMMA C9, Micro-Chem) was spin-coated and soft baked onto the resulting graphene-coated foil, at 180 ºC for 2 minutes, to protect a graphene layer and act as a support after the copper is etched away in an aqueous bath of $FeCl_3$, H_2O and concentrated HCl (3.5 g, 100 ml and 10 ml, respectively). A rigid support was used to transfer the graphene/PMMA into a bath of de-ionized water, where it was rinsed for 30 minutes to remove trace ion contaminates. Finally, the graphene is scooped up onto a target substrate and gently blown dry under nitrogen gas. Care was taken to avoid ripping the underlying graphene. A second PMMA layer was drop-cast onto the initial soft-baked PMMA layer, which dissolves the support and relaxes the strain in the underlying graphene film. Unlike previously described methods, the photo-resist was not cured and instead the sample was directly soaked in acetone to remove the polymer support. The graphene was finally annealed in an argon and hydrogen environment for 6 hour at 300 ºC to remove trace PMMA residues.

Optical micrographs of transferred graphene were obtained using a Zeiss Axioplan microscope at 50x and 100x magnification. A Titan 80-300 microscope was used to collect the electron diffraction patterns. TEM samples were prepared via transferring graphene onto silicon nitride substrates with a 3 nm silicon dioxide membrane layer, which was subsequently etched away in hydrofluoric acid to leave behind a suspended graphene sheet. Optical transmittance information was collected using a Shimadzu UV-3101PC, UV-Vis-NIR scanning spectrophotometer. Raman and 2D contour maps were collected on a Renishaw Raman spectrometer equipped with an automated stage. A 50x magnification lens obtains relatively high resolution with each pixel representing ~1 μm^2 area of the graphene.

3.4 Conclusions

In conclusion, we find that the single layer graphene growth rate is strongly correlated with the carbon concentration in the CVD reactor. Although each hydrocarbon gas decomposes into a graphene precursor on the copper surface, the larger molecules decompose and graphitize more rapidly than methane, consistent with hydrocarbon bond energies and known surface chemistry. To this end, the growth of additional graphene layers and its quality is directly related to a change in carbon concentrations. Since ethane and propane decompose via lower energy pathways, the reactive carbon species produced likely react with edges and defects to form additional layers of graphene. Finally, our experiments reveal that ethane is the preferred precursor for growing single and bilayer graphene, since changing the pressure from 250 to 1000 mTorr gives good selectivity without additional growth process and extended growth periods.

References

1. Wassei, J. K. & Kaner, R. B. Graphene, a promising transparent conductor. *Materials Today* **13**, 52–59 (2010).

2. Tung, V. C. *et al.* Low-Temperature Solution Processing of Graphene−Carbon Nanotube Hybrid Materials for High-Performance Transparent Conductors. *Nano Lett.* **9**, 1949–1955 (2009).

3. El-Kady, M. F., Strong, V., Dubin, S. & Kaner, R. B. Laser scribing of high-performance and flexible graphene-based electrochemical capacitors. *Science* **335**, 1326–30 (2012).

4. Tung, V. C., Allen, M. J., Yang, Y. & Kaner, R. B. High-throughput solution processing of large-scale graphene. *Nature Nanotechnology* **4**, 25–29 (2009).

5. Compton, O. C., Kim, S., Pierre, C., Torkelson, J. M. & Nguyen, S. T. Crumpled graphene nanosheets as highly effective barrier property enhancers. *Adv. Mater.* **22**, 4759–63 (2010).

6. Gómez-Navarro, C. *et al.* Atomic structure of reduced graphene oxide. *Nano Lett.* **10**, 1144–8 (2010).

7. Paredes, J. I., Villar-Rodil, S., Solís-Fernández, P., Martínez-Alonso, A. & Tascón, J. M. D. Atomic force and scanning tunneling microscopy imaging of graphene nanosheets derived from graphite oxide. *Langmuir : the ACS journal of surfaces and colloids* **25**, 5957–68 (2009).

8. Wassei, J. K. & Kaner, R. B. Oh, the Places You'll Go with Graphene. *Accounts of Chemical Research* **Article AS**, (2012).

9. Allen, M. J., Tung, V. C. & Kaner, R. B. Honeycomb Carbon: A Review of Graphene. *Chemical Reviews* **110**, 132–145 (2010).

10. Sutter, P. W., Flege, J.-I. & Sutter, E. a Epitaxial graphene on ruthenium. *Nature Materials* **7**, 406–11 (2008).

11. Coraux, J., N'Diaye, A. T., Busse, C. & Michely, T. Structural coherency of graphene on Ir(111). *Nano Lett.* **8**, 565–70 (2008).

12. Reina, A. *et al.* Large area, few-layer graphene films on arbitrary substrates by chemical vapor deposition. *Nano Lett.* **9**, 30–5 (2009).

13. Li, X. *et al.* Large-area synthesis of high-quality and uniform graphene films on copper foils. *Science* **324**, 1312–1314 (2009).

14. Li, X. *et al.* Transfer of Large-Area Graphene Films for High-Performance Transparent Conductive Electrodes. *Nano Lett.* **9**, 4359–4363 (2009).

15. T. Aizawa, R. Souda, S. O. and Y. I. Anomalous Bond of Monolayer Graphite on Transition-Metal Carbide Surfaces. *Phys. Rev. Lett.* **64**, 768–771 (1990).

16. Chen, S. *et al.* Millimeter-Size Single-Crystal Graphene by Suppressing Evaporative Loss of Cu During Low Pressure Chemical Vapor Deposition. *Advanced materials* **ASAP**, (2013).

17. Gao, L., Guest, J. R. & Guisinger, N. P. Epitaxial graphene on Cu(111). *Nano Lett.* **10**, 3512–6 (2010).

18. Tao, L. *et al.* Synthesis of high quality monolayer graphene at reduced temperature on hydrogen-enriched evaporated copper (111) films. *ACS nano* **6**, 2319–25 (2012).

19. Kim, K. S. *et al.* Large-scale pattern growth of graphene films for stretchable transparent electrodes. *Nature* **457**, 706–710 (2009).

20. Li, X. *et al.* Graphene films with large domain size by a two-step chemical vapor deposition process. *Nano Lett.* **10**, 4328–34 (2010).

21. Gao, L. *et al.* Efficient growth of high-quality graphene films on Cu foils by ambient pressure chemical vapor deposition. *Appl. Phys. Lett.* **97**, 183109 (2010).

22. Bhaviripudi, S., Jia, X., Dresselhaus, M. S. & Kong, J. Role of kinetic factors in chemical vapor deposition synthesis of uniform large area graphene using copper catalyst. *Nano Lett.* **10**, 4128–33 (2010).

23. Sun, Z. *et al.* Growth of graphene from solid carbon sources. *Nature* **468**, 549–552 (2010).

24. Srivastava, A. *et al.* Novel Liquid Precursor-Based Facile Synthesis of Large-Area Continuous, Single, and Few-Layer Graphene Films. *Chemistry of Materials* **22**, 3457–3461 (2010).

25. Michon, a. *et al.* Direct growth of few-layer graphene on 6H-SiC and 3C-SiC/Si via propane chemical vapor deposition. *Appl. Phys. Lett.* **97**, 171909 (2010).

26. Guermoune, A. *et al.* Chemical vapor deposition synthesis of graphene on copper with methanol, ethanol, and propanol precursors. *Carbon* **49**, 4204–4210 (2011).

27. Nandamuri, G., Roumimov, S. & Solanki, R. Chemical vapor deposition of graphene films. *Nanotechnology* **21**, 145604 (2010).

28. Lee, S., Lee, K. & Zhong, Z. Wafer Scale Homogeneous Bilayer Graphene Films by Chemical Vapor Deposition. *Nano Lett.* **10**, 4702–4707 (2010).

29. Yan, K., Peng, H., Zhou, Y., Li, H. & Liu, Z. Formation of Bilayer Bernal Graphene: Layer-by-Layer Epitaxy via Chemical Vapor Deposition. *Nano Lett.* **11**, 1106–1110 (2011).

30. Luo, Z. *et al.* Large-Scale Synthesis of Bi-layer Graphene in Strongly Coupled Stacking Order. *Advanced Functional Materials* **21**, 911–917 (2011).

31. Roddaro, S., Pingue, P., Piazza, V., Pellegrini, V. & Beltram, F. The optical visibility of graphene: interference colors of ultrathin graphite on SiO(2). *Nano Lett.* **7**, 2707–10 (2007).

32. Lenski, D. & Fuhrer, M. Raman and optical characterization of multilayer turbostratic graphene grown via chemical vapor deposition. *Journal of Applied Physics* **110**, 013720 (2011).

33. Ferrari, A. C. *et al.* Raman spectrum of graphene and graphene layers. *Phys. Rev. Lett.* **97**, 187401 (2006).

34. Malard, L. M. *et al.* Probing the electronic structure of bilayer graphene by Raman scattering. *Physical Review B* **76**, 201401 (2007).

35. Graf, D. *et al.* Spatially resolved Raman spectroscopy of single- and few-layer graphene. *Nano Lett.* **7**, 238–42 (2007).

36. Huang, P. Y. *et al.* Grains and grain boundaries in single-layer graphene atomic patchwork quilts. *Nature* **469**, 389–392 (2011).

37. Roberts, M. M. *et al.* Elastically relaxed free-standing strained-silicon nanomembranes. *Nature Materials* **5**, 388–93 (2006).

38. Chen, Y. & Washburn, J. Structural Transition in Large-Lattice-Mismatch Heteroepitaxy. *Phys. Rev. Lett.* **77**, 4046–4049 (1996).

39. Repp, J., Fölsch, S., Meyer, G. & Rieder, K.-H. Ionic Films on Vicinal Metal Surfaces: Enhanced Binding due to Charge Modulation. *Phys. Rev. Lett.* **86**, 252–255 (2001).

40. Olsson, F. . & Persson, M. A density functional study of adsorption of sodium-chloride overlayers on a stepped and a flat copper surface. *Surface Science* **540**, 172–184 (2003).

41. Folsch, S. *et al.* Self-organized patterning of an insulator-on-metal system by surface faceting and selective growth: NaCl/Cu(211). *Phys. Rev. Lett.* **84**, 123–6 (2000).

42. Fölsch, S., Riemann, A., Repp, J., Meyer, G. & Rieder, K. From atomic kinks to mesoscopic surface patterns: Ionic layers on vicinal metal surfaces. *Physical Review B* **66**, 161409 (2002).

43. Meyer, J. C. *et al.* The structure of suspended graphene sheets. *Nature* **446**, 60–3 (2007).

44. Chen, H., Zhu, W. & Zhang, Z. Contrasting Behavior of Carbon Nucleation in the Initial Stages of Graphene Epitaxial Growth on Stepped Metal Surfaces. *Phys. Rev. Lett.* **104**, 186101 (2010).

45. Starodub, E. *et al.* Graphene growth by metal etching on Ru(0001). *Physical Review B* **80**, 235422 (2009).

46. Wellmann, R., Böttcher, A., Kappes, M., Kohl, U. & Niehus, H. Growth of graphene layers on HOPG via exposure to methyl radicals. *Surface Science* **542**, 81–93 (2003).

47. Luo, Y. *et al.* Handbook of Bond Dissociation Energies in Organic Compounds. *CRC Handbook* 65–80 (2009).

48. Blanksby, S. J. & Ellison, G. B. Bond dissociation energies of organic molecules. *Accounts of Chemical Research* **36**, 255–63 (2003).

49. Matta, C. F., Castillo, N. & Boyd, R. J. Atomic contributions to bond dissociation energies in aliphatic hydrocarbons. *The Journal of chemical physics* **125**, 204103 (2006).

50. Zipse, H. Radical Stability—A Theoretical Perspective. *Radicals in Synthesis I* 163–189 (2006).doi:10.1007/128

51. Jenks, C., Bent, B. & Zaera, F. The chemistry of alkyl iodides on copper surfaces. 2. Influence of surface structure on reactivity. *The Journal of Physical Chemistry B* 3017–3027 (2000).

52. Teplyakov, A. V & Bent, B. E. Β-Hydride Elimination from Alkyl and Cycloalkyl Groups on a Cu (100) Surface: Ring Strain and Planarity of the Transition State. *J. Am. Chem. Soc* **117**, 10076–10087 (1995).

53. Yao, Y. *et al.* Controlled Growth of Multilayer, Few-Layer, and Single-Layer Graphene on Metal Substrates. *The Journal of Physical Chemistry C* **115**, 5232–5238 (2011).

Chapter 4: Graphene Electronic and Bio-Electronic Applications

Initially, graphene was lauded as a replacement for silicon in electronics, potentially enabling scientists to engineer smaller and faster circuits. While electronic applications may be important, many other applications have emerged and it seems likely that graphene will provide a cornerstone for some new and exciting technologies as described here briefly.

4.1 Graphene Flash Memory

Graphene has emerged as a fascinating platform because its planar atomic structure and high symmetry lead to a variety of superlative electronic and physical properties. Recent achievements in graphene research have fallen mainly into two categories. First, applications have been developed that rely on the intrinsic in-plane properties of graphene, such as new types of circuitry, robust films and photonic absorption. Secondly, applications requiring conductive thin films have benefited from graphene as a single atomic layer. Growing graphene via Chemical Vapor Deposition provides scientists access to large area and highly crystalline material. With this in mind, in collaboration with Prof. Kang Wang's group we explored using graphene for information storage, which we named, graphene flash memory (GFM).[1]

This form of nonvolatile memory utilizes graphene's high surface area, high work function and low dimensionality.[1] Our devices demonstrate that GFM has a 6 V memory window and using a program/erase voltage of ±7 V, long retention time, and low cell-to-cell interference. The figure of merit from our work can be seen in Figure 4.1. Our results indicate that the device performance of GFM is promising for achieving flash memory at a fraction of the current operating voltage.

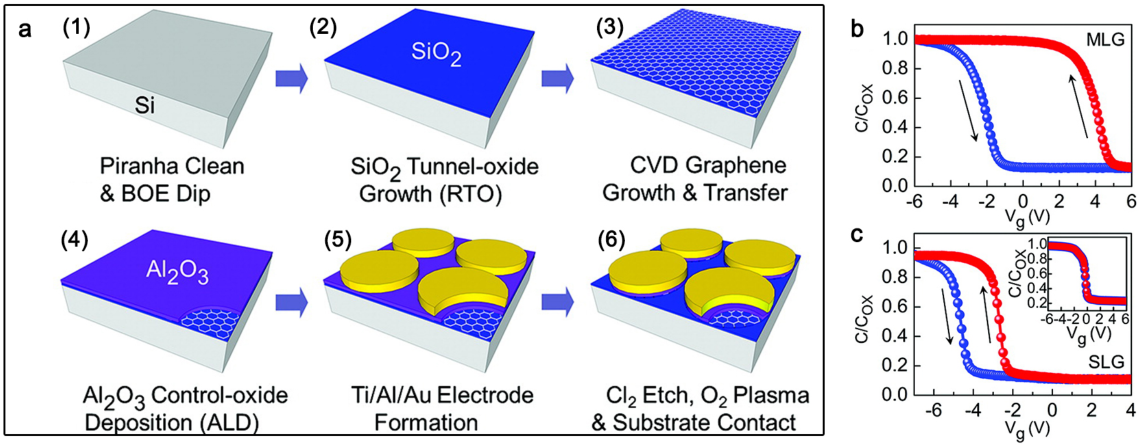

Figure 4.1 Graphene flash memory. (a) Schematic of graphene flash memory fabrication and the figure of merit, the memory window showing that (b) multilayer GFM has a 6 V memory window and (c) single layer GFM has a 2 V memory window using a program/erase voltage of ±7 V.

Graphene has the potential to exceed the performance of current flash memory technology by utilizing the exceptional intrinsic properties of graphene, such as high density of states, high work function, and low dimensionality when compared to the conventional FG and CT materials. Recently, it was shown that incorporation of an insulating form of graphene, known as graphene oxide, acts as an effective charge storing layer in CT devices.[2] In its natural semimetallic form, graphene can act as the floating gate in FG devices. Finally, the experiments demonstrate the benefits of graphene as a platform for flash memory.[1] The high density of states, high work function, and low dimensionality positively influence device performance, leading to a wide window of operation at low voltages, long retention time, and low cell-to-cell interference. The simulations pertaining to cell-to-cell interference further suggest that graphene may be instrumental in the next round of miniaturization of flash memory.

4.2 Graphene Electrodes for Nerve Cell Growth

One of the key challenges in medical bionics is to interface with, to stimulate, and regenerate the human neural system. Enhancing the communication between the electrode and the neural system will have immediate impact on existing medical bionics devices such as the cochlear implant, an artificial retina implant, vagus nerve stimulators (for controlling of epilepsy and pain management) and deep brain stimulators for the control of Parkinson's disease. More effective communication would also enable the development of other applications such as nerve regeneration or effective neural connections to wearable prosthetics. Here, we describe a process to modify non-conducting materials with graphene to create an electrode capable of electrical communication with cells without changing the surface or mechanical properties of the underlying materials. Each of the aforementioned implants require the development of novel structures and configurations that induce the formation of an effective electrode – cellular interface.[3] This also means that the electrode structure must be cytocompatible and have controllable mechanical properties.

Typically, attaining such materials is a significant challenge since conductive materials are often mechanically rigid. The difference between the modulus of the conductive material and the surrounding tissue can be problematic, both in terms of communication between the conductor and nerve cells, and the tissue response in the vicinity of the implanted material. Recent interest in developing a soft, conductive material has led to heightened research into the use of organic conductors.[4]

One material with the potential to provide the desired characteristics of bio-electrode structures, as discussed above, is graphene.[4] Chemical Vapor Deposition can produce both single and bilayers of sp^2 hybridized graphene on metal catalysts. One crucial advantage of this growth method is the ability to grow and transfer large-area graphene onto a range of different substrates, followed by metal etching.[5–13] Traditionally, this transfer has been achieved through the spin-casting of thin layers of poly(methyl methacrylate) (PMMA) onto copper foil followed by etching of the copper by concentrated HCl and $FeCl_3$. The etching process produces graphene on PMMA, which is then cleaned and deposited onto a range of substrates followed by polymer dissolution. We present an abridged process in which graphene is simply transferred onto a range of PLA and PLGA bio-polymers, the target substrate, via solution casting or melt processing methods, followed by the removal of copper.

CVD graphene is mechanically robust, opening unique avenues to design conductive, flexible and biocompatible electrodes with a controllable modulus. It has been found that multiple layers of graphene will have an effect on the electronic properties of graphene, allowing for the formation of tunable band-gaps in bilayer graphene over small areas.[14–16] In all cases regarding synthesis, there has been a significant focus on the lattice overlay structure (AB vs. ABC), which is poorly controlled over large areas. The interest in bilayer graphene for this application, however, is not the tunable band gap, but rather the conductivity, chemical stability and mechanical support, which other materials do not provide. Specifically the utilization of bilayer graphene allows for an increased conductive pathway over rough, flexible substrates. It is hypothesized that bilayer graphene would conform tightly to the polymer layer while remaining electrically conductive, as a continuous layer over large vertical height step changes. As such, the localized stacking parameters of the bilayer graphene were not studied within this body of work.

Polylactic acid (PLA) and polylactic-co-glycolic acid (PLGA) are biocompatible and biodegradable synthetic polymers made from polymerization of lactic acid and glycolic acid. PLGA materials, in particular, have found many applications in several biomedical devices, starting from their use as bio-resorbable sutures in the 1970s and moving towards more nanotechnological applications in recent years.[17] Increasing the proportion of glycolide relative to lactide in the polymerization leads to softer films that have higher rates of degradation.[18] PLA and PLGA films were chosen for this study due to the ability to tailor the mechanical properties within the same family, and for the known biocompatibility of the materials. It is known that varying the softness of the underlying materials changes the way that nerve cells grow and differentiate in culture,[19] and the use of PLGA materials with different mechanical properties is expected to change the way that PC-12 cells grow. Recently, it has been shown that CVD graphene sheets can mimic the surface chemistry of the underlying substrate.[20] This principle, when extended to mechanical properties, could allow for unprecedented control over the electronic and mechanical environment cells experience during growth and differentiation.

Here we explore the transfer of CVD-grown single and bilayer graphene onto glass coverslips and a range PLA and PLGA blends, with the final produced structure illustrated in Figure 4.2. We demonstrate that the rate of nerve cell growth is based on the underlying mechanical film properties, and not graphene modification, and then provide the first literature report of electrical stimulation of cells on graphene to enhance the differentiation into a neural phenotype. These results show that the process of transferring graphene onto non-conducting biocompatible polymers can be used to create an electrode that is sufficiently conductive for electrical communication with cells while retaining the mechanical and surface properties of the base polymer.

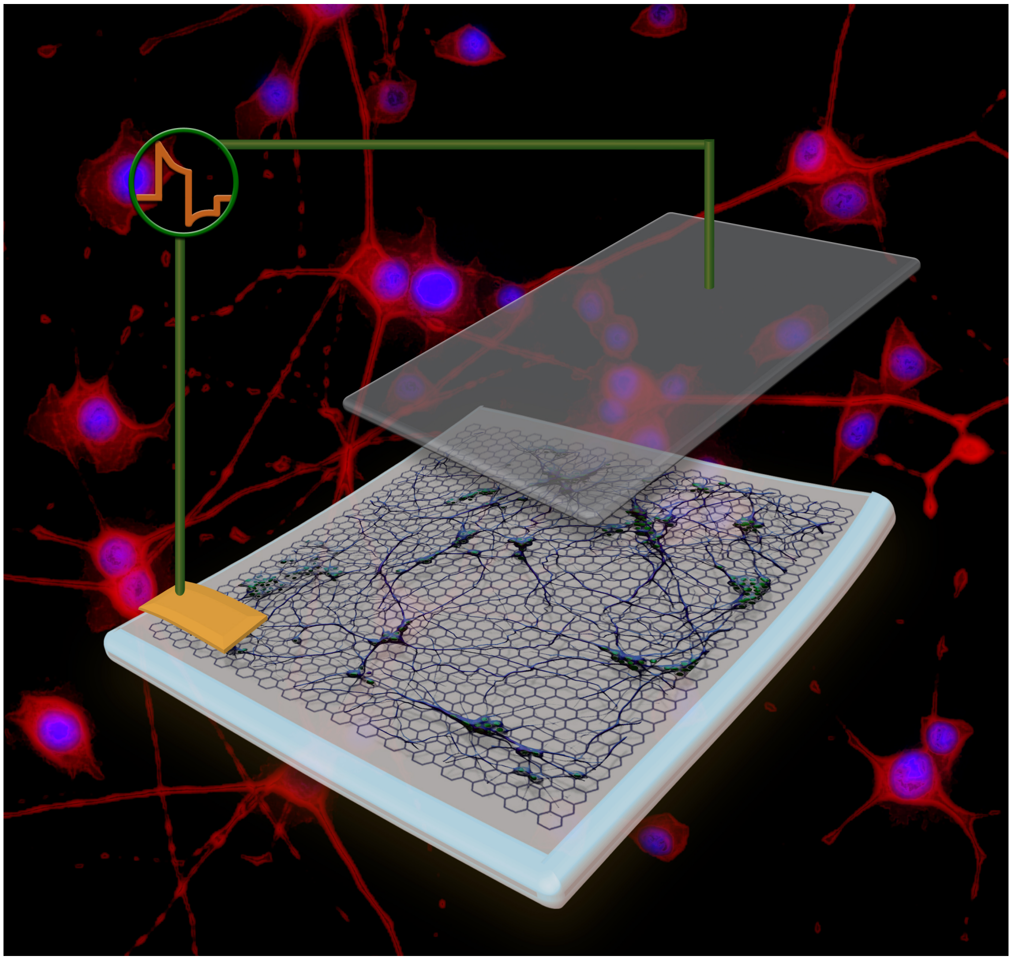

Figure 4.2 Schematic of neural cells growing on the GBP composite produced by modification of non-conducting biocompatible polymers with graphene. Here, a gold electrode connects to the graphene coated biopolymer and acts as a working electrode, while a platinum mesh (suspended above) is used as the counter-electrode. The electrode is shown in the final 2-electrode cell configuration, used for electrical stimulation of neural cell differentiation.

We demonstrate the utility of large-area graphene as a biocompatible electrode to stimulate PC-12 nerve cell growth. These experiments are two-fold: first, graphene transferred onto glass slides was analyzed and then used to stimulate cell growth; second, graphene was also transferred onto biopolymer supports, such as polylactic acid (PLA), polylactic-co-glycolic acid

(PLGA) copolymers, which provide a unique electrode structure retaining the mechanical and surface properties of the underlying materials with a conductive graphene conduit to enable electrical communication with excitable cells. The growth and compatibility of PC-12 cells on these graphene-biopolymer (GPB) electrodes was influenced by the underlying polymer. Differentiation of these cells into neural phenotypes was enhanced using electrical stimulation through the graphene conductive layer, confirming the ability to communicate with cells grown on the surface. The process described herein demonstrates that non-conducting, flexible biopolymer surfaces of desirable mechanical properties can be easily coated with graphene to create an electrode structure with electrical properties suitable to effectively stimulate cells for a wide-range of biomedical applications.

4.2.1 Nerve Cell Interactions with Graphene on Glass Coverslips

Initial studies involved the study of graphene's topology, electrochemical properties and the cytotoxicity. We set out to first verify the biocompatibility with the cells of interest, PC12 nerve cells. We explored two routes, graphene, which transferred onto glass cover slips and graphene as grown on copper into culture wells. We found that after 3 days of incubation, the cells transferred onto glass survived, while those transferred onto graphene on copper did not. We attribute this to cell culturing conditions, which caused the copper foils to oxidize and eventually kill the cells. Once this preliminary experiment was concluded, we decided to further study the nerve cell interactions with graphene and to determine if stimulated growth can be possible.

We designed a set of experiments to fully characterize the graphene and to determine the materials properties specifically for this application. First, we obtained cyclic voltammetry (CV) curves to determine charge capacity and also the redox potential in known electrolytes. Second, we studied the surface topology of graphene to determine the continuity and surface conductivity using atomic force microscopy (AFM), see Figure 4.3. Third, we designed culture cells in which nerve cells can be incubated and the current can be applied across the graphene for stimulated growth. The design of the experiment can be seen in Figure 4.4. In all instances, the experiments were carried out in triplicates for more conclusive evidence. Stimulated growth and incubation of the cells was performed over 4 days before growth was terminated and cell counting commenced.

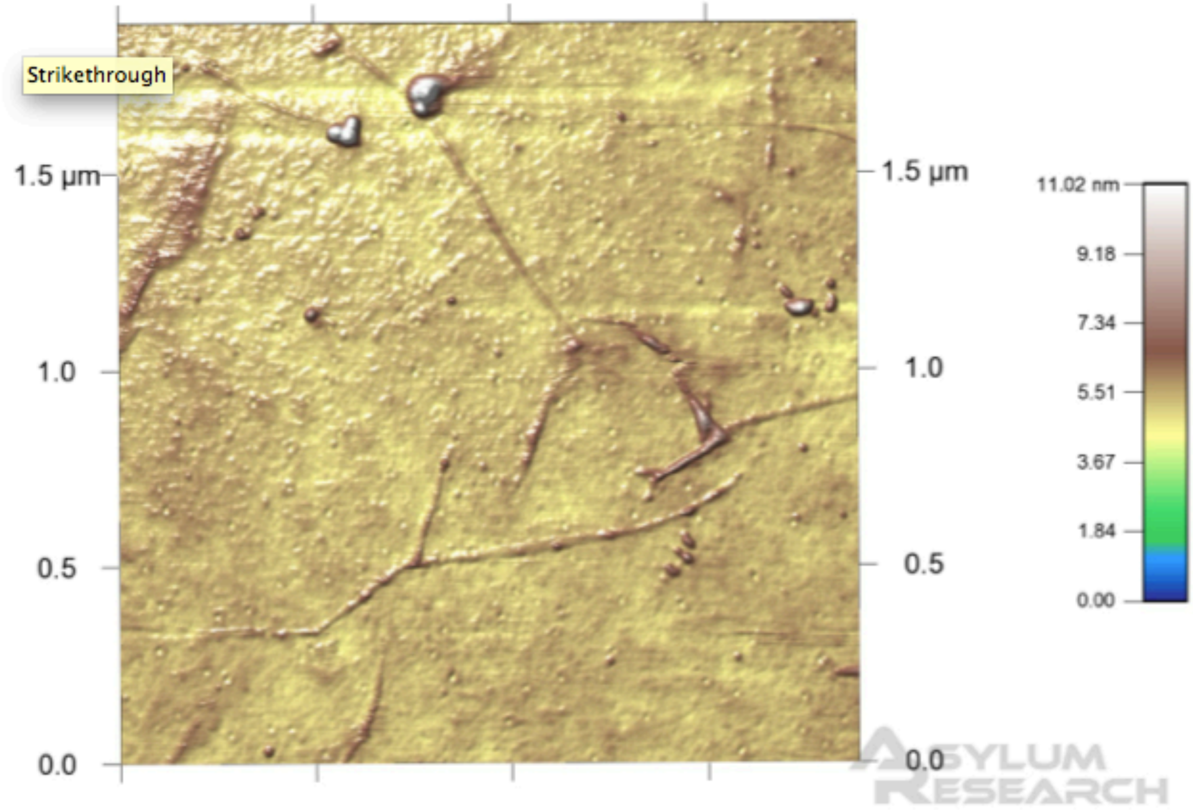

Figure 4.3 Atomic force micrograph (AFM) of graphene on a cover-slip. AFM scans reveal that the topology of the transferred graphene on rigid glass cover-slips results in micron sized wrinkles in the film. The small speck near the top is a result of polymer contamination from the PMMA transfer process.

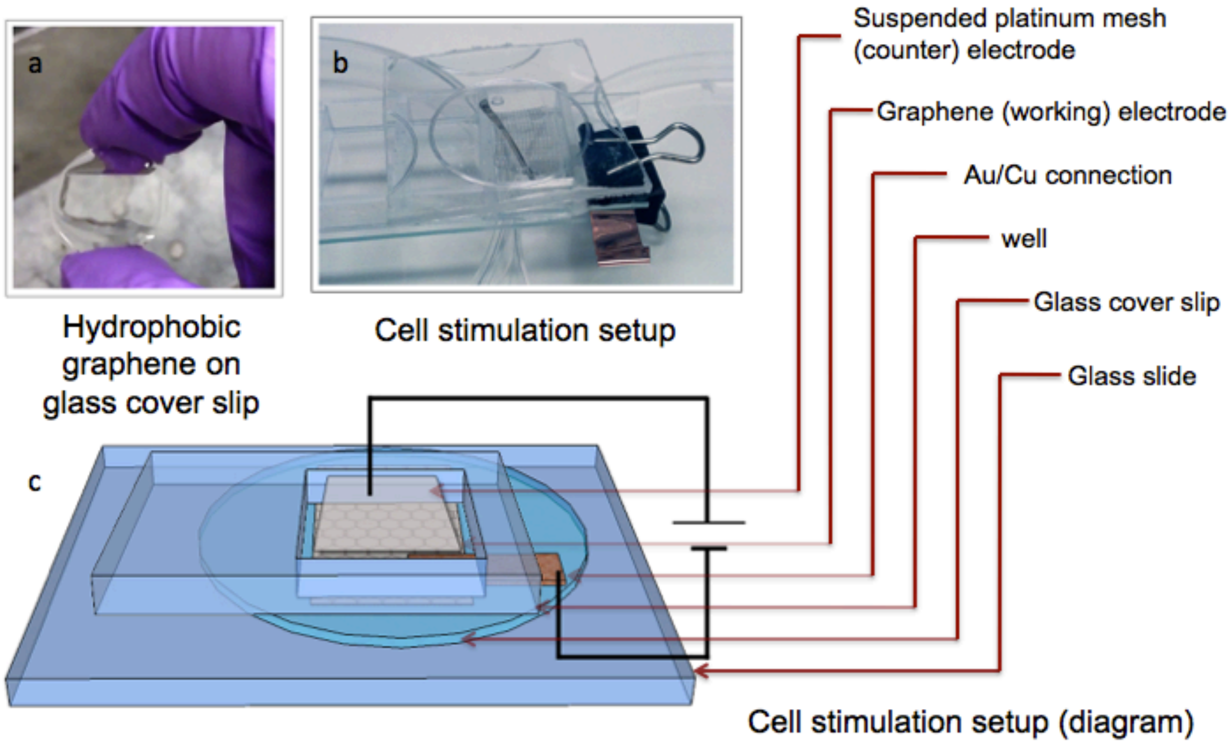

Figure 4.4 Cell stimulation setup using (a) graphene transferred onto glass cover-slips, which are then placed into a (b) cell well. The set up can be seen in (c) a schematic diagram.

Exciting results revealed that the PC12 nerve cells grow on graphene without the use of adhesion promoter proteins and preferentially to bare glass slides (Figure 4.5). Cellular growth was measured using optical micrographs and ImageJ software to count the length and number of dendrites on the graphene. The results from stimulated growth were not as favorable, as most cells went into apoptosis. After careful consideration, we determined that this must be due to the relatively low charge capacity of graphene, in relation to conducting polymers. In this respect, we attribute the apoptosis to a high charge injection rate from graphene into the cells and believe that stimulated growth is possible. To better accommodate the cells in a soft environment, it seemed important to repeat these experiments using soft biopolymer substrates.

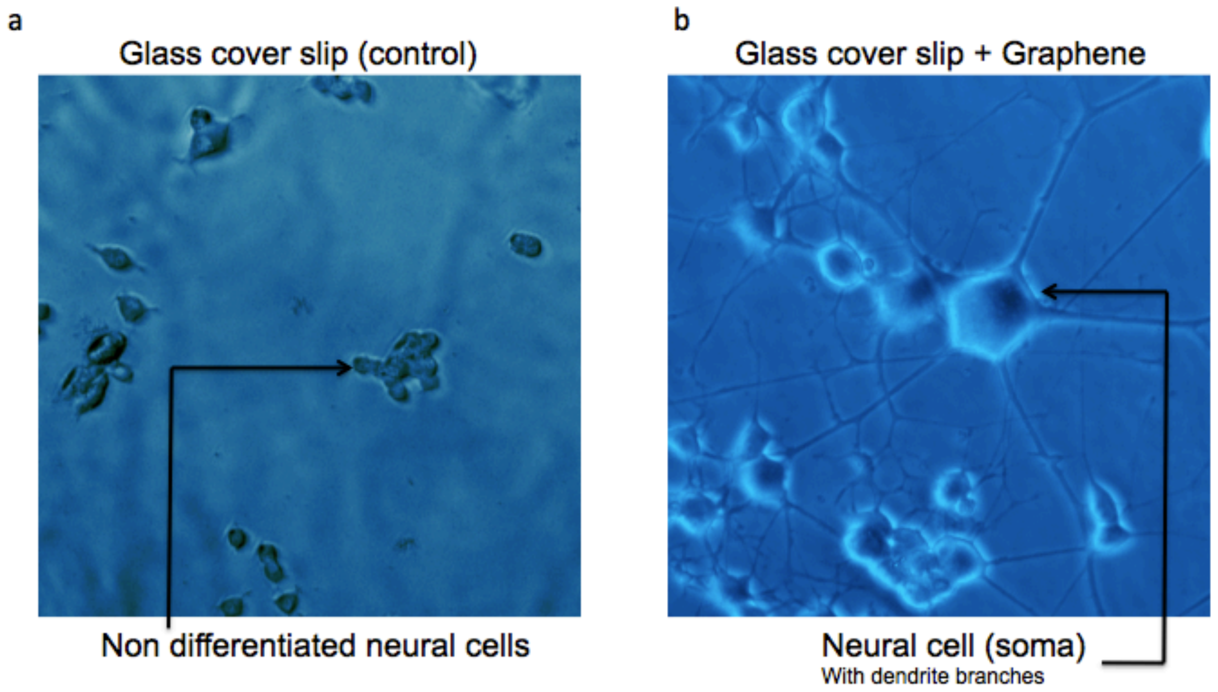

Figure 4.5 Optical micrographs of PC-12 nerve cells after incubation (a) without and (b) with graphene.

4.2.2 Graphene-Biopolymer Structures and Nerve Cell Stimulation

Variations in the CVD growth conditions, such as partial pressure, flow rate and temperature afford the growth of either 1 or 2 layers of graphene on the copper substrate. Raman spectroscopy clearly identified these regions as single, multi- or few-layered graphene based on the 2D:G ratio and the FWHM of the 2D peak (Figure 4.6a). The graphene was then transferred onto a range of PLA and PLGA biocompatible polymer films (PLA, 75:25 PLGA, and 50:50 PLGA) through drop-casting the pre-cured polymer over areas up to 9 cm^2, forming graphene-biopolymer composites (GBP). After a brief curing process, the copper was etched away.

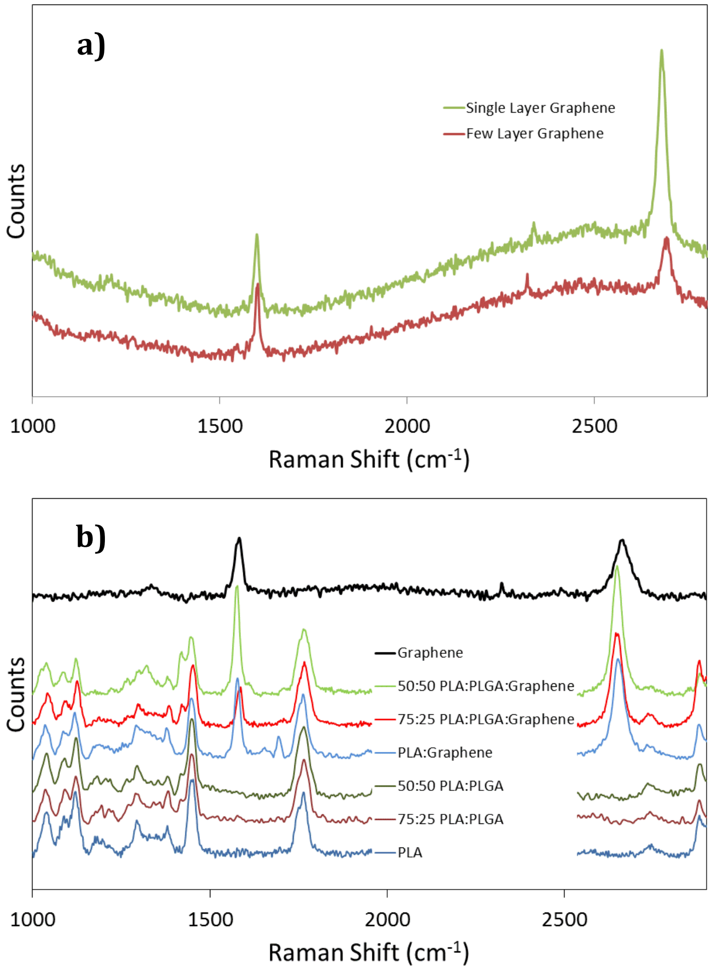

Figure 4.6 Raman spectra and analysis of graphene used for the cell stimulation studies. a) Raman spectra of graphene on copper sheets, showing the difference in 2D band excitation between regions of single layer or few-layer graphene; and b) Raman spectra of assorted biopolymer composites with and without transferred graphene.

Raman spectral analysis of these GBPs shows both the graphitic G band at ~1580 cm^{-1} and the 2D band at ~2650 cm^{-1}, confirming the successful transfer of graphene (Figure 4.6). Due to signal damping from the soft polymer layer, quantitative analysis of the number of transferred layers is not possible; however, qualitatively (from the Raman spectra of graphene on copper) it can be stated that predominantly bilayer graphene was transferred onto the polymer structures. Crucial to the confirmation of the successful transfer of bilayer graphene onto the polymers is the analysis of the full width at half maximum (FWHM) of the 2D peak subsequent to this transfer.[21–25] To this end, high resolution Raman spectroscopy with an 1800 line/mm grating was utilized, with analysis of the as grown graphene on copper shows four distinct peaks at 2636 cm^{-1}, 2643 cm^{-1}, 2671 cm^{-1} and 2687 cm^{-1}, respectively. Transfer of the graphene onto the biopolymers results in a red shift of these peaks to 2641 cm^{-1}, 2648 cm^{-1}, 2664 cm^{-1} and 2679 cm^{-1}, respectively, with a corresponding decrease in relative intensity of the peaks at higher wavenumbers. This decrease in peak intensity arises from the interaction of graphene with the polymer substrate causing a change in the way the layers vibrate in respect to each other. Such a change in vibrational mode is analogous to the restriction of the radial breathing modes of single-walled carbon nanotubes in the presence of polymers or surfactants.[25,26] Surface wettability is of paramount importance for cytocompatibility. To understand the changes in the surface energies of the GBP structures, room-temperature goniometric measurements were performed using 200 μL droplets of distilled water. PLA films were measured to have a contact angle of 68±12° and the addition of graphene caused the contact angle to increase to 75±7°, indicating only a slight change in the wettability of the material (Figure 4.7). This change arises either due to the addition of a hydrophobic surface to the material, or an increased nano-scale roughness after coating. We hypothesize that as the graphene mimics the surface morphology of the underlying substrate, the roughness of PLA (after etching) and PLA GBP would be very similar, thus the slight change in hydrophillicity of the material can be attributed to a minimal change in the surface energy. Interestingly, there was a dramatic increase in hydrophillicity when PLGA was utilized, with the resultant contact angle approaching 0 and being immeasurable for both etched

PLGA and PLGA GBPs. This decrease is attributed to the effect of the change in surface roughness from the etching process.

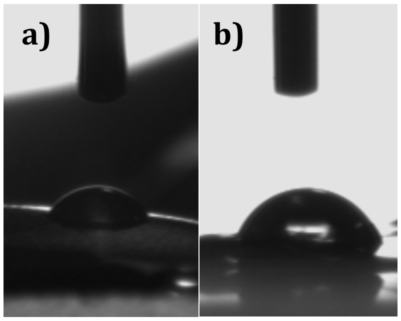

Figure 4.7 Contact angle measurements of 200 μL of distilled water of a) PLA and b) PLA GBP.

The focus of this section is to demonstrate the stimulation of nerve cells on graphene sheets. To determine the conductivity of the material, sheet resistance values were measured using both a high impedance multimeter and a linear 4-point probe system. The resistance of these films was observed to vary greatly dependent on the contact area of the dried films with the graphene substrate. Typical values of resistance were 10 kΩ over a linear 3 cm distance, measured using a high impedance multimeter. Utilizing a linear 4-point probe geometry, the sheet resistance of the GBP films was determined to be approximately 1 kΩ/□ (Table 4.1) for all of the examined samples. There was a large natural variation within all of the examined samples, which is attributed to poor contact between the probes and the sample. This poor contact is a function of both the soft polymer in relation to the significantly stiffer probe and the approximately 1 nm thickness of the conductive layer. The relatively low resistivity performance of the GBP composites demonstrates the utility of graphene as a viable electrode material, which is shown later for the electrical stimulation of nerve cells.

A 1 cm^2 (geometric surface area) GBP structure was prepared from a polymer composition of 50:50 PLGA, and placed into a bath of 1M $NaNO_3$. Using cyclic voltammetry (scan rate of 0.05 V/s), specific capacitance values were determined to be of the order of 7 $\mu F/cm^2$ (Figure 4.8). This value is near the lower boundary of charge for a Helmholtz double layer capacitance with a 1 cm^2 electro-active surface area, expected to be between 5 and 20 $\mu F/cm^2$.[27–29] We attribute the measured capacitance value to three possible reasons. First, the range of expected capacitance values were measured using bulk carbon materials with resistances of 10 to 100 Ω/□, while these GPB structures use graphene with a sheet resistance of ~1000 Ω/□. Second, there is a significant signal loss when making contact to these GBP structures due to contact resistance. Third, the capacitive response can be affected by the step-height changes in the polymer that can induce stress in the graphene and increase resistance in those areas.

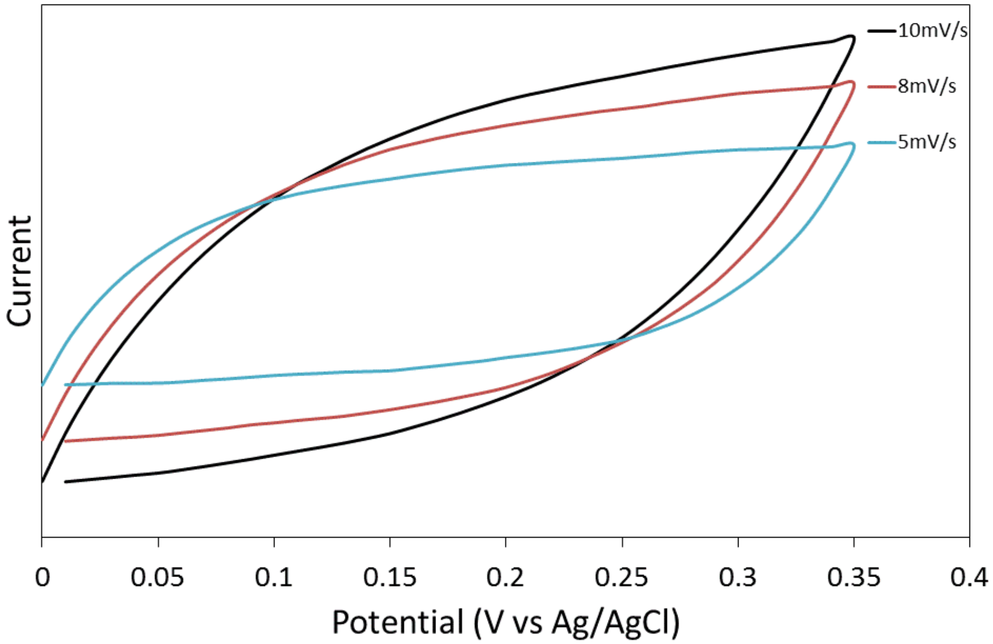

Figure 4.8 Cyclic voltammogram of a 1 cm^2 of 50:50 GBP in 1 M $NaNO_3$ showing a largely capacitive response at slow scan rates of 5 mV/s; higher scan rates of 10 mV/s begin to elicit a more resistive peak shape.

Atomic force microscopy (AFM) measurements were performed in a phosphate buffered saline (PBS) solution to replicate the biological environment that was used for cell stimulation studies. These measurements reveal the presence of step height changes, which could cause a reduction in the electrochemically active surface area (Figure 4.9). These step height changes manifest as both sharp height changes within the polymer surface itself (Figure 4.9 aii, d), and as voids on the surface of the polymer (visible in Figure 4.9 a-c). Root mean square roughness values attained for each sample correlate with the undulating surface observed through the AFM imaging with typical roughness values between 30 and 150 nm, with peak to valley roughness between 300 and 1500 nm (Table 4.1).

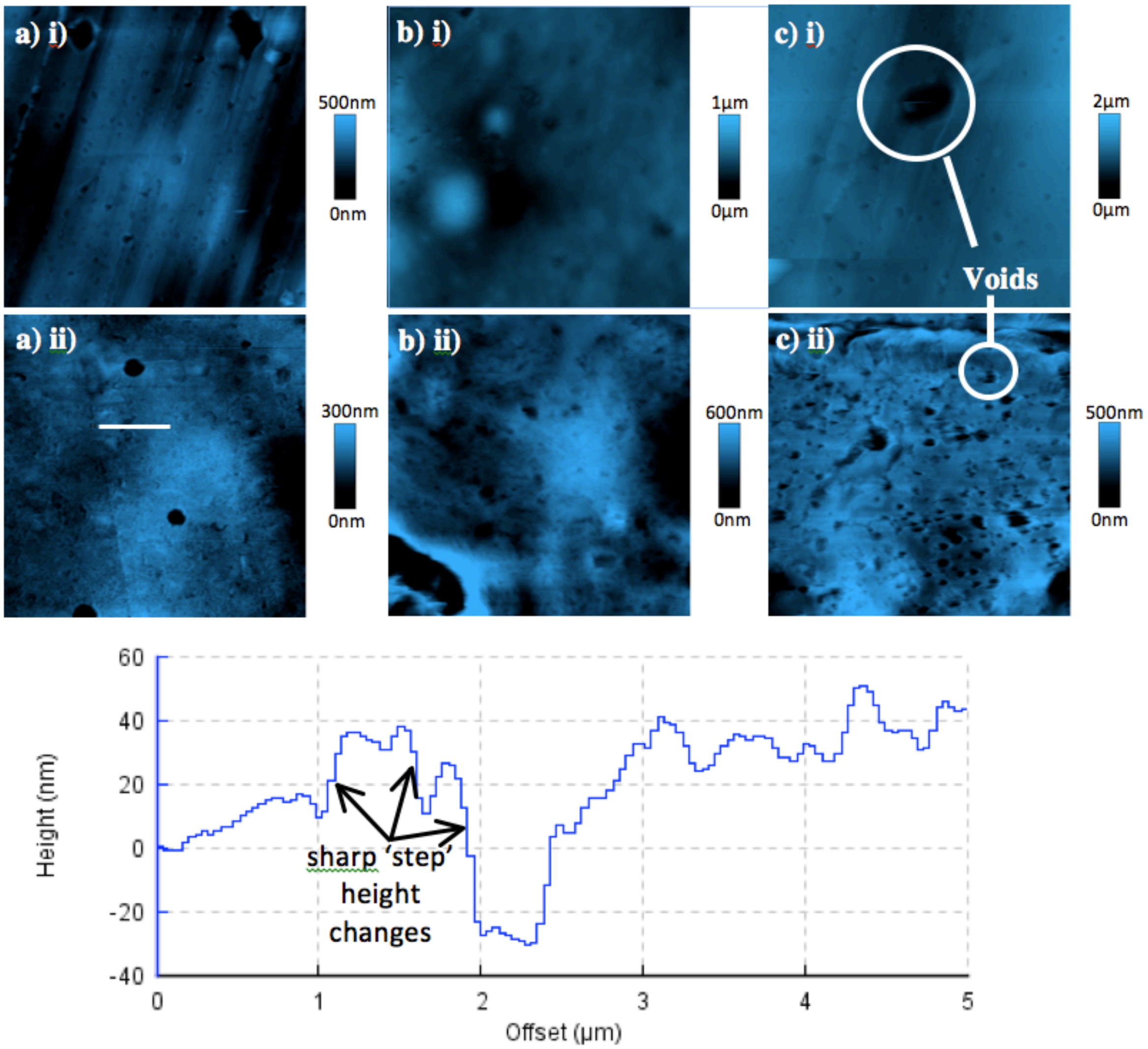

Figure 4.9 20 µm by 20 µm atomic force microscopy images detailing the surface morphology of graphene-polymer composite films in phosphate buffered saline solution; a) 50:50 PLGA; b) 75:25 PLGA; and c) PLA; i) polymer surface and ii) GBP; and d) Line profile showing the topography variation, including step height changes, over the line shown in a) i).

Table 4.1 Summary of the Raman Peak Intensity Ratio for (Figure 4.6) PLA and PLGA Composite Materials; Highlighting the Change in PLA:PLGA Ratios (I_{1410}:I_{1440}) and the Addition of Graphene ($2D_{2650}$:G_{1580})

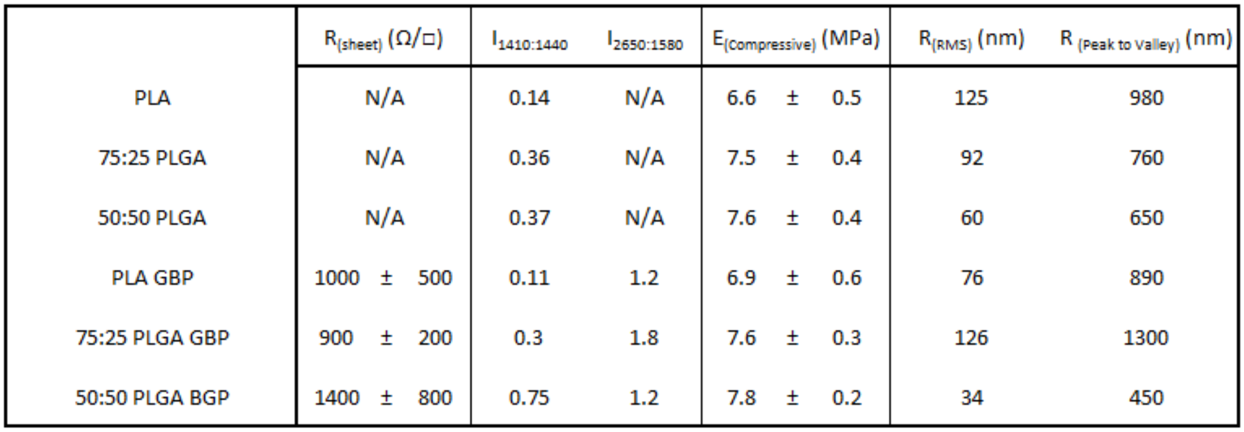

	$R_{(sheet)}$ (Ω/□)	$I_{1410:1440}$	$I_{2650:1580}$	$E_{(Compressive)}$ (MPa)	$R_{(RMS)}$ (nm)	$R_{(Peak\ to\ Valley)}$ (nm)
PLA	N/A	0.14	N/A	6.6 ± 0.5	125	980
75:25 PLGA	N/A	0.36	N/A	7.5 ± 0.4	92	760
50:50 PLGA	N/A	0.37	N/A	7.6 ± 0.4	60	650
PLA GBP	1000 ± 500	0.11	1.2	6.9 ± 0.6	76	890
75:25 PLGA GBP	900 ± 200	0.3	1.8	7.6 ± 0.3	126	1300
50:50 PLGA BGP	1400 ± 800	0.75	1.2	7.8 ± 0.2	34	450

To understand the mechanical properties of these GBP composites under compressive forces, AFM force measurements were collected using a silicon nitride tip with a spring constant of 20 $N.m^{-2}$ and maximum applied load of 40 nN. Force mapping curves were collected as a series of samples in a 32 x 32 array in order to measure the material properties across the GBS surface. The force maps display the slope (N/m) of the tip-sample contact region, which reflects the stiffness of the material (i.e. lighter areas are stiffer when using gray scale). The resulting force curves were found to correspond to a large range of modulus values, ranging between 1 MPa and 500 MPa for each sample. However, the compressive moduli of the GBP composites were observed to be either equivalent within error or slightly higher than the equivalent PLA or PLGA films (Figure 4.10).

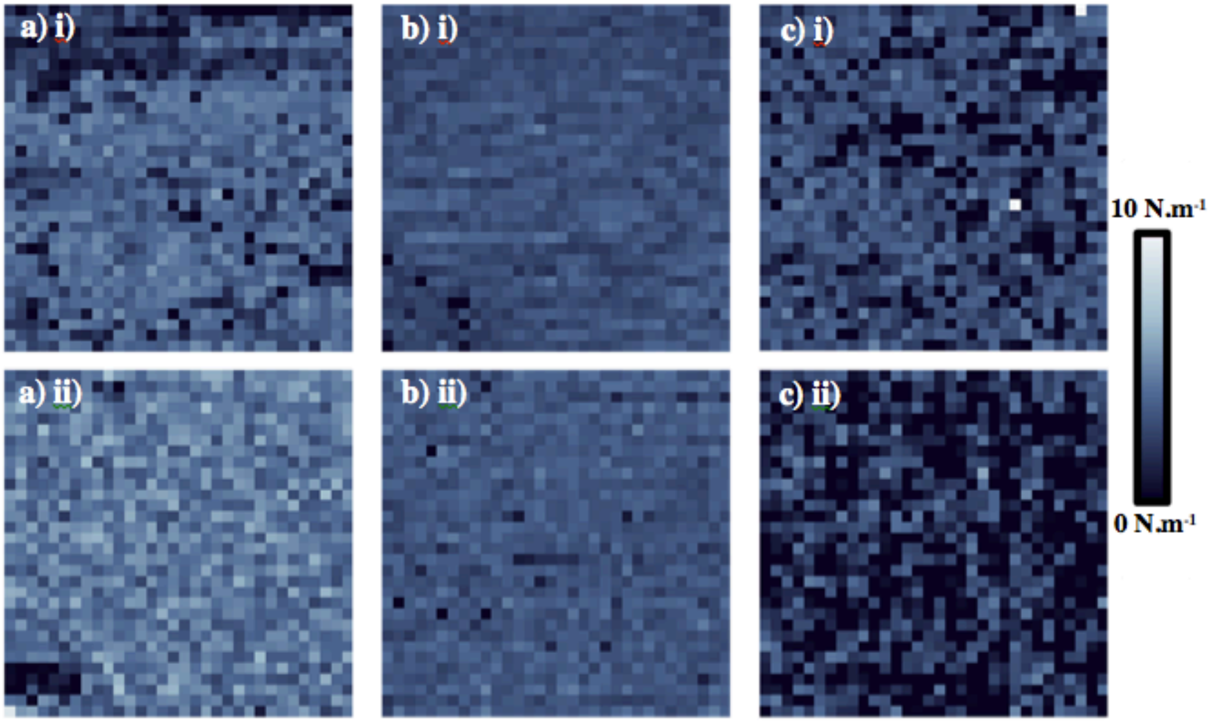

Figure 4.10 Slope measurements of force curves taken over a 20 µm by 20 µm area using a 20 nm tip radius silicon nitride AFM cantilever in phosphate buffered saline solution, a) 50:50 PLGA; b) 75:25 PLGA; and c) PLA; i) GBP; and ii) etched polymer only.

The compressive moduli of the films were tested on the macro-scale using a Shimadzu EZ mechanical analyzer. The indentation of the films by the 1 mm cylindrical probe fitted with a 2 N load cell demonstrated a clear linear response over the maximum total indentation distance of 200 µm. The compressive measurements yielded a compressive modulus according to Equation 4.1.

$$F = 2aE^{*}d$$

$$F \sim \left(\frac{8}{3}\right) aE_2 d$$

$$E_2 \sim \frac{3Fd}{8a}$$

Equation 4.1 Variation of Hooke's Law for establishing the compressive modulus of a material; where F = force (N); a = depth into the material (mm); E* is the compressive modulus of the sample and the probe (Pa); d is the diameter of the probe (mm) and E2 is the compressive modulus of the sample.

In the case of this mechanical test, the elastic modulus of the testing probe can be discounted as, using a stainless steel probe, $E_{probe} >> E_{sample}$ and the addition of mechanical properties occurs in series (Equation 4.2)

$$\frac{1}{E^{*}} = \frac{1}{E_{Probe}} + \frac{1}{E_{Sample}}$$

Equation 4.2 Expression detailing the addition of two different mechanical moduli; showing the observed modulus is equal to the sample modulus if the modulus of the probe is sufficiently large.

The slopes of the stress/strain compressive curve moduli were obtained for different polymers compositions with and without graphene (Figure 4.11). These values, see Table 4.1, were measured to range between 6.6 MPa for PLA and 7.8 MPa for graphene coated 50:50 PLGA. There was a consistent increase in the overall modulus of the structures with the addition of graphene. Incremental increases between 0.1 - 0.3 MPa, correspond to an increase between 2 - 5% of the initial material modulus value. We measured the sheet resistance values before and after these tests and found that they retained their values ranging from 900 - 1400 Ω.□$^{-1}$ (Table 4.1).

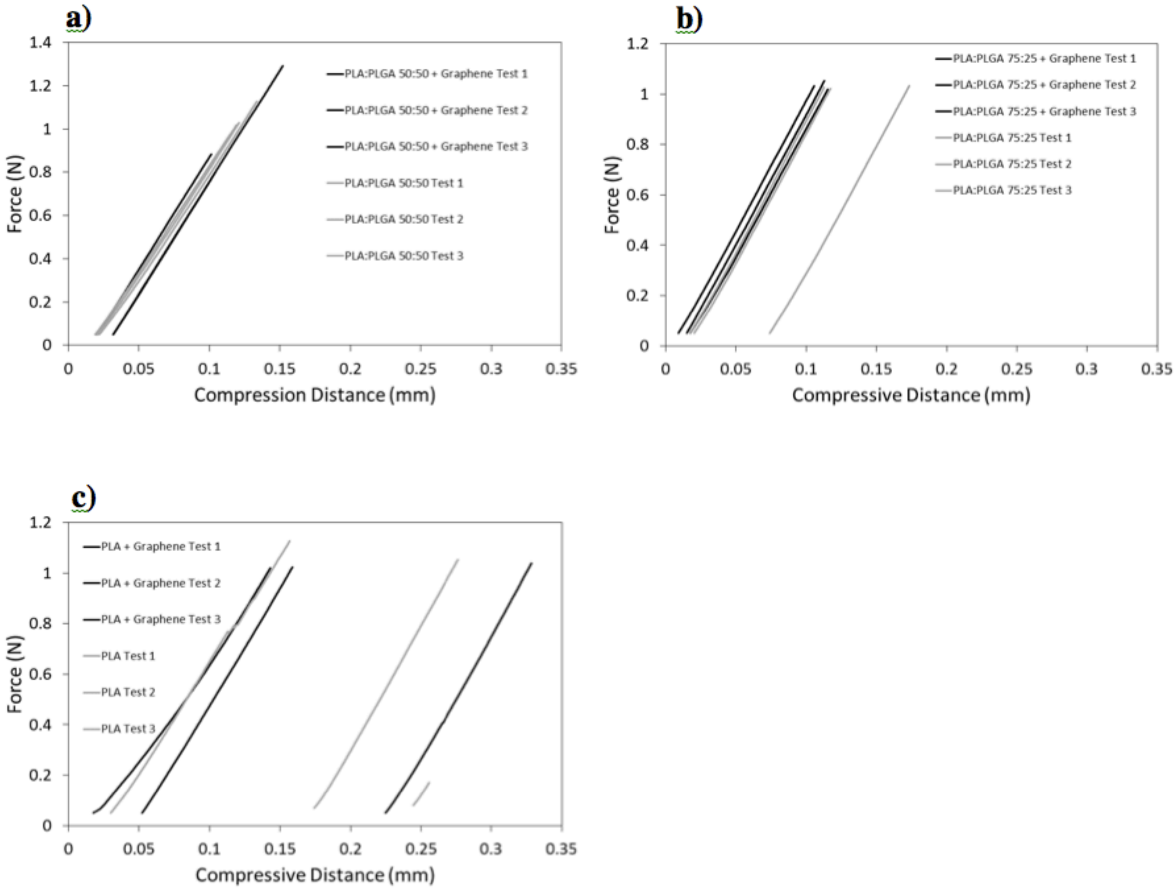

Figure 4.11 Compressive mechanical testing of PLA and PLGA composites with and without graphene; a) 50:50 PLGA; b) 75:25 PLGA; and c) PLA films.

The comparison of the bulk compressive modulus analysis and the AFM nanometer surface testing shows a marked difference in the consistency of the resultant compressive moduli, with the AFM force curves having a significantly broader range of values compared to the bulk compressive tests. Such variations in the AFM force curves are expected for nanometer scale force measurements, especially in complex composite surface systems. Different points are thought to correlate to areas of wrinkled graphene, sample defects (either polymer uncoated with graphene or voids within the polymer), and areas where there is poor adhesion between the graphene and the polymer.[30] Such nanometer, and micrometer scale defects are not detectable using bulk mechanical systems and, as such, these techniques provide independent, crucial, mechanical information regarding the surface mechanical properties on different scales.

The field of neuro-regeneration is concerned with the repair of nervous tissue and nerve cells in vivo. It is a matter of great importance because nervous system injuries affect over 90,000 people a year.[31] It is widely accepted that in order to regenerate and repair nerve cell tissue, the application of electrical stimuli to cells from a conducting material is required. We present here a potentially implantable and conductive composite material capable of facilitating electrical stimulation for neuro-regeneration.

In order to assess the suitability of these composite materials before the application of stimuli to cells, the adhesion and proliferation of a rat neural model cell line (PC-12) was first assessed by Pico Green assay. This assay estimates cell density by measuring the amount of DNA in solution after lysing the cells. As shown in Figure 4.12, at 24 hours after seeding, there was no difference in the adhesion and early proliferation of the PC-12 cells on any of the materials. However, the cell density on 50:50 PLGA, or 50:50 GBP had started to increase over other materials at 48 hours. This increased proliferation rate continued on to 4 days, with a significantly increased cell density on both the coated and uncoated materials. After a longer lag phase, PC-12 proliferation was also increased on the 75:25 PLGA biopolymer at 96 hours, and again, the cell growth observed was similar for GBP and unmodified PLGA. Cell proliferation was minimal on PLA, with only a slight increase in cell number after 24 hours. The cells were observed to be over 97% viable by live/dead (data not shown) on all materials, with no differences in cell viability observed between samples. Based on these results, the 50:50 PLGA material provided the optimal biopolymer formulation and was then used to make the GBP structures to study the efficacy of stimulated cell growth.

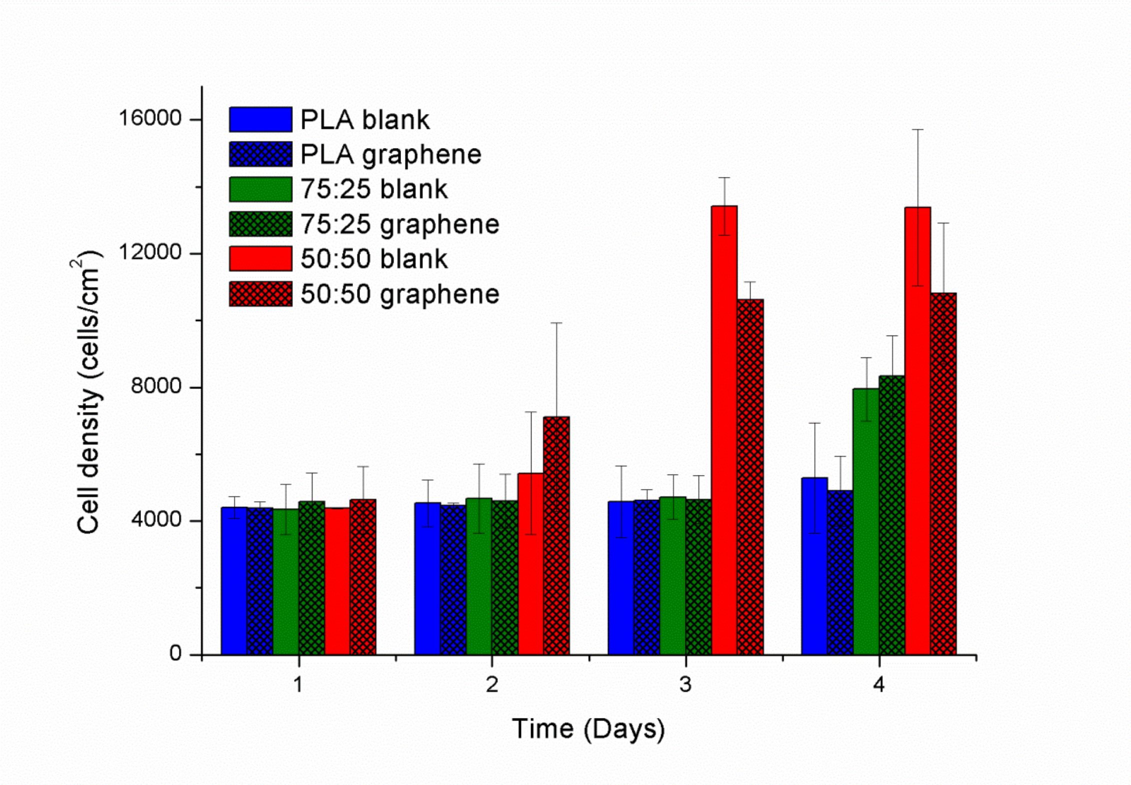

Figure 4.12 Proliferation of PC-12 cells on modified and unmodified PLGA over 4 days. The cells were seeded at 3000 cells.cm^{-2} on materials that were not coated with collagen or any other cell adhesion molecule and the cell densities were assessed at each time point using a Pico Green Assay to estimate amount of DNA. The cell proliferation wasn't affected significantly by graphene coating, but was highly dependent on the underlying polymer, particularly at 48-72 hours.

PC-12 cells differentiate into a neural phenotype when exposed to the protein nerve growth factor. The degree of differentiation, as measured by the length of neurites expressed by the differentiating cells, is known to be enhanced with electrical stimulation.[32–34] Cells were seeded onto the GBP structures at a density of 2000 cells cm^{-2} in 4 well chamber slides (area ≈ 1.5 cm^2), and changed to differentiation media after approximately 14 hours. Electrical stimulation was applied for 8 hours per day for 3 days, and the cells were fixed and stained immediately after the last period of electrical stimulation. As shown in Figure 4.13, the effect of electrical stimulation on the PC-12 cells was dramatic, with a large increase in the neurite length and connectivity of the neurites. The cell number, and number of neurites per cell showed no difference with electrical stimulation (Figure 4.14), but the average length of neurites per cell was significantly increased (a 2.5-fold increase from 30 μm per cell to 75 μm per cell, $p = 0.00028$ for the ANOVA statistic), due to a larger number of longer neurites, as illustrated in Figure 4.11c. This result is very significant, as it demonstrates both the ability of the composite material to communicate with cells in order to modify their metabolism by provision of electrical charge and also because it is the first literature report of enhanced nerve cell differentiation using graphene electrodes. Crucially the successful electrical stimulation of PC-12 cells, in combination with the step height changes demonstrated in the AFM height maps (Figure 4.7), validate the choice of bilayer graphene as the conductive material for the surface modification of the polymers.

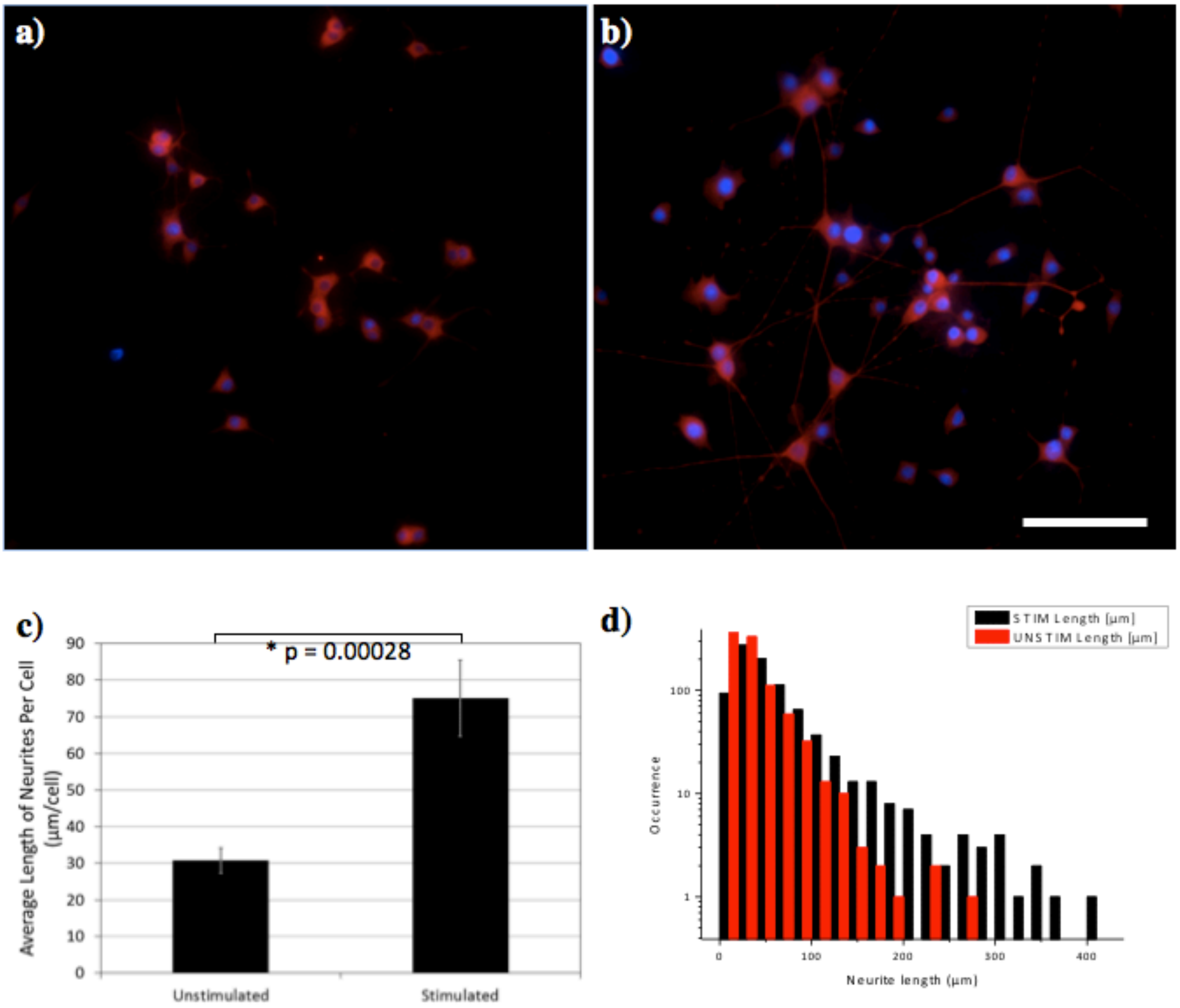

Figure 4.13 Differentiation PC-12 cells on GBP structures and analysis of image data: a) Fluorescence microscope without and b) with electrical stimulation. c) Shows the results of image analysis for neurite length performed over 8 mm^2 area. The error bars show one standard error of the mean, and the numbers describe the ANOVA statistics for comparison of stimulated and un-stimulated cells, with * indicating a statistically significant difference. d) Shows a histogram comparing the frequency of occurrence of neurite lengths in the stimulated and un-stimulated populations measured.

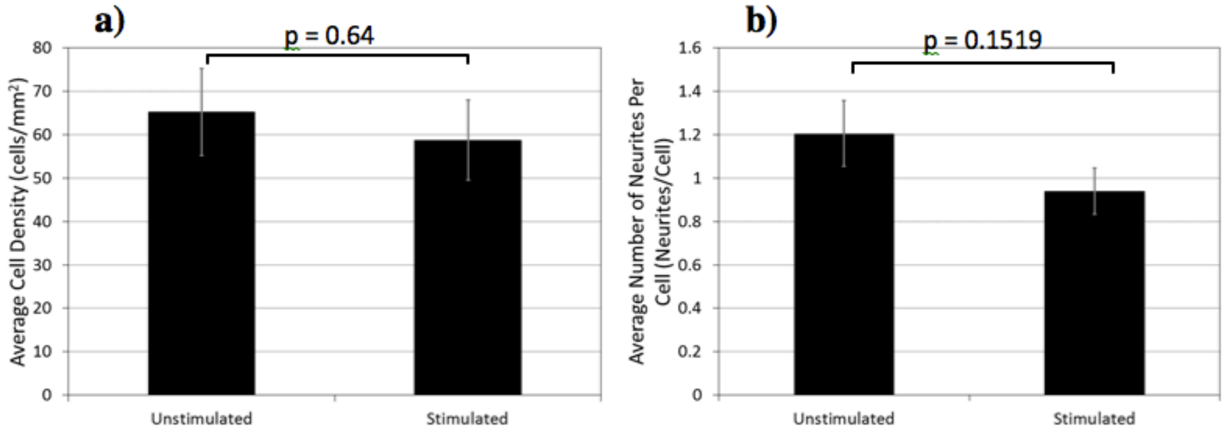

Figure 4.14 Cell density and neurite number per cell data derived from image analysis of PC-12 cells grown on 50:50 GBP with and without electrical stimulation, indicating that these parameters were not affected by electrical stimulation. The error bars show one standard error of the mean, and the numbers indicated describe the ANOVA statistics for comparison of stimulated and un-stimulated cells, which were not statistically different.

To confirm that the crystallinity of the graphene in the GBP structure was preserved after electrical stimulation, Raman mapping and spectral analysis were performed on the collagen-coated samples with the cells on the surface (Figure 4.15). The Raman spectra were segregated into three different data sets dependent on the 2D:G ratio (Figure 4.15a) and these data sets were overlaid with the optical image of the sample. The mapped data correlate with the presence of cells with a slight decrease in the 2D:G ratio surrounding cells visible in the optical images. This decrease is attributed to light scattering from the fluids inside the cell in combination with the low signal intensity from the graphene. Over the bulk of the examined sample, taken through the cell adhesion collagen layer, the average 2D:G ratio was 2.0±1.5 (mean ± standard deviation). This result confirms the structural stability of the graphene after electrical stimulation and the successful growth and differentiation of PC-12 nerve cells on GBP composite materials.

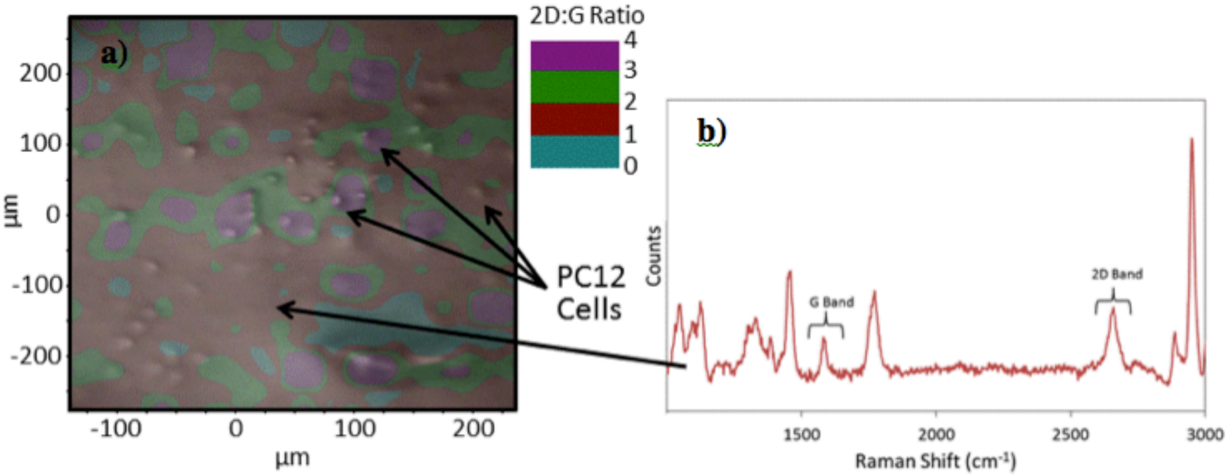

Figure 4.15 Raman spectra of GBP taken after electrical stimulation of PC-12 nerve cells, **a)** Raman map of 2D:G intensity ratio for 50:50 GPB composites after cell growth and electrical stimulation at 10x magnification; this maps demonstrated an average 2D:G ratio of 1.7 ± 1.0; and **b)** typical Raman spectra demonstrating the presence of bilayer graphene on the surface, and under the regions of PC-12 cells.

4.2.3 Conclusions to Nerve Cell Stimulation on Graphene Electrodes

We have successfully demonstrated graphene-biopolymer structures useful for cell stimulation and studied their mechanical and surface properties. The development was made possible by the novel process of transferring CVD-grown bilayer graphene onto the non-conducting biocompatible underlying polymer. Examining the interaction of these materials with PC-12 cells shows the addition of graphene onto the biopolymers did not change the cell-substrate interaction and the overall cell densities were defined by the underlying biopolymer composite. The optimal polymer composition (50:50 PLGA) was used to prepare the GBP structures for the electrical stimulation studies. A previously unseen increase in the average neurite length per cell was observed, which demonstrates the efficacy of GBP structures for supplying charge to cells. In essence, these results show the ability of bilayer graphene to serve as a material to add surface electrical conductivity over a large area; and over large morphological features. We have demonstrated the ability of graphene sheets to mimic the materials surface properties of the underlying substrate, and shown the applicability of a graphene-biopolymer composite as an electrode to enhance nerve cell differentiation.

References

1. Hong, A. J. *et al.* Graphene flash memory. *ACS Nano* **5**, 7812–7817 (2011).

2. Baek, D. J., Seol, M.-L., Choi, S.-J., Moon, D.-I. & Choi, Y.-K. Nonvolatile memory with graphene oxide as a charge storage node in nanowire field-effect transistors. *Applied Physics Letters* **100**, 093106 (2012).

3. Wallace, G. G., Moulton, S. E. & Clark, G. M. Electrode-Cellular Interface. **324**, 185–186 (2009).

4. Geim, a K. & Novoselov, K. S. The rise of graphene. *Nature materials* **6**, 183–91 (2007).

5. Batzill, M. The surface science of graphene: Metal interfaces, CVD synthesis, nanoribbons, chemical modifications, and defects. *Surface Science Reports* **67**, 83–115 (2012).

6. Park, H. J., Meyer, J., Roth, S. & Skákalová, V. Growth and properties of few-layer graphene prepared by chemical vapor deposition. *Carbon* **48**, 1088–1094 (2010).

7. Bhaviripudi, S., Jia, X., Dresselhaus, M. S. & Kong, J. Role of kinetic factors in chemical vapor deposition synthesis of uniform large area graphene using copper catalyst. *Nano Lett.* **10**, 4128–33 (2010).

8. Liu, L. *et al.* A systematic study of atmospheric pressure chemical vapor deposition growth of large-area monolayer graphene. *Journal of Materials Chemistry* **22**, 1498 (2012).

9. Hu, B. *et al.* Epitaxial growth of large-area single-layer graphene over Cu(111)/sapphire by atmospheric pressure CVD. *Carbon* **50**, 57–65 (2012).

10. Geim, A.K. Graphene: status and prospects. *Science* **324**, 1530–4 (2009).

11. Li, X. Cai, W., Kim, S., Tutuc, E., Ruoff, R.. Large-area synthesis of high-quality and uniform graphene films on copper foils. *Science* **324**, 1312–1314 (2009).

12. Rasool, H. I. *et al.* Continuity of Graphene on Polycrystalline Copper. *Nano Lett.* **11**, 251–256 (2011).

13. Coville, N. J., Mhlanga, S. D., Nxumalo, E. N. & Shaikjee, A. A review of shaped carbon nanomaterials. *South African Journal of Science* **107**, 1–15 (2011).

14. Brown, L. *et al.* Twinning and twisting of tri- and bilayer graphene. *Nano Lett.* **12**, 1609–15 (2012).

15. Castro, E. *et al.* Biased Bilayer Graphene: Semiconductor with a Gap Tunable by the Electric Field Effect. *Phys. Rev. Lett.* **99**, 216802 (2007).

16. Lui, C. H., Li, Z., Mak, K. F., Cappelluti, E. & Heinz, T. F. Observation of an electrically tunable band gap in trilayer graphene. *Nature Physics* **7**, 944–947 (2011).

17. Chen, C. Current advances in research and clinical applications of PLGA-based nanotechnology. *Expert Review of Molecular Diagnostics* **9**, 325–341 (2009).

18. Kiremitci-Gumusderelioglu, M. & Deniz, G. Synthesis, characterization and in vitro degradation of poly (DL-lactide)/poly (DL-lactide-co-glycolide) films. *Turkish Journal of Chemistry* **23**, 153–161 (1999).

19. Balgude, A. P., Yu, X., Szymanski, A. & Bellamkonda, R. V Agarose gel stickiness determines rate of DRG neurite extension in 3D cultures. *Biomaterials* **22**, 1077–1084 (2001).

20. Wang, Q. H. *et al.* Understanding and controlling the substrate effect on graphene electron-transfer chemistry via reactivity imprint lithography. *Nature Chemistry* **4**, 724–732 (2012).

21. Wassei, J. K. *et al.* Chemical Vapor Deposition of Graphene on Copper from Methane, Ethane and Propane: Evidence for Bilayer Selectivity. *Small* **8**, 1415–1422 (2012).

22. Ferrari, A. C. *et al.* Raman spectrum of graphene and graphene layers. *Phys. Rev. Lett.* **97**, 187401 (2006).

23. Malard, L. M. *et al.* Probing the electronic structure of bilayer graphene by Raman scattering. *Physical Review B* **76**, 201401 (2007).

24. Graf, D. *et al.* Spatially resolved Raman spectroscopy of single- and few-layer graphene. *Nano Lett.* **7**, 238–42 (2007).

25. Dresselhaus, M. S., Jorio, A., Souza Filho, A. G., Dresselhaus, G. & Saito, R. Raman spectroscopy on one isolated carbon nanotube. *Physica B: Condensed Matter* **323**, 15–20 (2002).

26. Mohana Reddy, A. L., Rajalakshmi, N. & Ramaprabhu, S. Cobalt-polypyrrole-multiwalled carbon nanotube catalysts for hydrogen and alcohol fuel cells. *Carbon* **46**, 2–11 (2008).

27. Frackowiak, E. & Béguin, F. Carbon materials for the electrochemical storage of energy in capacitors. *Carbon* **39**, 937–950 (2001).

28. Largeot, C. & Portet, C. Relation between the ion size and pore size for an electric double-layer capacitor. *Journal of the …* **4**, 2730–2731 (2008).

29. Shiraishi, S., Kurihara, H., Okabe, K., Hulicova, D. & Oya, A. Electric double layer capacitance of highly pure single-walled carbon nanotubes (HiPcoe Buckytubese) in propylene carbonate electrolytes. *Electrochemistry Communications* **4**, 593–598 (2002).

30. Gelmi, A., Higgins, M. J. & Wallace, G. G. Physical surface and electromechanical properties of doped polypyrrole biomaterials. *Biomaterials* **31**, 1974–83 (2010).

31. Stabenfeldt, S. Thermoreversible lamininâ-functionalized hydrogel for neural tissue engineering. *Journal of Biomedical …* (2006).doi:10.1002/jbm.a

32. Schmidt, C. Bioelectronics: The bionic material. *Nature* **483**, S37 (2012).

33. Lee, N. H. *et al.* Comparative expressed-sequence-tag analysis of differential gene expression profiles in PC-12 cells before and after nerve growth factor treatment. *Proceedings of the National Academy of Sciences of the United States of America* **92**, 8303–7 (1995).

34. Liu, X., Gilmore, K. J., Moulton, S. E. & Wallace, G. G. Electrical stimulation promotes nerve cell differentiation on polypyrrole/poly (2-methoxy-5 aniline sulfonic acid) composites. *Journal of neural engineering* **6**, 065002 (2009).

Chapter 5: Future Work

5.1 Growth of Boron Tricarbide Monolayers

At the end of any graduate student's tenure, there is likely to be a large amount of unfinished experiments or future studies they wished they could perform. While I spent a large portion of my final year building a CVD system with old parts, I wished I had time to add a few parts to the system so that I could grow single layers of boron tricarbide, BC_3.[1] In 1986, Kouvetakis et al. described the growth of multilayered BC_3 at atmospheric pressure and with liquid precursors. This physical vapor deposition process used carcinogenic precursors that would need to be scrubbed prior to entering the vacuum pump and out to the exhaust. In addition, a specialized sparge system would need to be integrated into the existing hardware, such that, the various halogenated species will not react with the carrier gasses until entering the reactor zone. I would predict that lower pressures would result in fewer layer deposition and possibly control down to single layer. In addition, since this deposition occurred on quartz, it is likely that metal catalysts are not needed, but further investigation is merited.

5.2 A Rational Design of Efficient, Graphene-Scaffolded Photo-Catalyst Structures Using Inorganic and Organometallic Photo-sensitizers

While photo-catalysts have the potential to impact many areas of research such as the degradation of pollutants and hydrogen generation, many of these routes are hampered by the lack of thoughtfully designed systems and low efficiency due to recombination of generated electron-hole pairs. Therefore, the suppression of recombination is of paramount importance for the enhancement of said photo-catalysts.

Graphene - a single layer of sp^2 carbon – is a zero bandgap semiconductor that possesses a slew of interesting intrinsic properties. For instance, it is highly conductive with superior carrier mobility, has a wide window of electromagnetic radiation absorption, possesses ample surface area and can form covalent bonds, ionic bonds or stack via pi-pi interactions with other aromatic molecules. These properties have been shown to enhance the photo-catalytic behavior metal oxide semiconductors and organic chromophores by acting as an efficient light scavenger, scaffold material and electron acceptor.[2,3] For artificial photosynthesis to be realized, on a large scale, a highly efficient light active photo-catalyst system needs to be developed. Recently, there has been a report in which graphene was combined with a chromophore to generate and shuttle electrons to a rhodium catalyst for the enzymatic conversion of CO_2 into formic acid. In short, this system is efficient, but, like several other approaches, uses the less conductive graphene derivative, reduced graphene oxide.

Herein, I describe a new strategy for enhancing the photo-catalytic properties of metal oxide semiconductors and organic chromophores, using large-area, highly conductive CVD-derived graphene, and the subsequent shuttling of electrons to organometallic complexes, with minimum recombination that can be used for a variety of applications.

5.2.1 Technical Approach

Highly crystalline graphene can be grown via CVD on copper substrates and subsequently transferred onto a variety of surfaces. A few photo-sensitizers have been selected to be incorporated into this graphene-scaffolded photo-catalyst system. First, titanium dioxide (TiO_2) electrodes have been used to demonstrate the photo-catalytic splitting of water.[4] Since then, there has been a great deal of progress in the area of metal oxide semiconductor for applications in solar energy conversion. For this reason, titanium dioxide nanoparticles will be used as photo-sensitizers because they have had great success with photo-excitation and the generation of electron-hole pairs.[5,6] Second, the organometallic complex, tris(bipyridine) ruthenium (II) or $[Ru(bipy)_3]^{2+}$, will be studied because the excited state has a relatively long lifetime. In the appropriate ratio, these two materials should be able to convert and transfer generated electrons and react with pollutants or dyes quicker than the electron-hole recombination rate of graphene. Alternatively, mild oxidation treatments or doping experiments, as described early, can hamper this recombination process. The photo-sensitizers described here can be purchased off the shelf and readily combined with the graphene scaffold via self-assembly, see Figure 5.1. Once incorporated with graphene, these photo-catalyst structures should be able to split water in the presence of light and hydrogen evolution should be evident. In addition, it would be useful to explore the synthesis and exploration of other organic porphyrin-containing chromophores, described in a recent paper,[3] and this will require some organic synthesis and purification.

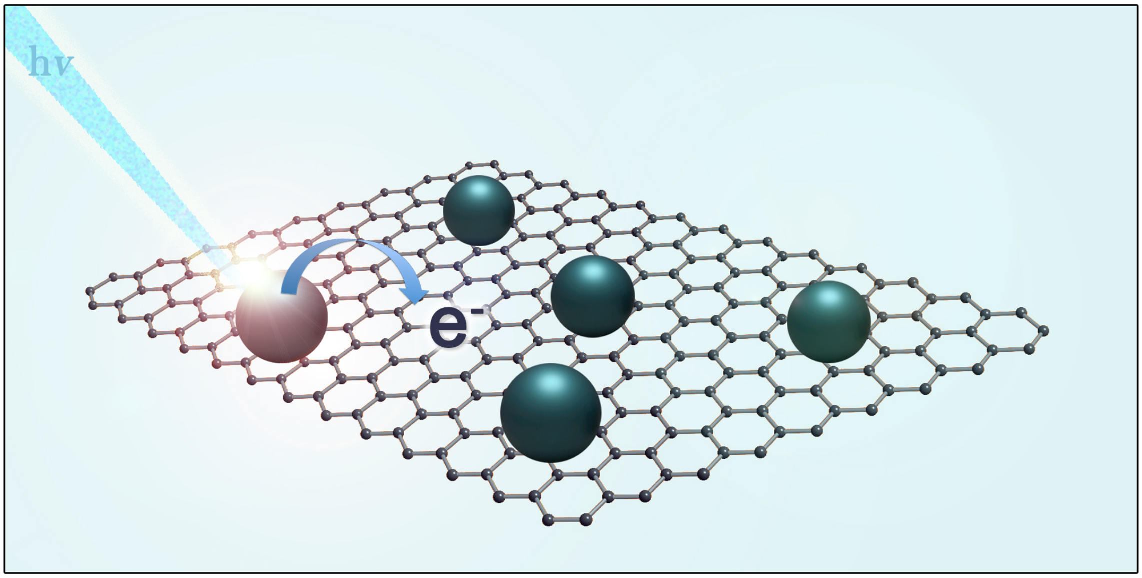

Figure 5.1 An illustration of a graphene photo-catalyst structure, decorated with catalytic nano-structures.

Papers describing photo-catalysis enhancement using graphene, use solution-processed graphene derivatives. While this is definitely a scalable route to graphene, it is unclear whether or not this approach will be useful beyond the proof-of-concept stage. For instance, if one wanted to do actual photo-catalysis and subsequent photo-synthesis of formic acid, alcohols, glucose etc., it seems problematic to filter out so many materials and isolate a product. Instead, GPS can be prepared as large electrodes, via roll-to-roll processing, and introduced into aqueous baths.

5.3 Platinum Decorated, Laser-Scribed Graphene for Rapid Glucose Monitoring

According to the Center for Disease Control (CDC) there were approximately 25.8 million Americans living with diabetes in 2011, all of which must test their blood glucose levels daily.[7] Oddly enough, this makes blood the most commonly tested analyte. Diabetics continuously monitor glucose levels with a combination of glucose test strips and a wearable glucose monitoring system. Many diabetics report a discrepancy in recorded values, but have no alternative but to live with this uncertainty.[7] The current state-of-the art sensors utilize an amperometric monitoring system that relies on the use of platinum catalyst surfaces without the enzyme intermediate, glucose oxidase. This enzyme-less route is promising because the detector is more stable under environmental conditions, but requires platinum with a moderately high surface area.[8] Decorating laser-scribed graphene (LSG) with platinum nano-structures (see Figure 5.2) would be an attractive alternative to what is currently available in the market for several reasons. First, the LSG yields a foam-like material with an extremely high surface area with many vacancies for platinum nano-particles to nestle into. Second, this LSG route appears to be scalable, cost-effective and because it is conductive, it is easy to decorate with metal nanoparticles. Third, a proof-of-concept device can be built with little expertise. Finally, the cyclic voltammetry measurement is quite straightforward and provides accurate glucose concentration and detection time.

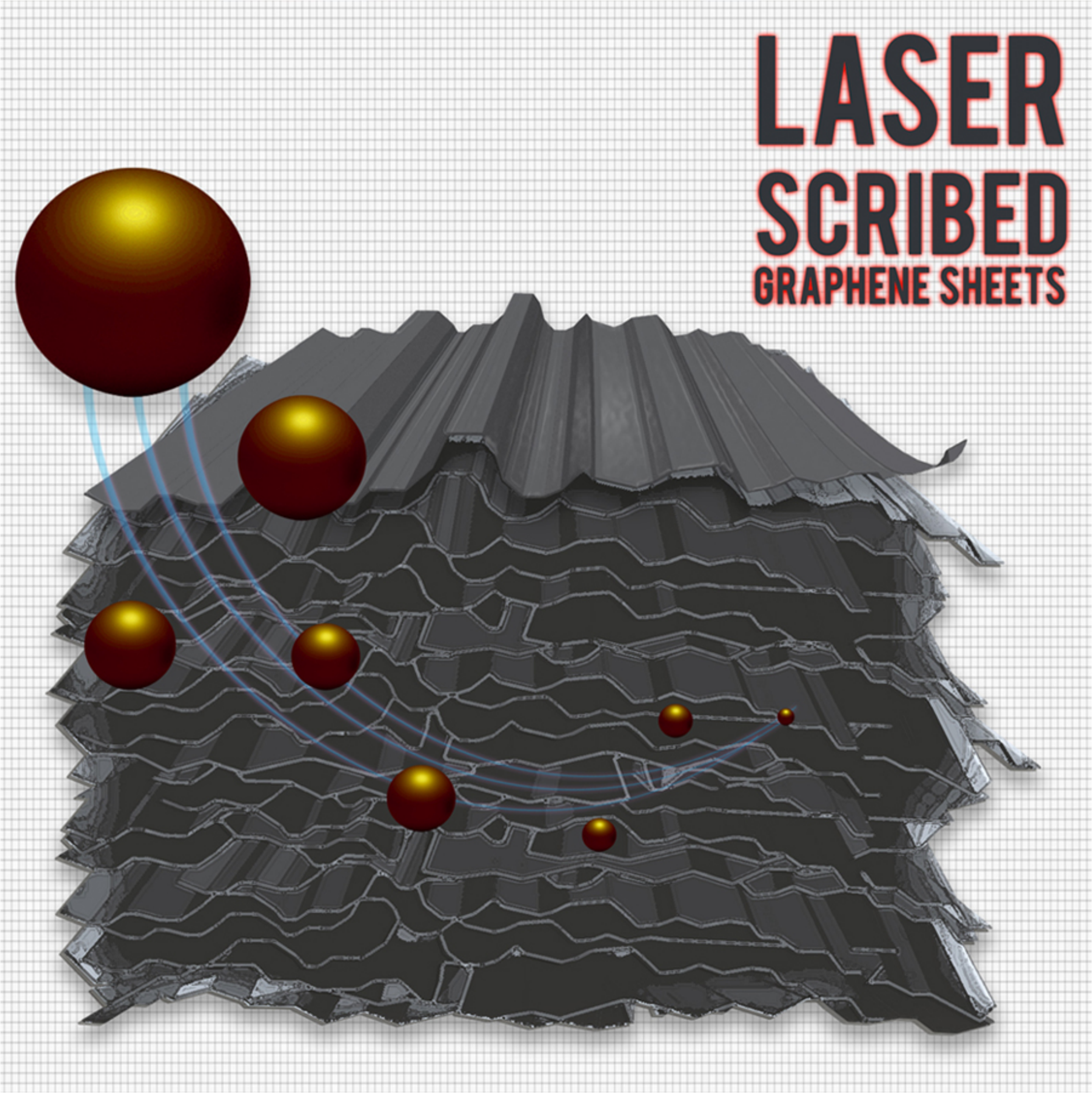

Figure 5.2 An artist rendering of high surface area, laser-scribed graphene sheets with many voids for metal nanoparticles (orange spheres) to electro-deposit into.

References

1. J. Kouvetakis, R.B. Kaner, M.L. Sattler and N. Bartlett, "A novel graphite-like material of composition BC_3 and nitrogen-carbon graphites," *J. Chem. Soc.*, *Chem. Commun.*, 1758 (1986).

2. Q. Xiang, J. Yu and M. Jaroniec, *Chem. Soc. Rev.*, 2012, 41, 782-796

3. R.K. Yadav, J. Baeg, G.H. Oh, N. Park, K. Kong, J. Kim, D.W. Hwang, and S.K. Biswas, *JACS*, 2012, 134, 11455-11461

4. A. Fujishima and K. Honda, *Nature*, 1972, 238, 37.

5. X. Y. Zhang, H. P. Li, X. L. Cui and Y. H. Lin, *J. Mater. Chem.,* 2010, 20, 2801

6. L. F. Qi, J. G. Yu and M. Jaroniec, Phys. *Chem. Chem. Phys.,* 2011, 13, 8915.

7. CDC *National Diabetes Fact Sheet, 2011*. 1–12 (2011).at http://www.cdc.gov/diabetes/pubs/pdf/ndfs_2011.pdf

8. K.E. Toghill and R.G. Compton, *Int. J. Electrochem. Sci.,* 5 (2010) 1246 - 1301